Dynamique non-linéaire dans les systèmes nano-électromécanique à basses températures

Martial Defoort

UNIVERSITÉ DE GRENOBLE

THÈSE

Pour obtenir le grade de

DOCTEUR DE L'UNIVERSITÉ DE GRENOBLE

Spécialité : **Physique de la matière condensée et du rayonnement**

Arrêté ministériel : 7 août 2006

Présentée par

Martial Defoort

Thèse dirigée par **Eddy Collin**

préparée au sein **de l'Institut Néel, CNRS, Grenoble**
et de **Ecole doctorale de physique de Grenoble, Université Joseph Fourier**

Non-linear dynamics in nano-electromechanical systems at low temperatures

Dynamique non-linéaire
dans les systèmes nano-électromécaniques
à basses températures

Thèse soutenue publiquement le **16/12/2014**,
devant le jury composé de :

Mr. Olivier Bourgeois
Director of Research, Néel Institute Grenoble, France, Président
Mr. Mark Dykman
Professor, Michigan State University, USA, Rapporteur
Mr. Warner Venstra
Doctor, TU Delft, Netherlands, Rapporteur
Mr. Stephen Purcell
Director of Research, ILM Lyon, France, Examinateur
Mr. Sebastien Hentz
Doctor (HDR), CEA LETI Grenoble, France, Examinateur
Mr. Andrew Armour
Associate Professor, University of Nottingham, UK, Invité

A part of the present manuscript has been
removed due to confidential content.

Remerciements

Ces trois années de thèse ont été un incroyable enrichissement personnel, et c'est essentiellement grâce à vous !

Je tiens donc à remercier Eddy, mon encadrant. Tu as su m'encadrer et être présent tout en me laissant gérer mon temps. C'est grâce à ta pédagogie et ta patience que j'ai pu progresser en recherche. Mais avant d'être une expérience professionnelle, ces trois années avec toi ont surtout été une formidable expérience humaine. Ces soirées ensemble autour d'un verre ou d'un jeu de plateau, ces interludes en manip' à base de "A kind of Magic" ou de "Seek and Destroy" ... Je n'aurais jamais pu m'épanouir autant en thèse sans cette relation qu'on a pu avoir. Tu as toujours été compréhensif, tu as su me faire confiance, tu m'as permis de voyager et par là même de gagner en maturité et en ouverture d'esprit. Merci.

Je remercie aussi Henri. Les longues conversations avec toi m'ont beaucoup appris. J'ai particulièrement apprécié la semaine qu'on a passé tous les deux à Lancaster. Je te remercie, Andrew, pour ton aide dans ma recherche de post-docs.

Merci aux non-permanents de l'équipe UBT ! C'était une incroyable expérience. Kunal, "Qu'est-ce que diiiiiit Dykmaaaaan ?!", you taught me so much.. and I miss the Hobgoblins ! Ahmad (alias Alexandre), tes histoires vécues devraient faire l'objet d'une saga télé. Je remercie aussi Olivier, ta culture musicale donnait une sacré ambiance à la salle de manip', ainsi que Ketty et Florent pour votre bonne humeur.

Je remercie toutes les personnes du CNRS avec lesquelles j'ai pu travailler, notamment Olivier Bourgeois, Sébastien Triqueneaux, Thierry Crozes, Jean Guidi, Julien Minet, Patricia Poirier et le personnel du liquéfacteur.

Je remercie l'équipe de Lancaster avec laquelle j'ai collaboré et qui m'a accueilli pendant plusieurs semaines dans leur laboratoire : Shaun Fisher, Georges Pickett, Viktor Tsepelin, Malcolm Poole, Sean Ahlstrom, Andrew Woods. Je remercie aussi Fabio Pistolesi et Vadim Puller de Bordeaux pour la très intéressante collaboration qu'on a eu sur la bifurcation. Je remercie Andrew Armour de Nottingham pour son aide essentielle à la compréhension du mode-coupling.

Je remercie Olivier Commowick, qui m'a permis de gagner un temps précieux lors de la rédaction, en mettant en libre accès son template de thèse déjà bien élaboré. Je tiens aussi à remercier Thom Yorke et Jonny Greenwood pour leur soutien et leur source d'inspiration au quotidien durant la période de rédaction du manuscrit.

Je remercie Étienne, Alexander, Karim, Émilie, Caterina ainsi que les disciples du BatMan : Benoît, Guillaume, Tobias, Grégoire, Vivien... pour tous les moments passés ensemble au sein de l'institut (ou autour d'une bière !).

Je remercie les amis externes au CNRS avec lesquels j'ai pu partager les bons et mauvais moments de ma thèse : Mehdi, Rachel, Mélina, Pierre, Estelle, Vincent, Lisa, Pierre-Loup, Amandine, et bien sûr la Maîtresse de Boissons, mais aussi la SunaTeam en la personne d'Alexis, Clément, Pierre, Germain, Julien...

Paul et Florence, depuis le début des études supérieures, vous avez toujours été un moteur pour moi. Votre franchise et vos conseils m'ont amené à faire cette thèse, je vous remercie.

Je remercie la Kroloc avec laquelle j'ai vécu durant ces trois années de thèse, que ce soit pour les sept Kro de cristal ou pour les heures de débats/conversations à table. Joce, ces concerts préparés ensemble ont été mémorables, parmi mes meilleurs souvenirs. Benji, ton optimisme a bien souvent allégé le poids de la rédaction. Pierre, tu es parti tôt, mais ton dynamisme a été une source de motivation.

Je remercie aussi ma famille, et particulièrement mes parents et ma sœur. Vos conseils ont toujours guidé mes pas, et votre soutien a été essentiel. Si j'en suis arrivé là, c'est surtout grâce à vous.

Pour finir, merci Laura pour m'avoir conseillé et supporté ces derniers mois de thèse, je te dois beaucoup, et j'ai hâte de commencer notre expérience aux États-Unis.

Contents

General introduction

Contents

I.1   Fundamental Science with nano-mechanical devices

Fundamental physics is a challenging field of investigation, the study of a specific system requiring dedicated detectors/probes whose design and development are topics of research on their own. In astrophysics, the latest discoveries on the Universe arose from telescopes and satellites. In nuclear physics, detectors and counters are essential for the comprehension of elementary particles. In condensed matter, SQUIDs (Superconducting QUantum Interference Devices) give access to electric signals almost down to the quantum limit (about tens of $\hbar$ energy resolution), SEM (Scanning Electron Microscopes) permit to observe matter at the nanometre scale and LASER (Light Amplification by Stimulated Emission of Radiation) are at the core of many detection techniques, like the Raman spectroscopy.

Micro-Electro-Mechanical Systems (MEMS) are also extremely valuable sensors for condensed matter physics. They are small (at least one of their dimension being in the μm range), light (and thus very sensitive) and they are able to transduce an electric signal into a mechanical deformation (and vice-versa). As foreseen by R. P. Feynman's lecture *There's Plenty of Room at the Bottom* [Feynman 1993], the development of MEMS increased with the expansion of their possible applications, and a large contribution to this field came from the Industry. While those micro-technologies are employed in everyday life for example in smartphones, watches or cars, they are also implemented in applied science as electronic switches [Rebeiz & Muldavin 2001], for frequency control [Nguyen 2007] or in Lab-on-a-chip technologies using bio-MEMS [Verpoorte & de Rooij 2003], the list being non-exhaustive. Furthermore, fundamental research also benefits from the sensitivity of such devices, for instance with the search for deviations in the law of gravity at small lengthscales (as predicted from some extensions of the Standard Model) [Chiaverini *et al.* 2003], with the study of the Casimir force (the attraction between two closeby metallic plates) [Chan *et al.* 2001] or as a thermometers for superfluid ^{3}He experiments at ultra-low temperatures (below 1 mK) [Triqueneaux *et al.* 2000].

As the fabrication process improved, the dimensions of the devices could get reduced, enabling the fabrication of NEMS (Nano-Electro-Mechanical Systems). Vibrating from hundreds of kHz to the GHz range [Island *et al.* 2012], they can be made of silicon [Cleland & Roukes 1996], diamond [Espinosa *et al.* 2003] or carbon nano-tubes [Bachtold *et al.* 1999], with geometries such as drums, cantilevers or doubly clamped beams, driven through capacitive, magnetomotive [Cleland & Roukes 1999] or self-oscillating schemes [Barois *et al.* 2013], the list being non-exhaustive. Following on the path of MEMS, these nano-resonators demonstrate a very high mass sensitivity [Hanay *et al.* 2012], although it is not their only interesting feature: they are *actual model systems* for numerable degree of freedom physics [Jacobs 2012]. The NEMS is thus not only a probe for condensed matter, but also the system under study itself, investigating fundamental areas of Science. Both aspects will be discussed in this thesis, although the focus will be essentially on the latter. Among the different kinds of NEMS existing in the literature, the structures at the core of this thesis are simple beam-based resonators.

A NEMS resonator can be thought of as an almost ideal 1D harmonic oscillator which makes it very convenient when it comes to test fundamental theories: its basic dynamic properties are rather simple to express from (rather simple) theories. However, in order to use this device for such an ambitious purpose, a cryogenic environment is required for two distinct practical reasons.

On one hand, a low temperature environment reduces electrical noise, enabling to perform more sensitive measurements. It permits to handle high currents using superconducting lines and thus to work with large magnetic fields. With the NEMS confined in a leak-tight experimental cell, the Kelvin temperature range leads to cryogenic vacuum which contributes to cleaner acquisitions of mechanical vibrations, free from spurious outgassing and environmental fluid friction.

On the other hand, the temperature is a key parameter in condensed matter, as the phenomena involved in a system change with the energy scale that is probed. Working at cryogenic temperatures hence enables to prevent undesired physical effects that could spoil our measurements, like the thermal contractions in materials which are frozen typically below 50 K. Last but not least, thanks to their high resonance frequency NEMS can probe quantum physics at low enough temperatures (with respect to the oscillator's fundamental state energy).

Reaching the quantum ground state in a *mechanical macro-system* is one of the most challenging motivations in the field of NEMS, where the resonator itself becomes the quantum object under study, typically in the millikelvin temperature range [Regal *et al.* 2008, O'Connell *et al.* 2010]. Furthermore, quantum matter can be studied through its interactions with a nano-mechanical device: this research can be focused on quantum solids with the constitutive materials of the NEMS (so-called two level systems present in amorphous materials like silicon nitride [Southworth *et al.* 2009]), or on quantum fluids with the immersion of the probe in a quantum fluid like ^{3}He or ^{4}He [Kraus *et al.* 2000]. However, the present manuscript does not focus on the quantum aspects, and our experiments are mostly performed around the kelvin which already gives access to complex and elegant (yet classical) physics. Indeed, making use of the non-linearities, it is possible to build systems of ubiquitous interest, and one rising utilisation of NEMS is to create analogous systems, implementing fundamental non-linear phenomena or even creating *classical analogues of quantum effects*. For instance, using two degenerate flexural modes of a nano-beam (experiencing in-plane and out-of-plane motion), a classical two level system has been realised displaying the equivalent of Rabi oscillations [Faust *et al.* 2013]. The phenomenon is based on a non-linear interaction between those two modes, and poses the challenging question: what is really quantum in a Rabi-type measurement. In a more general view, any coupling behaviour between distinct modes emerges from non-linearities, which is at the core of this thesis. The first step before using NEMS as probes for fundamental physics is thus to understand the nano-resonators' behaviour itself, which implies a thorough study of the nano-structure on its own.

I.2   Positioning of realised research

In Chap. II we describe the experimental set-up and characterise the nano-structures we manipulated. The peculiarity of our layout is to be optimised for fine measurements of the devices' mechanical properties (high-impedance environment). We demonstrate that these measurements are thoroughly calibrated, which is essential in order to use the NEMS as a model system, and we present in real units the resonators' parameters (motion in meters, force applied in Newtons).

By using the intrinsic non-linearity of the devices, we show in Chap. III our findings on the coupling between modes within a single resonator. Taking the particular case of coupling one mode with itself through a two-tone drive, we develop both theoretically and experimentally a new scheme of high precision measurement which transduces motion into frequency.

By controlling the non-linearity of an intrinsically highly linear NEMS, we investigate in Chap. IV the bifurcation process which is known to exhibit universal scaling laws. Making use of the control of the non-linearity, the phenomenon which is at the heart of the bifurcation phenomenon, we could explore a wide range of parameters up to the region where no analytical theory predicts its behaviour. After a description of the model's limit, we demonstrate both experimentally and numerically that the scalings hold in a range beyond the analytical predictions. We also discuss and show preliminary results on an application of the bifurcation process: the detection and characterisation of low frequency intrinsic two-level systems (TLS) present in the resonator itself.

We present in Chap. V actual implementations of the NEMS as sensors for condensed matter physics. Various schemes are developed to enhance the probing capabilities of nano-resonators, and the non-linear schemes of Chap. III are some of them. In the first section of the present chapter we describe an audio-mixing technique that enables to imprint a low-frequency (audio) signal into the motion of the high-frequency (r.f.) nano-mechanical mode. Cooling down the NEMS to tens of millikelvin, we used the standard magnetomotive scheme to probe the mechanisms at the essence of the dissipation in our structures, namely the intrinsic TLS present within the constitutive materials. Immersing our structures in a rarefied gas, we explored the interactions with a benchmark fluid (^{4}He gas at 4.2 K) and demonstrated our ability to access unique microscopic physical properties: here studying slippage and the boundary layer in the molecular regime.

To finish with, we conclude with a brief summary of the manuscript in Chap. VI, highlighting the contributions of this work to the field of NEMS and the associated perspectives.

I.3   Résumé

La physique fondamentale est un domaine d'investigation ambitieux, l'étude d'un système spécifique exigeant des détecteurs/sondes dédiés, dont la conception et le développement est un sujet de recherche en soi. En physique de la matière condensée, de tels outils ont été mis au point suivant les exigences de cette spécialité, tel que les SQUIDs (Superconducting Quantum Interference Devices) ou les SEMs (Scanning Electron Microscopes). Les MEMS (Micro-Electro-Mechanical Systems) bientôt suivi par les NEMS (Nano-Electro-Mechanical Systems), ont aussi leur place dans cette liste de part leur petite taille, leur faible masse, et leur capacité à transférer un signal électrique en un signal mécanique, et inversement. Leur nature et leur utilisation sont très variés, et dans cette thèse nous nous concentrerons uniquement sur des nano-résonateurs de géométrie assez simple. On dissocie principalement deux utilisations de ces nano-structures : comme sonde en physique de la matière condensée et comme système modèle où le NEMS lui-même devient le système à l'étude. Même si ces deux aspects seront étudié dans ce manuscrit, cette dernière facette sera la plus détaillée. Afin de mener à bien ce projet, nous utilisons un environnement sous vide et à basse température (essentiellement un cryostat à 4.2 K) pour obtenir des mesures précises tout en ayant un contrôle sur les paramètres physiques ressentis par le NEMS (la pression et la température). Plusieurs sujets de physique fondamentale ont mis à contribution l'aspect de système modèle du NEMS, en particulier en physique quantique. Il existe cependant d'autres domaines accessibles, comme la mise au point de systèmes analogues entre la physique quantique et la physique classique, ou encore l'étude des systèmes non-linéaires qui est la thématique au cœur de ce manuscrit.

Dans le Chap. II, nous présentons le dispositif expérimental mis en place pour étudier nos échantillons. Après une calibration détaillée de nos lignes, nous étudions les propriétés physiques élémentaires de nos nano-résonateurs sur une large gamme de différents paramètres. En utilisant la non-linéarité intrinsèque de nos poutres doublement encastrées, nous présentons dans le Chap. III le couplage entre deux modes d'un seul résonateur. Nous nous intéressons ensuite au cas particulier d'un dispositif à deux tons, excitant un seul mode. En contrôlant la non-linéarité induite dans un NEMS initialement linéaire, nous étudions dans le Chap. IV le phénomène de bifurcation entre deux états de notre structure, dont le comportement au sein d'une hysteresis est prédit comme étant universel. Nous verrons alors comment ce phénomène peut être utilisé pour détecter du bruit basse fréquence dans nos nano-résonateurs. Nous présentons dans le Chap. V quelques exemples développés durant cette thèse sur l'utilisation des NEMS comme sonde en matière condensée. Nous y verrons leurs applications dans un dispositif de mélange de fréquences, de caractérisation des systèmes à deux niveaux présents dans le matériau constituant nos nano-structures, et de détecteur de pression dans un gaz raréfié au bord d'une surface. Pour finir, nous concluons sur l'ensemble de ce manuscrit et du travail effectué durant cette thèse dans le Chap. VI.

Experimental techniques

Contents

II.1 Introduction

Nano-mechanical resonators are continuously attracting more and more interest with the advance of technologies (fabrication, detection, sensitivity) and modeling. The richness and complexity emerging from these devices contribute to many fields which spread from applied to fundamental physics, involving for example micro-fluidics, non-linear phenomena or condensed matter properties. However, in order to use NEMS as tools or probes, it is essential to thoroughly understand their basic properties in the first place. We present in this chapter the experimental techniques that we used in the whole thesis to characterise our resonators.

First of all, we will shortly describe the nano-fabrication processes we use to make silicon and silicon nitride NEMS. To study those devices, we cool them down to temperatures around 1 K in a Helium cryostat and measure them through electrical bond contacts which connect the 4.2 K to the 300 K environment. Using the so-called magnetomotive scheme, we both actuate and detect the NEMS vibration by means of an A.C. applied current and a static magnetic field. By having a side gate electrode close to our resonators, we can tune mechanical mode properties which enables complex dynamics to be generated. Kelvin temperatures are low enough for most of the issues we deal with. However some NEMS research areas require much lower temperatures to be reached (millikelvin, and even sub-millikelvin). This shall be discussed in Chap. V.

The electrical measurement needs then to be calibrated in order to extract in real units (meters, newton) the dynamical properties of the NEMS. We will present the general idea enabling the definition of the injection, the capacitive and the detection lines, using the Joule effect to obtain an in-situ calibration of our resonators.

Last but not least, we present the characteristics of different NEMS we made and compare them with one another. In order to do so, we introduce the concept and the issues of measuring higher modes, and their behaviour as we increase the mode number or the beam length. We then show the dependence of the dissipation and the resonance frequency of the NEMS with respect to the temperature. Finally, we present the displacement response of the resonator from the linear to the anelastic regime, and introduce the so-called Duffing non-linearity which eventually leads to new emerging phenomena and rich physics.

<u>Note on the definition of experimental/theoretical parameters:</u>

Experimentalists and theoreticians often use different notations when it comes to define oscillating frequencies : f (in Hertz) and ω (in rad.s^{-1}), such that $\omega = 2\,\pi\,f$. Since they are relevant either for experimental results or for mathematical expressions, we use in this manuscript both notations depending on the context. Hence for clarity, the definition of a frequency in this thesis always applies for both notations. For instance, defining the loaded linewidth of a resonance Δf_{load} automatically implies the definition of $\Delta \omega_{load} = 2\,\pi\,\Delta f_{load}$.

Along the same lines, experimentalists are used to measure amplitudes in RMS (root mean square) units, while theoreticians use peak. For consistency we present data expressed only in peak units.

II.2   Fabrication of NEMS

In this thesis, we mainly focus on non-linear dynamics of NEMS. Hence we will not particularly require extremely high resonance frequencies (as opposed to the GHz range used for quantum experiments). On the other hand, we need a high enough quality factor to be in the Lorentzian approximation, but the linewidth Δf should be large enough to guarantee a fast enough measurement time $\tau = \dfrac{1}{\pi \Delta f}$ (mainly for practical reasons).

Silicon (Si) and silicon nitride (SiN) vibrating nano-structures are well-known to be robust and the SiN has an in-built tensile stress. Thus the frequency, non-linearity and quality factor can be controlled beforehand essentially on demand, which makes those structures appropriate for our objectives. We present in the following two fabrication techniques used for the two kinds of devices investigated in Chap. III and Chap. IV: doubly-clamped SiN nano-beams and goalpost shaped Si nano-resonators. We relied only on those fabrication techniques.

II.2.1   Silicon goalpost structure

We start from a thick SOI (Silicon On Insulator) wafer with a radius of 20 cm composed of a 150 nm silicon layer over a 1 μm sacrificial silicon oxide layer on top of a silicon under layer (of about 300 μm). After cutting a chip of 1 cm^2, we clean it with both acetone and isopropanol (IPA) and then dry it with nitrogen gas. We bake resist (PMMA 4%) on top of it (about 1 μm thick), print the pattern of the structure we want on it with e-beam lithography and finally develop the resist with a MIBK solution. We evaporate at room temperature an aluminium (Al) layer and using an acetone solution we lift-off both the resist and the Al wherever the e-beam lithography did not flash the resist, leading to an Al mask only where the structure is supposed to be. By means of Reactive Ion Etching with sulfur hexafluoride gas (SF$_6$) we anisotropically etch the Si overlayer on the whole chip except where the Al is present, patterning the structure. The 1 μm oxide is then removed by a chemical vapour hydrofluoric (HF) etching. This step etches also away the oxide underneath the Al mask, which releases the vibrating structure and creates an undercut on the connecting pads. We then remove the Al mask and evaporate a new 30 nm thick aluminium layer on the whole chip. We end up with a 150 nm thick silicon nano-structure covered by an aluminium layer of 30 nm, released from the bulk by a 1 μm gap. All those steps are presented in Fig. II.1a. In Fig. II.2a we show a Scaning Electron Microscope (SEM) picture of the goalpost we use in the following, made by our colleague Jean-Savin Heron [Collin *et al.* 2011b].
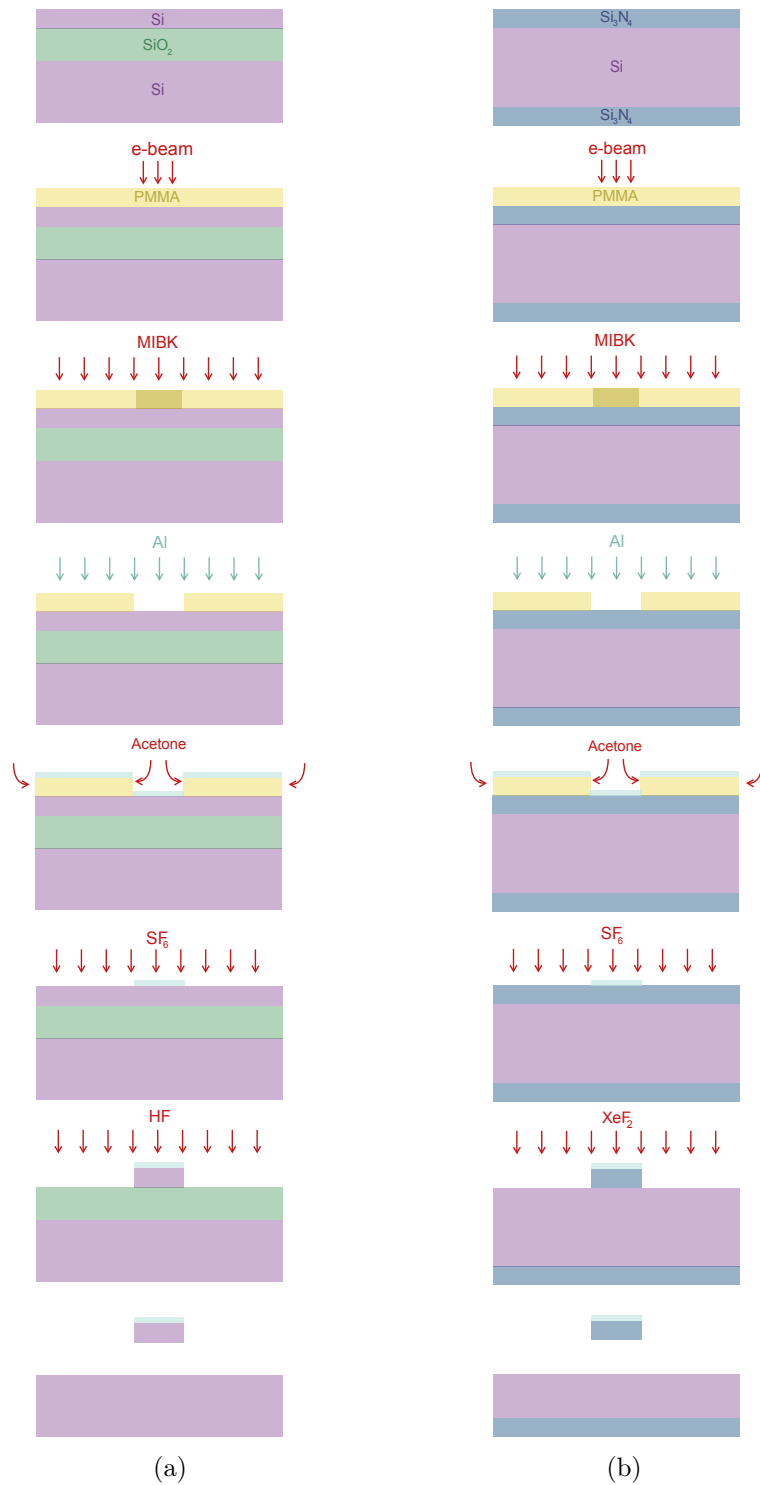
Figure II.1: Schematic of the side view of nano-fabrication processes used for the Si goalpost (*a*) and the SiN doubly-clamped beam (*b*). Each step is described in the text.

<center>(a) (b)</center>
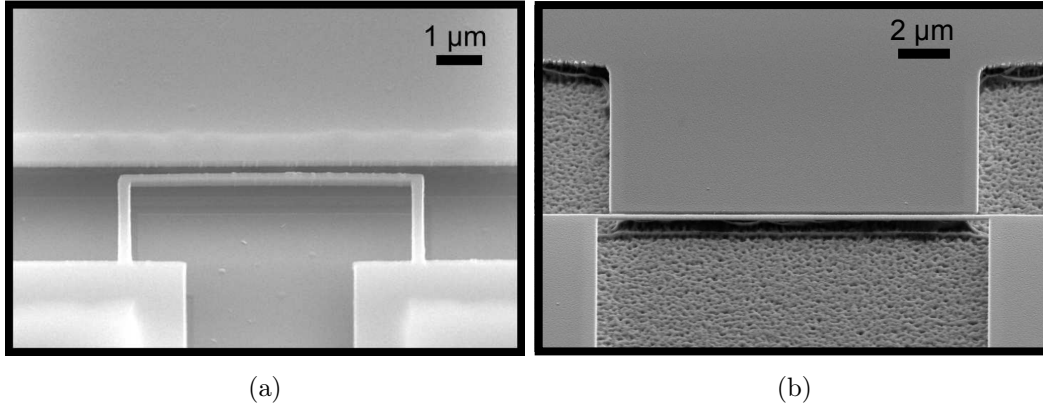
Figure II.2: Scanning Electron Microscope (SEM) pictures of typical nano-structures. *a*: goalpost with paddle of 7 μm and feet of 3 μm long, for a Si thickness of 150 nm with an Al thickness of 30 nm on top of it, and an overall width of 280 nm. *b*: 15 μm long doubly-clamped beam, for a SiN thickness of 100 nm and an Al thickness of 30 nm, and an overall width of 250 nm. Note the presence of a gate electrode close to the nano-devices (with a gap of 100 nm from the resonators). In our experiments, the NEMS are vibrating out-of-plane.

II.2.2 Silicon nitride doubly-clamped beam

The wafer we used for this nano-wire is made of silicon of about 300 μm thickness coated with a silicon nitride layer of 100 nm on both faces. The fabrication technique is then similar to the one used for the goalpost structure, except that we etch the silicon using XeF$_2$ to release the beam. We obtain a 100 nm thick silicon nitride beam with a 30 nm thick aluminium layer which is released from the bulk silicon by a gap which size depends on the XeF$_2$ final etching exposure time. The aluminium mask can be kept as conducting layer or equivalently can be removed in a wet etch and replaced by a full field evaporation of metal. Again, we present the different steps in Fig. II.1b. In Fig. II.2b we show an example of the resulting NEMS. We used this fabrication technique to obtain doubly-clamped beams of lengths ranging from 10 μm to 300 μm. Most of the doubly-clamped beams we used were made by our collaborators Kunal Lulla and Thierry Crozes.

When the fabrication process is validated by our SEM observation, the devices are electrically tested and finally mounted onto the sample holder. We glue them using GE-Varnish, and bond the NEMS contacts to the electrical tracks of the sample holder using 30 μm diameter aluminium wires. The metallic experimental cell is then hermetically sealed using an indium ring.

II.3 General set-up

II.3.1 Cooling down to Kelvin temperatures

In the experiments presented in the next chapters, cryogenic temperatures are used in order to ensure optimal operating condition: we benefit from cryogenic vacuum, less electrical and mechanical noise, and an overall better NEMS quality (high quality factors, smaller thermal contraction, less degassing).
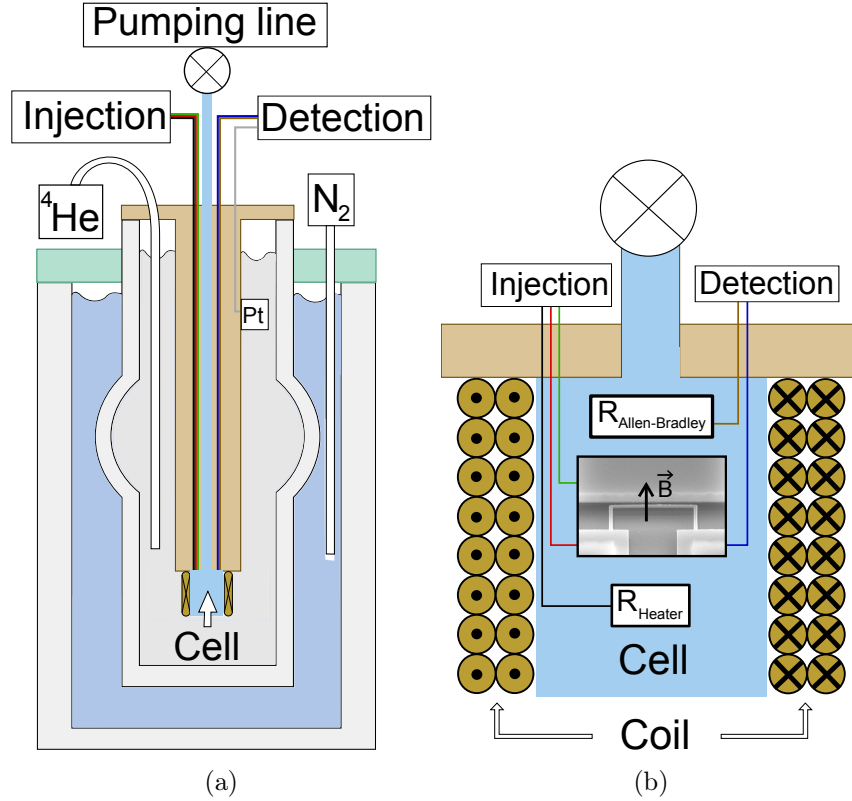
Figure II.3: Schematic of our 4.2 K cryostat (*a*) and the experimental cell (*b*). The cryostat consists of two baths (liquid N_2 and ^{4}He) separated by a vacuum chamber, to cool down the experimental cell at 4.2 K. This cell is connected to the 300 K environment through electrical wires, with injection and detection lines, surrounded by a coil. The goalpost picture is taken as an example.

As presented in Fig. II.3a, our cryostat consists of two baths. The first one is filled by liquid nitrogen (N_2) and is separated from the second bath by vacuum. The second bath is filled with liquid Helium and cools down to 4.2 K the outside of our experimental cell. Prior to cooling, the cell is pumped to about 10^{-4} mbar, and the remaining gas is then adsorbed (cryo-pumped) on the inner surfaces leading to a vacuum $< 10^{-6}$ mbar at low temperatures. A pumping line connected to the ^{4}He bath enables to reach temperatures down to 1.5 K.

The cell (Fig. II.4) is soldered to a pump line at the bottom of a stick. A few copper disks are fixed along it to reduce thermal radiation from outside and electri-

cal lines link the 4.2 K to the 300 K environment. Beside the NEMS there were two thermometers, a heater and a coil connected within the cryostat with twisted (constantan and copper) wires. The first thermometer is a platinum resistor bolted on the first copper screen and is useful for temperatures above 50 K typically, verifying thermalisation at nitrogen temperatures, while the second one is an Allen-Bradley carbon resistance appropriate for liquid Helium temperatures. This last thermometer is mounted directly on the sample holder, and defines the NEMS temperature. The heater, also fixed to the sample holder, is a 100 Ω resistance and enables to regulate the sample temperature while the cell remains at Helium bath temperature. The coil is made of superconducting niobium-titanium wires enabling to reach fields up to 1.2 T. We used an HP 34401A voltmeter to measure the resistance of the platinum thermometer and a Kepco current generator to drive the coil. The sample's thermometer and heater are connected to a Barras-Provence resistance bridge. The sample holder temperature can then be regulated from 1.5 K to 30 K.
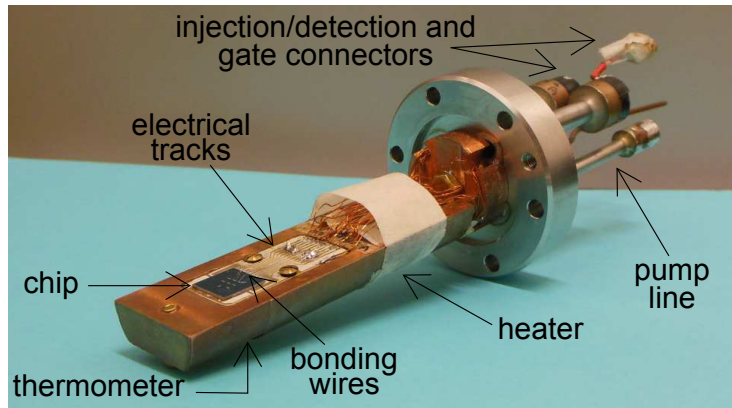
Figure II.4: Picture of the inner cell in which we glue the chip, as described in the text. Heater and thermometers are fixed on the back of the copper sample holder.

II.3.2   Actuation and detection of NEMS

As shown in Fig. II.3b and in the schematic of Fig. II.5, we use three electrical lines to actuate and detect the NEMS: an injection line, a detection line and a line connected to a gate electrode. In the electrical language, the NEMS resonance is equivalent to a $r\,\ell\,c$ circuit which equivalent parameters can be computed from the mechanical ones [Cleland & Roukes 1999].

Since we are dealing with vibrating nano-structures we need a way to drive them resonantly. One standard method of exciting the NEMS is to use the magnetomotive scheme [Cleland & Roukes 1999]. We apply an A.C. current $I_i = I_0 \cos(\omega\,t)$ at frequency ω through the NEMS using an A.C. voltage generator at 300 K biasing a 1 kΩ drive resistance kept at 4.2 K. The voltage generator is a Tektronix AFG 3252 which can deliver a voltage drive V_i from DC up to 240 MHz over about two orders of magnitude in amplitude (tens of mV to V). We used 20 and 40 dB attenuators to
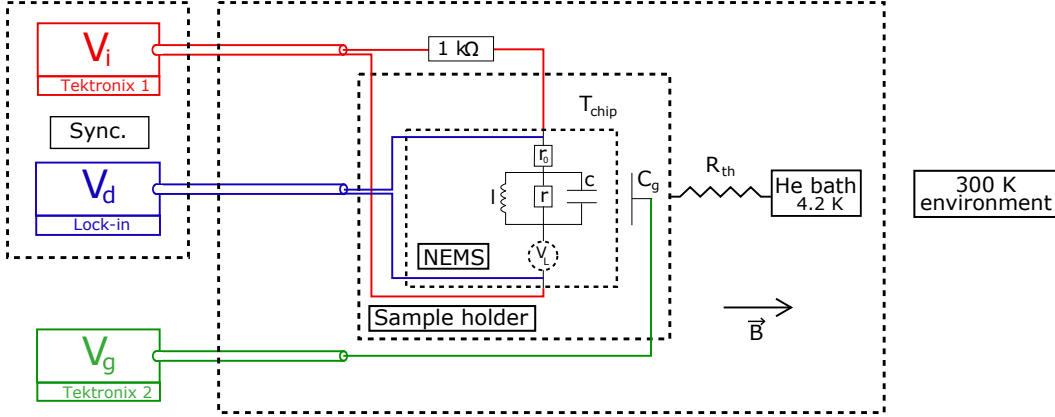
Figure II.5: Schematic of the electrical circuit in our experiment. We drive the NEMS with a voltage V_i, measure an output voltage V_d and modulate a gate electrode V_g capacitively coupled to the NEMS.

reach the μV range needed for our experiments. In order to electrically protect the devices, we added a grounding box which connects/grounds the cryostat lines from the 300 K electric circuit. A static magnetic field $\overrightarrow{B} = B\,\vec{y}$ perpendicular to the NEMS length and which is assumed to be constant and unidirectional on the whole chip is also present. Using both inputs, an infinitesimal Laplace force is generated on each beam sub-element $\overrightarrow{dz'}$:

$$d\overrightarrow{F_L} = I_i \, \overrightarrow{dz'} \times \overrightarrow{B} = I_i \, B \, dz \left(\vec{z'} \times \vec{y} \right), \tag{II.1}$$

with $\overrightarrow{dz'} = dz\,\vec{z'}$ the path followed by the drive current along the NEMS of length l, as presented in Fig. II.6. Since the element $\overrightarrow{dz'}$ moves in the $\vec{x}$ direction under this excitation with an amplitude $\Psi_n(z)\,x_n(t)$, the power associated to the mode n motion is:

$$P_n = \int_l \Psi_n(z) \, \dot{x}_n(t) \, I_i \, B \, \cos\left[\theta(z)\right] \, dz, \tag{II.2}$$

with $\cos\left[\theta(z)\right] = \frac{1}{\sqrt{1+(\Psi'_n x)^2}}$, Ψ_n is the mode shape and x_n its amplitude. The cosine term can always be very well approximated by 1 in all our experiments, and P_n can be written:

$$P_n = I_i \, l \, B \, g_n \, \dot{x}_n(t), \tag{II.3}$$

with $g_n = \frac{1}{l} \int_l \Psi_n \, dz$ a mode-dependent parameter. From Eq. (II.3) , the effective force acting on mode n is immediately defined as:

$$\overrightarrow{F_{L,n}}(t) = g_n \, I_i(t) \, l \, B \, \vec{x}. \tag{II.4}$$

For a doubly-clamped beam in its first flexure, defining $x_n(t)$ as the amplitude of the mid-point motion one calculates $g_{0,h} \approx 0.637$ (high stress) and $g_{0,l} \approx 0.523$
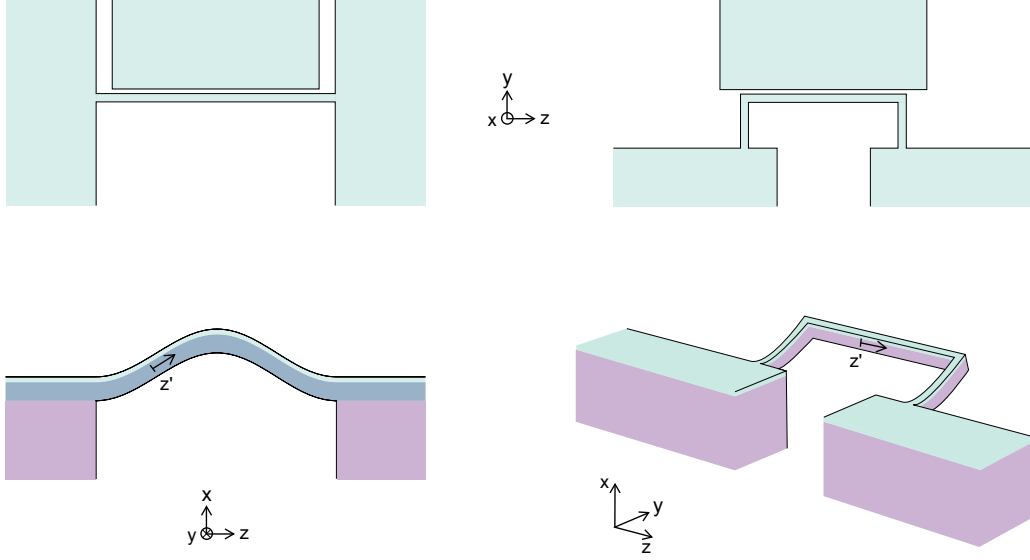
Figure II.6: Schematic of a top view and of a side view of the first flexural mode of a doubly-clamped beam and of a goalpost structure (respectively top and bottom, left and right). The path followed by the current is represented on the side view by the $\vec{z'}$ axis and is slightly misaligned from the fixed $\vec{z}$ axis by the NEMS motion, represented by the mode shape Ψ_n of the driven mode n (doubly-clamped) or the paddle distortion (goalpost, almost straight).

(low stress). For a goalpost structure, one simply has $g_0 \approx 1$ (the paddle bar remains essentially straight).

The mechanical susceptibility of the beam transduces the force $\overrightarrow{F_{L,n}}$ into a displacement $x_n \vec{x}$, and solving the second law of Newton we can deduce the displacement amplitude of the NEMS for mode n, in the linear regime limit:

$$\ddot{x} + \Delta\omega_n \dot{x} + \omega_{0,n}^2 x = \frac{F_{L,n}}{m_n}, \tag{II.5}$$

with $\Delta\omega_n$ quantifying the dissipation experienced by the motion and $\omega_{0,n} = \sqrt{\frac{k_n}{m_n}}$ the resonance frequency. The mass m_n and spring constant k_n associated to the mode n can be defined from the kinetic and flexural/tensioning energies involved in the motion:

$$E_m = \frac{1}{2} \dot{x}_n^2 \int_l \rho \, e \, w \, \Psi_n^2(z) \, dz = \frac{1}{2} m_n \dot{x}^2, \tag{II.6}$$

$$E_k = \frac{1}{2} x_n^2 \int_l \left[E \, I \left(\frac{\partial^2 \Psi_n(z)}{\partial z^2} \right)^2 + T \frac{\partial^2 \Psi_n(z)}{\partial z^2} \Psi_n(z) \right] dz = \frac{1}{2} k_n x^2, \tag{II.7}$$

with ρ the mass density of the beam and E its Young's modulus. The second moment of inertia is defined as $I = \frac{1}{12} w \, e^3$, with w the width and e the thickness.

Depending on the in-built stress $\frac{T}{w\,e}$ in the material, one of the two terms in the integral of Eq. (II.7) can be neglected. Thus in our devices, the spring constant k_n is defined either by the Young's modulus for the low stressed goalpost structures or by the stress for the high stressed doubly-clamped ones.

From now on, we shall drop the index n for simplicity. In the limit of high quality factor $Q = \frac{\omega_0}{\Delta\omega}$, the displacement x is described by a Lorentzian in the frequency domain:

$$x\left(\omega\right) = \frac{F_L}{2\,m\,\omega_0} \frac{1}{\left(\omega_0 - \omega\right) + i\,\frac{\Delta\omega}{2}} = \chi\left(\omega\right) F_L, \qquad (II.8)$$

where $\chi\left(\omega\right)$ is called the mechanical susceptibility. Now that the NEMS can be excited, the next step is to measure its oscillation through the detection line.

Since the NEMS oscillates perpendicular to $\overrightarrow{B}$, it cuts the field lines by spanning an effective surface S, and the corresponding magnetic flux is written:

$$d\Phi = \int_l \overrightarrow{B} \cdot \vec{y}\, d^2 S = B \int_l \Psi\, dz' . dx \qquad (II.9)$$

which produces a voltage source due to the Lenz induction law:

$$V_L = -\dot{\Phi}, \qquad (II.10a)$$
$$V_L = -g\,B\,l\,\dot{x}, \qquad (II.10b)$$

with g the mode parameter already introduced. For goalpost devices, the area spanned is an arc of circle which brings a cosine term in the scalar product $\left(\vec{y'}.\vec{y}\right)$. However, for our experiments this cosine can always be approximated to 1 (Fig. II.7).
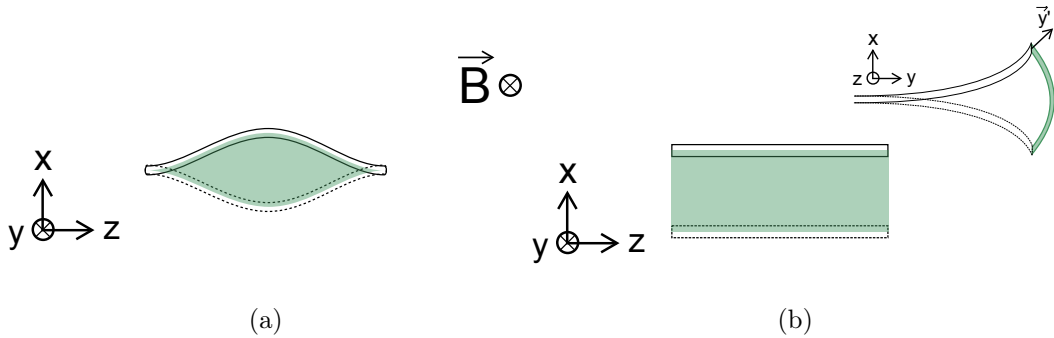
Figure II.7: Schematic of the surface S (in light green) cutting the field lines, leading to an electromotive voltage V_L for (a) a doubly-clamped beam and (b) a goalpost device (only the paddle is represented in the main figure, while only one foot is represented in the inset). Note in the latter case that the surface is patterned onto an arc of circle (inset of b), due to the nature of the mode's motion. However, for our small displacement, we can approximate it to a plane surface.

By measuring this voltage we can deduce the displacement amplitude. The NEMS is connected through a four point measurement scheme to a lock-in detection enabling the direct measure of the NEMS response. Nevertheless, the voltage

measured V_d does not directly correspond to the NEMS amplitude, one should first subtract the ohmic voltage $I_i r_0$ due to the metallic conductor: indeed the aluminium layer of the NEMS is not superconducting above 1.5 K. We used a SR844 Lock-in amplifier with a 1 MΩ detection input referenced on the drive current frequency, which enables to extract the in-phase V_X and out-of-phase V_Y components of the motion contained within V_L, such that $|V_L| = V_R = \sqrt{V_X^2 + V_Y^2}$. Our phase reference thus directly comes from the Tektronix voltage generator V_i, and gives:

$$V_X = \frac{g\,B\,l\,F_L}{2\,m} \frac{\frac{\Delta\omega}{2}}{(\omega_0 - \omega)^2 + \left(\frac{\Delta\omega}{2}\right)^2}, \quad V_Y = \frac{g\,B\,l\,F_L}{2\,m} \frac{\omega_0 - \omega}{(\omega_0 - \omega)^2 + \left(\frac{\Delta\omega}{2}\right)^2}. \quad \text{(II.11)}$$

Note that while the displacement amplitude is linear with the magnetic field, the measured voltage depends quadratically on it (since $F_L \propto B$). Moreover, the detected voltage is simply proportional to the motion, and one verifies the conservation of injected energy: $|V_L|\,I_i = F_L\,|\dot{x}|$.

From Eq. (II.1) and Eq. (II.11) we can now measure the motion of our NEMS in one of its out-of-plane flexural modes, as seen in Fig. II.8, from which we see that $\Delta\omega$ defines the full width at half maximum of the Lorentzian peak (called simply the linewidth) and ω_0 is its position. V_{max} is the height of the peak at resonance (V_X component), where the V_Y component is zero.
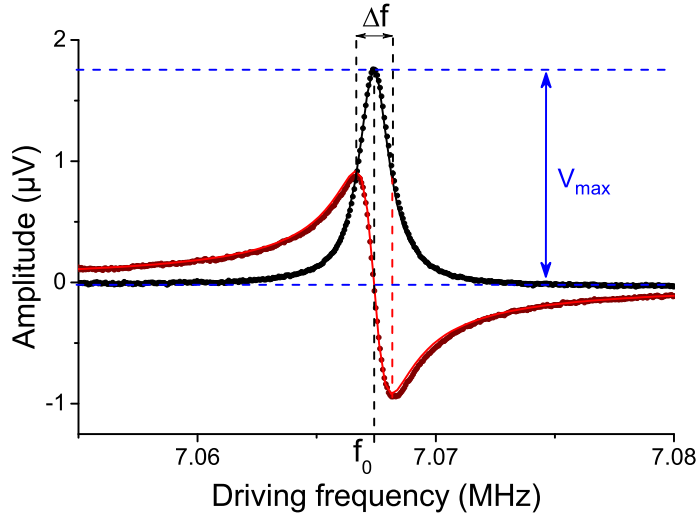
Figure II.8: Resonance line of the goalpost first flexural mode measured at 4.2 K with the lock-in amplifier. The in-phase (black) and quadrature (red) components of the signal are presented in volt units. Lines are fits, using Eq. (II.11), from which we can extract both resonance frequency and linewidth (here $f_0 = 7.07$ MHz and $\Delta f = 1500$ Hz). V_{max} is the height on resonance of the peak.

II.3.3 Driving higher harmonics

Ideal oscillating systems have an infinite number of modes which differ by their resonance frequency and characteristics. The first flexural modes $\Psi_n(x)$ (with $n = 0, 1, 2$) are represented in Fig. II.9.
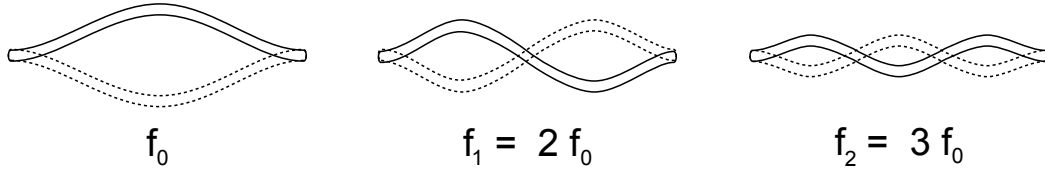
Figure II.9: Schematic of the flexural mode shapes Ψ_n of an ideal string with perfect clamps. We represent here the three first modes along the x axis. In this ideal high stress picture, the scaling of the resonance frequency for each mode is $f_n = (n+1) f_0$.

(a)   (b)
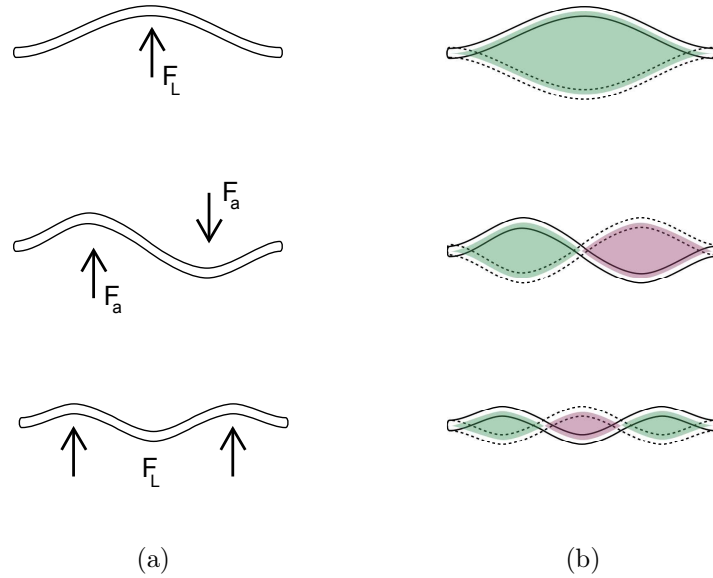
Figure II.10: Schematic of our actuation (a) and detection (b) technique on a beam, affecting the capability of measuring different modes. a: only an asymmetric force F_a could drive an odd mode, which cannot be created with our symmetric Laplace Force F_L. b: with an odd mode, the Lenz law would generate an average zero electromotive voltage V_L.

With our real resonators and high impedance set-up, we are able to detect some of these higher harmonic flexural modes. However the magnetomotive scheme limits us to modes with an even number of nodes because of both the actuation and detection set-up symmetry (the g_n factor introduced in Sec. II.3.2 is otherwise zero).

On one hand the Laplace force we create cannot generate an asymmetric excitation
(Fig. II.10a) and on the other hand the electro-motive voltage we measure from the
flux cut by the NEMS should not be cancelled by its own mode shape (Fig. II.10b).
Hence we have only access to half of the flexural modes of our beams (fundamental
mode $n = 0$, second harmonic $n = 2$, fourth harmonic $n = 4$, ...).

n = 0   n = 2   n = 4   n = 6
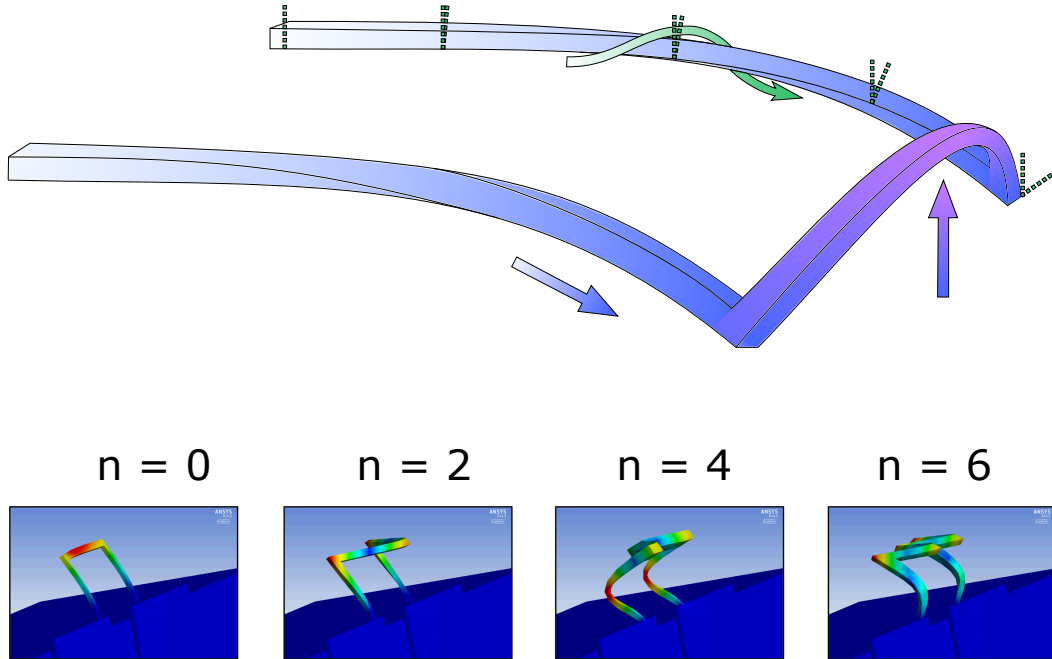
Figure II.11: *Top*: schematic of the distortion of the goalpost as we drive it. Three
effects, each one acting on the other, are involved: the feet bend (blue), a torsion is
applied on each foot (green) and hence the paddle bends (purple). *Bottom*: ANSYS
(finite element analysis software) simulations of the four first symmetric modes of
our goalpost, exhibiting exotic shapes, generated by our co-worker Jean Guidi.

However the modes of the goalpost structure have a different behaviour due
to their more complex geometry. While the first mode bends in a rather intuitive
way, the higher mode shapes result from an intrinsic geometrical coupling between
the feet and the paddle (Fig. II.11) [Collin *et al.* 2014]. Due to this coupling, the
magnetomotive scheme will again reduce the number of modes we have access to:
antisymmetric modes cannot be detected by our scheme (one foot bending one way
and the other foot bending the other way, the paddle experiencing a node in the
center, see Fig. II.12). Furthermore, the detection of some symetric modes can be
rather difficult because of a particularly low g_n parameter, caused by the strong
bending experienced by the paddle (see Fig. II.12).

(a)   (b)
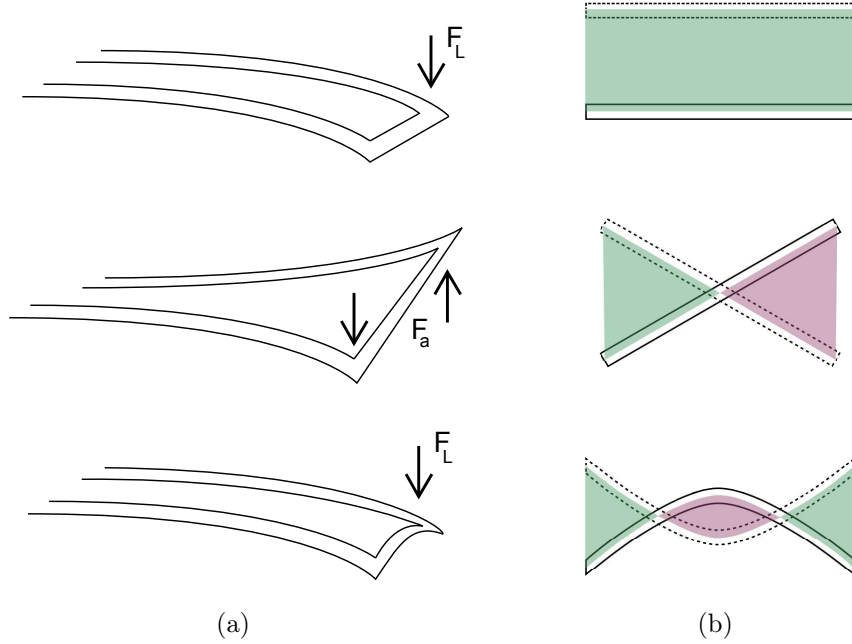
Figure II.12: Schematic of our actuation (a) and detection (b) technique on a goalpost device. *a*: side view of the structure. Only modes with symmetric feet oscillation can be actuated. *b*: front view (only the paddle is represented). As for the beams, the modes we cannot drive are also impossible to detect. However, for the symmetric ones, the electromotive voltage V_L measured might be considerably reduced due to the distortion of the paddle, to the point we might not have the resolution to detect it.

II.3.4   The gate electrode

The magnetomotive scheme is a robust technique used to drive the NEMS, but implementing an extra coupling with a gate electrode gives access to additional capabilities (Fig. II.2a and Fig. II.2b). In most samples this gate is at 100 nm away from the NEMS and will be controlled by a voltage generator through the capacitive line. By biasing the gate, an electric field is generated which affects the NEMS dynamics through a force:

$$\overrightarrow{F_g} = \frac{1}{2}\,\frac{\partial C_g}{\partial x}\,V_g^2\,\vec{x}, \tag{II.12}$$

with C_g the capacitance between the gate and the NEMS and V_g the voltage applied onto the gate. Obviously, the electric field also couples to the in-plane motion through a similar expression to Eq. (II.12) but since these modes are never resonant, this degree of freedom can be safely neglected (as well the $\vec{z}$ gradient which couples to the longitudinal modes is irrelevant). For small NEMS' displacements (typically $x \leq 100$ nm), we can use the Taylor expansion approximation:

$$\frac{\partial C_g(x)}{\partial x} = \frac{\partial C_g(0)}{\partial x} + \frac{\partial^2 C_g(0)}{\partial x^2}\,x + \frac{1}{2}\,\frac{\partial^3 C_g(0)}{\partial x^3}\,x^2 + \frac{1}{6}\,\frac{\partial^4 C_g(0)}{\partial x^4}\,x^3 + ... \tag{II.13}$$

For doubly-clamped structures, the motion generates also a tension in the beam described by:

$$\delta T = E\,w\,e \left[\int_l \frac{\sqrt{1 + (\Psi'(z)\,x + \Psi_s'(z)\,x_s)^2}}{l}\,dz - l \right]$$

$$\approx \frac{E\,w\,e}{2} \left[x^2 \int_l \frac{\Psi'^2(z)}{l}\,dz + x_s^2 \int_l \frac{\Psi_s'^2(z)}{l}\,dz + 2\,x\,x_s \int_l \frac{\Psi'(z)\,\Psi_s'(z)}{l}\,dz \right], \quad \text{(II.14)}$$

with $\Psi_s'(z)\,x_s$ the static (or non-resonant) distortion generated by the voltage applied onto the gate through $\frac{\partial C_g(0)}{\partial x}$. The first term in the bracket generates a non-linear spring constant $\propto x^3$ (Sec. II.3.5) while the second one is a static modification of the in-built tension T [Eq. (II.7)]. The last one modulates the stress in the beam $\propto x$, which in turn generates an effective non-linear term $\propto x^2$ in the dynamics. This is essentially what is described in Ref. [Kozinsky *et al.* 2006]. For cantilevers in the first flexure, only the main x-dependent expansion of $\frac{\partial C_g(x)}{\partial x}$ is relevant (there is no δT).

Introducing this force in Eq. (II.5), we obtain:

$$\ddot{x} + \Delta\omega\,\dot{x} + \left(\omega_0^2 - \frac{1}{2\,m}\frac{\partial^2 C_g(0)}{\partial x^2}\,V_g^2 \right) x$$

$$- \frac{1}{4\,m}\frac{\partial^3 C_g(0)}{\partial x^3}\,V_g^2\,x^2 - \frac{1}{12\,m}\frac{\partial^4 C_g(0)}{\partial x^4}\,V_g^2\,x^3 = \frac{F_L}{m} + \frac{1}{2\,m}\frac{\partial C_g(0)}{\partial x}\,V_g^2. \quad \text{(II.15)}$$

We see that each order of the expansion acts on the NEMS in a different way [Collin *et al.* 2012]:

- The first order $\dfrac{\partial C_g}{\partial x}$ can be used as a driving force. By applying an A.C. voltage on the gate at half the resonance frequency ω_0 we excite the NEMS without the magnetomotive actuation. Note that applying a D.C. voltage on the gate will only slightly bend the NEMS to a fixed intrinsic distortion (negligible in all experiments).

- The second order $\dfrac{\partial^2 C_g}{\partial x^2}$ enables to tune the spring constant k, which allows to statically shift the resonance frequency (see Sec. II.4.3 and Fig. II.20) or to drive the NEMS in a parametric regime (modulating at twice the resonance frequency) [Collin *et al.* 2011b].

- The third and fourth order terms are non-linear parameters that transform the Lorentzian shape of the resonance into a "Duffing-type" lineshape, leading to new physics. The non-linear description of the resonance is presented below in Sec. II.3.5.

Using each of these effects, we can measure in-situ the actual values of the coefficients entering in Ref. Eq. (II.13), as described in [Collin *et al.* 2012]. For the ones of importance to our work (the static shift of the resonance frequency

and the fourth order non-linear term), see Fig. II.21 and Fig. II.35 below in this chapter. It is important to note that, while this voltage biasing is a powerful way of attaining new physics, it is limited. Above a NEMS displacement of about 100 nm (typically the gap between the gate and the resonator), not only the Taylor expansion loses meaning, but also the capacitive coupling smoothly vanishes. For this reason, we paid attention not to use the gate with such amplitudes, keeping the Taylor expansion meaningful.

II.3.5   Non-linearities in nano-resonators

The NEMS dynamics described in the section above (Sec. II.3.2) corresponds to the response of an ideal linear resonator. For large displacement amplitudes and due to constraints in the materials or in the geometry, the dynamics becomes more complex and we need to introduce non-linearities in Eq. (II.5). The most well-known non-linear model reads:

$$\ddot{x} + \Delta\omega\, \dot{x} + \omega_0^2\, x + \gamma\, x^3 = \frac{F_L}{m}, \tag{II.16}$$

with γ the so-called "Duffing" non-linear coefficient. This non-linear equation modifies the Lorentzian linear mechanical susceptibility given in Eq. (II.8) into:

$$\chi_{Duff}(\omega) = \frac{1}{2\,m\,\omega_0} \frac{1}{(\omega_0 + \beta\, x^2 - \omega) + i\,\frac{\Delta\omega}{2}}, \tag{II.17}$$

with $\beta = \frac{3\gamma}{8\omega_0}$ which shifts the resonance frequency quadratically with respect to the displacement amplitude x. This results in a bending of the resonance line upwards for $\beta > 0$ and downwards for $\beta < 0$. Moreover, a characteristic feature of this equation is that two motional states exist for $x > x_c$ with:

$$x_c^2 = \frac{\sqrt{3}}{2} \frac{\Delta\omega}{\beta}, \tag{II.18}$$

from which arises new phenomena like bistability (see Sec. II.5.3).

However, on basic grounds the Duffing term is not the only source of non-linearities that comes into play. Materials features outside of the linear (elastic) range are discussed in Sec. II.5.4. Here, we consider only non-linear effects of geometric origin, namely the curvature of strongly deflected cantilevers or the elongation of doubly-clamped beams. One way of defining the most generic 1D non-linear equation is to expand to third order the energy balance in terms of a non-linear Taylor series of the mode shape. Rewriting the dynamics equation [Collin *et al.* 2010a] we obtain:

$$\ddot{x}\left(1 + \alpha_1\, x + \alpha_2\, x^2\right) + \dot{x}^2\left(\frac{\alpha_1}{2} + \alpha_2\, x\right)$$
$$+\Delta\omega\, \dot{x}\left(1 + \bar{\alpha}_1\, x + \bar{\alpha}_2\, x^2\right) + \omega_0^2\, x + \kappa\, x^2 + \gamma\, x^3 = \frac{F_L}{m}, \tag{II.19}$$

with α_i, $\bar{\alpha}_i$, κ and γ parameters defined from the integrated non-linear distortion of the mode over the structure. The α_i parameters can be called inertial non-linear coefficients, while the $\bar{\alpha}_i$ impact the damping term $\Delta\omega\,\dot{x}$. The parameters κ and γ are restoring force non-linear coefficients.

In our case of a sinusoidal driving force, we can use an extended version of the Landau-Lifshitz method to solve Eq. (II.19) (see [Collin *et al.* 2010a]). This leads to a modification of the linear mechanical susceptibility which reads exactly like Eq. (II.17), but with an effective Duffing coefficient:

$$\beta_{eff} = \frac{3\,\gamma}{8\,\omega_0} + \omega_0\left(\frac{\alpha_1^2}{16} + \frac{\alpha_1\,\kappa}{4} - \frac{5\,\kappa^2}{12} - \frac{1}{4}\,\alpha_2\right), \qquad \text{(II.20)}$$

written here in the high-Q limit ($Q = \frac{\omega_0}{\Delta\omega} \gg 1$). This neglects an extra $\propto x^2$ correction on the linewidth parameter in Eq. (II.17) which is proven to be irrelevant experimentally. This in turn implies that the $\bar{\alpha}_i$ terms do not play any role in the dynamics we study and can be dropped already from Eq. (II.19). While Eq. (II.19) involves different non-linear terms from different orders, their overall signature on the resonance line reduces to a quadratic shift of the resonance frequency, just as in a Duffing oscillator where the only non-zero non-linear coefficient is γ. Note that we stopped the expansion to the third order in Eq. (II.19), since all higher order terms do not contribute to the $\propto x^2$ correction in the lineshape.

As a result, measuring such a shift in the resonance frequency does not directly imply that we are dealing with a strict Duffing oscillator. For a doubly-clamped beam (or a string in the high stress limit), the main source of non-linearity is stretching which brings a $\gamma\,x^3$ into the equation [first term in Eq. (II.14)]. All the other terms are much smaller and can thus be neglected: such NEMS can thus be considered as proper implementations of Duffing resonators [Nayfeh & Mook 1995]. On the other hand, for a cantilever (or a goalpost) structure, all the terms are supposedly of the same order. Moreover, in the case of nanomechanical devices, they somehow cancel in Eq. (II.20) leading to particularly small experimentally reported β_{eff} coefficients [Villanueva *et al.* 2013]. Since we generate the non-linearity in our goalpost devices through the gate electrode with the additional terms $\gamma \propto V_g^2$ (κ being much smaller than γ [Collin *et al.* 2012]), we can again consider that the voltage-biased goalpost NEMS is an excellent implementation of the Duffing oscillator. While being our basis for the analysis in Chap. III and Chap. IV, non-linear terms beyond the Duffing model could be the cause of deviations between modeling and experimental results. Indeed, the way these coefficients combine within β_{eff} in a frequency-sweep measurement (or equivalently a time decay, [Collin *et al.* 2010a]) has no reason to be identical to the one leading to the effective barrier height in the bifurcation process, Chap. IV, or mode-coupling strength, Chap. III.

Considering the non-linearity of the devices we measured in this thesis, the Duffing equation Eq. (II.16) shall be sufficient to describe all the complex dynamics we studied, and we assume from now on $(\alpha_i, \bar{\alpha}_i, \kappa) = 0$.

II.4 Calibration

The calibration of the experimental set-up is of crucial importance for the experiment presented in the next chapters, especially for the bifurcation phenomenon (Chap. IV), since we want to *quantitatively* understand the physics in those experiments. In a standard R.F. set-up, the line impedance matches 50 Ω. With this technique, the transmission is optimal (no reflection) but the NEMS device is strongly loaded by its electric environment, (see Sec. II.4.1).

Contrarily in our experiments (Fig. II.13), while the voltage generators are 50 Ω we chose to measure the NEMS in a high impedance environment. The drawback of this set-up is that it generates lossy and uncontrolled transmission characteristics that require a thorough in-situ calibration. Those losses change with the end impedance mismatch, which itself depends on the resistance of the device (which scales as we change the length of the beams, from 10 μm to 300 μm). We hence need to perform this calibration essentially for each sample. As an example, we present in the following the calibration of a goalpost resonator, the technique being the same for the other NEMS.
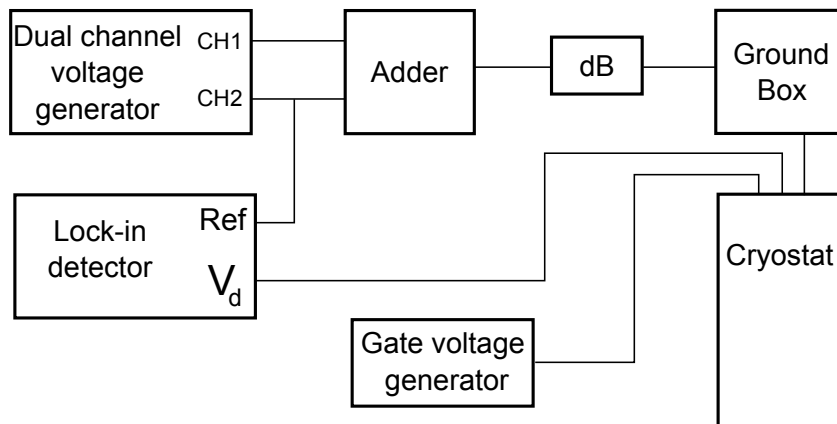
Figure II.13: Experimental set-up for the calibration procedure. Two channels (CH1 and CH2) of the generator are combined in the injection line through an adder. The driving force channel is split to be used as a reference for the lock-in. To prevent any electrical shocks while changing the set-up configuration, we added a grounding box just before the cryostat. We measure the output signal with the lock-in amplifier, as described in Sec. II.3.2.

II.4.1 The loading correction

First of all, we need to take into account the environment's finite impedance effect on the measured resonance frequency ω_0 and linewidth $\Delta\omega$. Indeed, the magnetomotive scheme we use affects the measurement of the NEMS properties due to the presence of the magnetic field, as presented in Ref. [Cleland & Roukes 1999]. The resonator can be modeled as an electrical component with an inductor l, a capacitor c and a resistance r in parallel (Fig. II.5). Since the impedance seen by the NEMS ($Z_{ext} = R_{ext} + i\,X_{ext}$) is non-zero, it loads in parallel the $r\,l\,c$ component which shifts up the resonance frequency and broadens the linewidth:

$$\omega_{loaded} = \omega_0 \sqrt{1 + \frac{X_{ext}}{|Z_{ext}|^2} \frac{g^2\,l^2}{\omega_0\,m} B^2} \tag{II.21a}$$

$$\Delta\omega_{loaded} = \Delta\omega \left(1 + \frac{R_{ext}}{|Z_{ext}|^2} \frac{g^2\,l^2}{\Delta\omega\,m} B^2\right). \tag{II.21b}$$

In our set-up configuration, the dissipative real part of the external impedance has always been the major contribution in this correction, such that $R_{ext} \gg X_{ext}$ and $\omega_{loaded} \approx \omega_0$. Even though the aim is to maximise R_{ext}, the correction to the linewidth can never be neglected completely: a quadratic magnetic field dependence in the linewidth is always detected. For most experiments, we need fields of about 1 T, which alters the linewidth measured from as little as a few percent up to a factor of 200 depending on the NEMS structures (Fig. II.14).

(a)   (b)
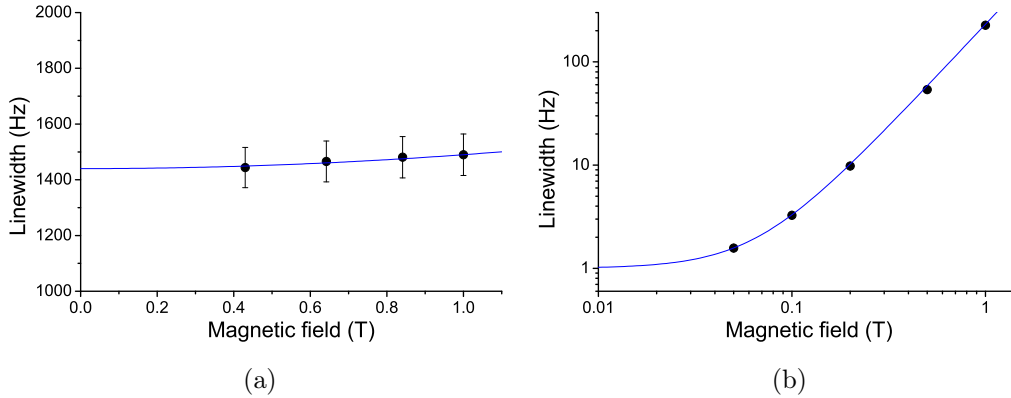
Figure II.14: Loading effect of the magnetic field on the linewidth measured for (a) a 3 μm x 7 μm goalpost and (b) a 300 μm doubly-clamped beam. Note the logarithmic scale in the latter. The blue lines are quadratic fits to the data, which enable to extrapolate the intrinsic linewidth of the NEMS to (a) 1440$\pm$70 Hz and (b) 1$\pm$0.3 Hz.

Let us point out that the linewidth $\Delta\omega$ of the NEMS does not change, it is just our measurement technique that depends on the field and requires a B^2 correction to extract $\Delta\omega$ from $\Delta\omega_{loaded}$. Furthermore, the applied current splits in the same proportion between environment and NEMS; thus the actual drive current has to be calculated properly for quantitative characterisations.

II.4.2 The injection line

The basic idea of the calibration technique of the lines is to heat the NEMS by means of the Joule effect, scaling onto one another the thermal drifts measured for different excitation frequencies [Collin *et al.* 2012]. The phenomenon is genuinely local, and relies only on the NEMS thermal properties: we achieve an in-situ calibration, which does not require any extra electric connections.

Because the current needed to heat the NEMS is orders of magnitude above the current needed to drive it, we used a home-made adder (made by our electronic shop colleague Julien Minet) to add both heating and driving signals in the injection line (Fig. II.15). This adder has two 50 Ω inputs and a high impedance output, with a bandwidth of 100 MHz, a maximum input voltage of about 1 V_{rms} and which has a constant gain of 1.9 over the frequency range we explored (always below 10 MHz for the fundamental harmonic). We used both outputs of the Tektronix voltage generator, one to inject a drive current to the NEMS of about 100 nA enabling the measurement of a linear mechanical resonance, and the other one to inject a heating current $I_h = I_{h,0} \cos(\omega_h t)$ ramping from typically 10 μA to 100 μA (device resistance r_0 from 100 Ω to about 3 kΩ).
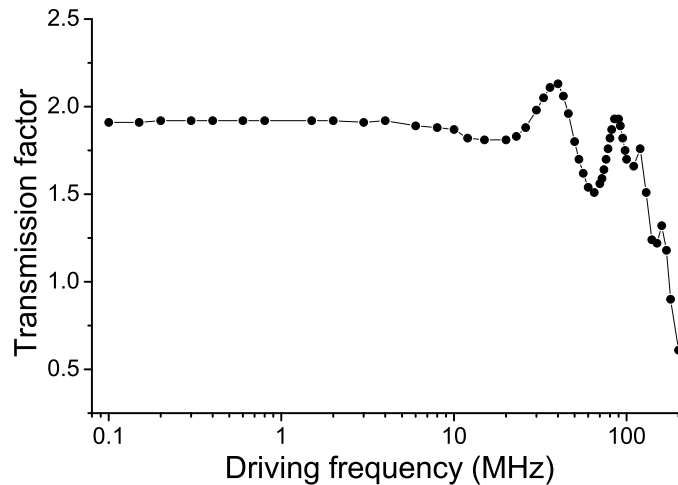
Figure II.15: Transmission of the active adder as a function of the driving frequency for a drive amplitude of 300 mV$_{rms}$. The small fluctuation between 10 MHz and 100 MHz is due to the finite length of our cables.

The losses in the lines due to the impedance mismatch are frequency dependent. To detect them we need a frequency independent technique which will not alter our calibration: the Joule effect. The applied current I_h leads to a heating power $\propto I_{h,0}^2 \frac{1+\cos(2\omega_h t)}{2}$ of which only the static component will be relevant. By heating the nano-resonator, its metallic layer properties also change (the spring constant and the dissipation), which shift down the NEMS' resonance frequency and increase its linewidth (see Sec. II.5.2). We hence measure those shifts and broadening for different applied current oscillation frequencies.
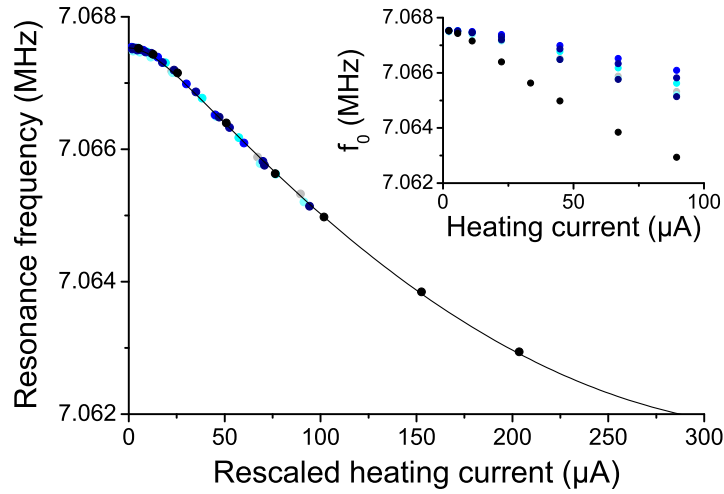
Figure II.16: Shift of the resonance frequency f_0 as a function of the heating current at different frequencies (from D.C. to 20 MHz - from light to dark blue). As I_h increases, f_0 shifts down with a different scaling for each heating frequency (inset). By renormalizing the current for each frequency to the D.C. regime, we can recover a single scaling (main). Those rescaling factors represent the transmission factor in the lines. The black line is a calculation based on the thermal modeling of the goalpost [Collin *et al.* 2012].
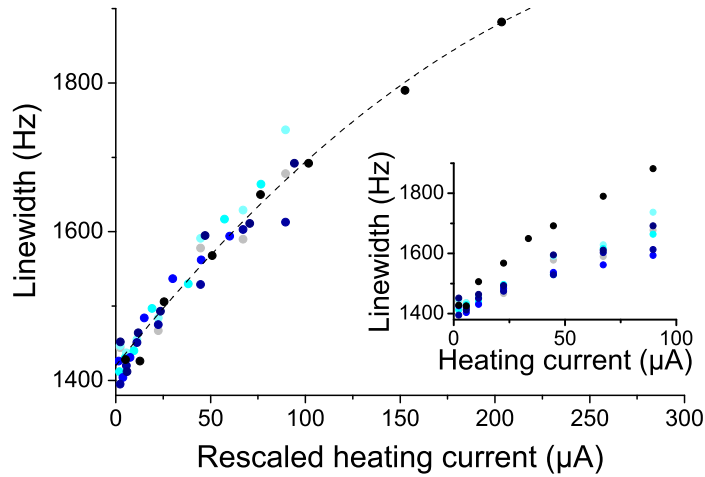
Figure II.17: Broadening of the linewidth Δf as a function of the heating current at different frequencies (from D.C. to 20 MHz). Inset and main follow the same logic as presented in Fig. II.16. The dashed black line is a guide for the eyes reproducing the temperature dependence of Δf. The rescaling factors are identical to the ones in Fig. II.16.

By construction the D.C. regime corresponds to perfect transmission and we thus use it as a reference. Measuring at different powers (different temperatures for the
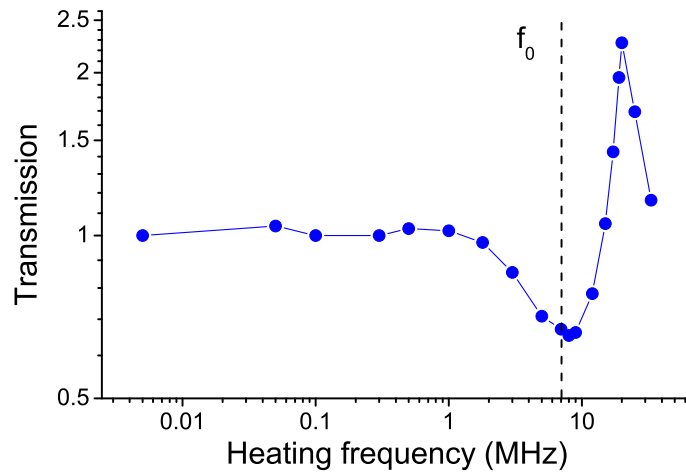
Figure II.18: Transmission of the injection line deduced from the rescaling factors used in Fig. II.16 and Fig. II.17. For our goalpost, we obtain a loss factor of 1.49 on resonance (7 MHz).

nano-structure) both resonance frequency and linewidth, we can rescale the resulting curve onto the DC one for each heating frequency ω_h (Fig. II.16 and Fig. II.17). The scaling factors involved for this correction directly correspond to the loss factor at that frequency (Fig. II.18).

By doing so, one should be careful about not applying the heating current at ω_h too close to a frequency where mechanical dynamics could be excited, like another mode or even the same one used for the calibration protocol. For the first flexure, about a few hundred linewidths away from the resonance frequency are required, depending on the heating current amplitude and on the NEMS non-linear coefficient γ. Indeed, as far as the first mode is concerned, exciting at few linewidths from the resonance frequency basically means driving the NEMS at the tail of the Lorentzian line in Fig. II.8. But if the drive is large enough, this small tail might become comparable to the maximum amplitude of the Lorentzian response at the driving current I_i (Fig. II.19). If the non-linear coefficient of the NEMS is large (even though the NEMS is driven in the linear regime) then the NEMS excitation at both drive and heating current frequencies couple, which will produce an extra shift in the resonance frequency of the NEMS. This "self-coupling" (coupling together two different exciting frequencies through the same mechanical mode) is explained in more detail in Chap. III. The main idea here being that if the heating current frequency ω_h is too close to the resonance frequency ω_0, then the shift in frequency might not come from the Joule effect but from the self-coupling which would lead to wrong extracted calibration factors.

Unfortunately, the doubly-clamped beams' non-linear coefficients are so large that we do see self-coupling up to a thousand linewidths from the resonance fre-
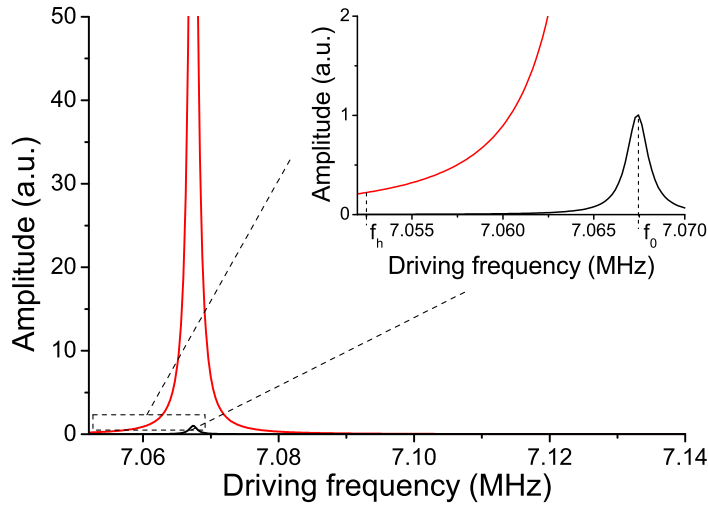
Figure II.19: Representation of the self-coupling issue in the calibration procedure. There is about a factor of hundred between the amplitude of the driving and the heating currents in the calibration scheme. The black curve represents the displacement induced by the driving force, while the red curve is the hypothetical displacement due to the heating current relative to the former one (main). In practice, we heat only at a fixed frequency f_h far from the resonance frequency f_0. But for such a large I_h the resulting displacement of the NEMS can be comparable to the one due to the initial driving force, even at ten linewidths away from f_0 (inset). If the non-linear terms in the dynamics equation are large enough, those two amplitudes might couple, which will shift the measured resonance frequency f_0 (Chap. III).

quency. One way to bypass this issue is to use the magnetic field. While the NEMS amplitude (and thus the self-coupling) depends on the magnetic field due to the magnetomotive scheme [Eq. (II.10) and Eq. (II.1)], the Joule effect does not. Measuring the calibration factor for various fields B and extrapolating the resonance frequency shift at $B = 0$, we are left with the component solely due to the Joule effect, extracting then the right loss factors. In the example presented here (the goalpost structure), the intrinsic non-linearity is small enough not to observe any self-coupling effect on the frequency shift, which enables to measure the loss factor of the lines very close to the resonance frequency and hence very close to the working point.

II.4.3 The capacitive line

The line used to control the gate voltage should also be calibrated. Around the D.C. regime the calibration factor will obviously be 1, but when it comes to excite the NEMS, to mix frequencies or to drive the NEMS with a parametric scheme, then it is essential to know what voltage the NEMS really sees from the gate at a given frequency ω. The general technique is the same as presented above, but since the gate is capacitively coupled to the NEMS, the heating current of the Joule effect will now have the form $I_g = -V_g C_0 \omega \sin(\omega t)$. Similarly to the injection line, not all frequencies are usable: one should avoid being too close to $\omega = 0$ (because of mechanical mixing, see Chap. V) or to a parametrically excited resonance (at $\frac{2\omega_n}{p}$ for mode n, p being an integer).

The analysis for the gate is slightly more complex since, as seen in Eq. (II.15), applying a voltage V_g intrinsically affects the mechanical properties of the NEMS. While we track the resonance frequency as a function of the heating current (thus the voltage V_g), an additional frequency shift arises from the non-linear capacitance:

$$\omega_{0,g} = \omega_0 \sqrt{1 - \frac{1}{2\,k} \frac{\partial^2 C_g(0)}{\partial x^2} V_g^2} \approx \omega_0 - \left(\frac{\omega_0}{4\,k} \frac{\partial^2 C_g(0)}{\partial x^2} \right) V_g^2. \tag{II.22}$$
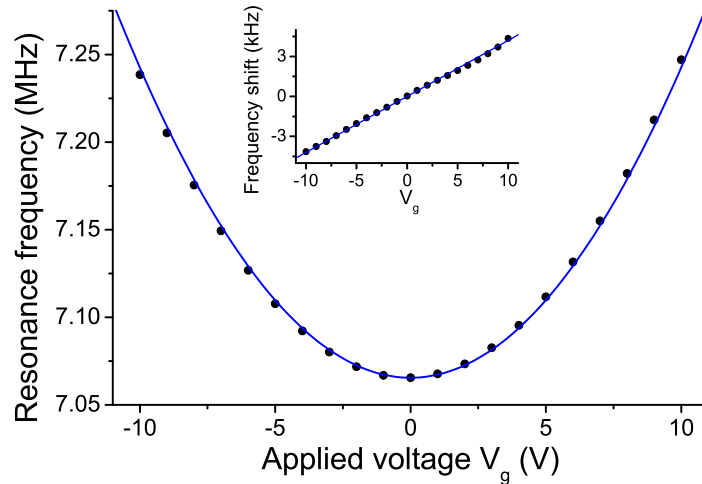
Figure II.20: Main: quadratic shift of the resonance frequency f_0 as a function of applied D.C. gate voltage V_g. We fit $f_{0,g} = f_0 + 1770\,V_g^2$. Inset: substracting the fit to the data, a linear component emerges. Since no linear shift is expected from the model, this component is interpreted as a residual offset voltage on the gate. We finally obtain $f_{0,g} = f_0 + 1770\,(V_g + 0.12)^2$. This residual voltage of 120 mV changes with devices and cryo-cycles, thus this calibration has to be done carefully.

We see in Fig. II.20 the expected quadratic shift of the resonance frequency with a D.C. applied gate voltage, and thus we obtain the second derivative capacitance term $\dfrac{\partial^2 C_g(0)}{\partial x^2}$. If we now subtract this non-Joule effect from the calibration data,

we can recover the capacitance ($C_g = 0.3$ pF at low frequency) and the loss factor in Fig. II.21 as for the injection line. Performing the same technique as described in Sec. II.4, we can then obtain the capacitive line transmission factor (Fig. II.22).
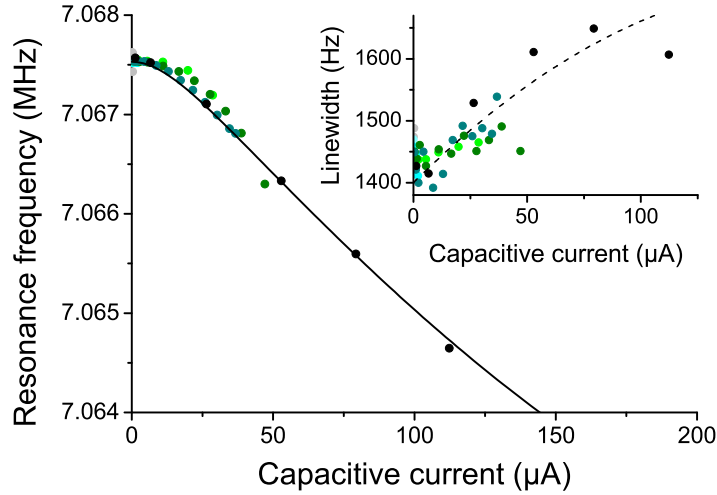
Figure II.21: Main: rescaling of the resonance frequency shift due to the heating current induced by the capacitance at frequencies from 50 kHz to 20 MHz (from light to dark green). Inset: rescaling of the linewidth's increase with respect to the frequency of the heating current from the capacitive coupling with the gate. As for the injection line, from the rescaling factors we can deduce the transmission of the capacitive line.
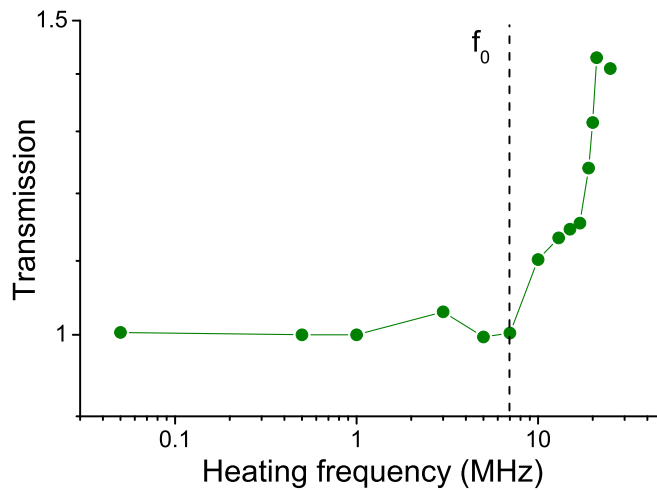
Figure II.22: Transmission of the capacitive line, extracted from the rescaling of the heating current in Fig. II.18. For our goalpost device, the transmission at resonance is about 1.

II.4.4 The detection line

With both the injection and the capacitive lines calibrated, we now need to know the losses in the detection line.
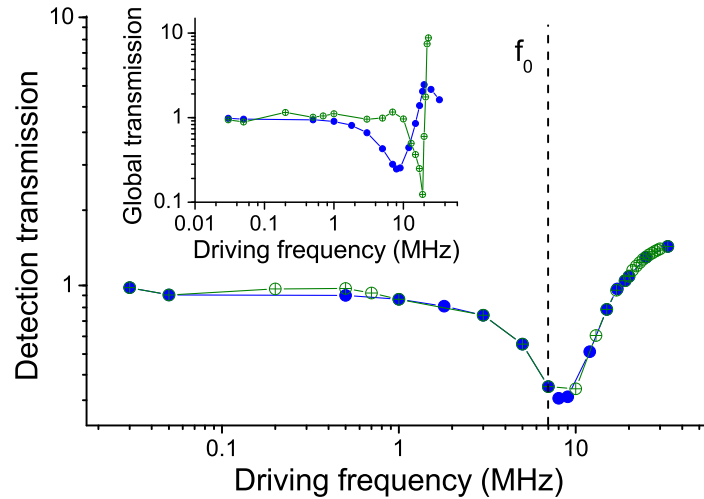
Figure II.23: Inset: transmission through the combination of the injection and detection lines (blue) and the capacitive and detection lines (green). Main: transmission through the detection line deduced from the global transmission of the injection (blue) and capacitive (green) lines. The loss factor in the detection line for our goalpost is here 2.39 at resonance.

One way of deducing the detection losses is to use the calibration of the injection/capacitive lines together with the global transmission from the voltage generator to the lock-in amplifier detector. The NEMS has a resistance r_0 and Ohm's law leads to a voltage (at non resonant frequencies) which can be measured as a function of the applied current (on the injection or capacitive lines). We calculate the deviation of the measured output voltage from an ideal circuit as a function of the frequency and obtain the overall transmission of the circuit which integrates both injection/capacitive lines and detection line calibrations (inset of Fig. II.23). Knowing the losses of the injection/capacitive lines we deduce those of the detection line alone (Fig. II.23). We can see that measuring the detection line from the injection or the capacitive port results in the same transmission factor, validating the technique.

Now that our set-up is thoroughly calibrated, we can measure and convert in real units the NEMS' properties (displacement in meters, forces in newtons).

II.5   Quantitative characterisations

Depending on the geometry, the size or the materials (with their different amounts of stored stress), the NEMS' properties might change by orders of magnitude. In the following sections, we present the general behaviour of our NEMS as we drive different modes, as a function of temperature and increasing the driving force from the linear up to the anelastic regime. Making use of the calibration techniques described in the previous section (Sec. II.4), we reach a quantitative characterisation of our devices. A typical Si goalpost device is shown in Fig. II.1a, while SiN doubly-clamped beams are presented in Fig. II.24.
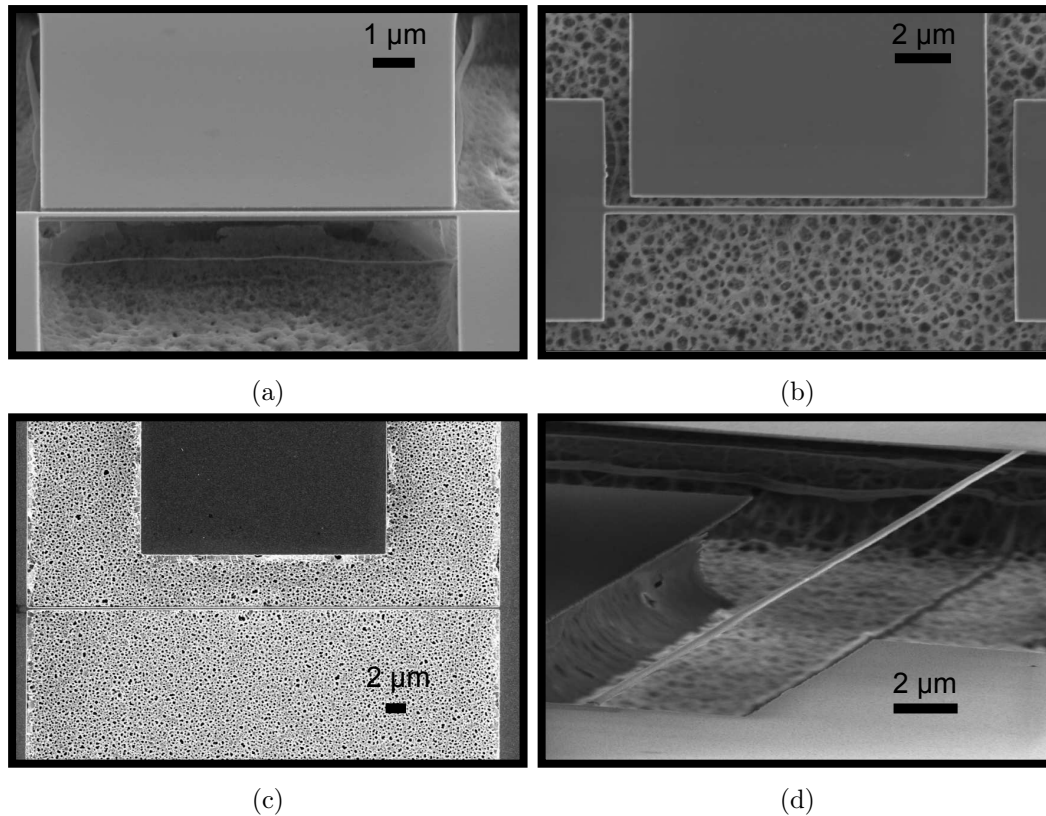
Figure II.24: SEM pictures of different NEMS we characterised, in addition to the goalpost and the 15 μm long low stress beam already presented (with the fabrication technique presented in Sec. II.2). *a*: Slightly tilted top view of a 10 μm long reduced high stress structure (about 600 MPa [Defoort *et al.* 2013b]). *b*: Top view of a 15 μm long high stress (850 MPa) SiN doubly-clamped beam. *c*: Top view of a 50 μm long SiN nano-string. *d*: Side view of a 100 μm long SiN nano-string, with an angle from top view of 89° (note that for this last one, the scale only defines the horizontal axis).

II.5.1   Linear response of NEMS

We measured the resonance frequencies and the dissipation in the linear regime (at small driving forces) for different flexural modes n for various devices: goalpost Si structures and doubly-clamped SiN beams. The characteristics of a goalpost NEMS are presented in Chap. II, and here we essentially discuss our stressed doubly-clamped beam structures, the data being taken at 4.2 K.

From the Euler-Bernoulli equation we know that the resonance frequency for any mode of an ideal resonator, in the tension (or string) limit follows:

$$\omega_{0,n} = \frac{(n+1)\,\pi}{l}\sqrt{\frac{T}{\rho\,w\,e}}\left(1 + 2\sqrt{\frac{E\,I}{T\,l^2}}\right), \tag{II.23}$$

implementing a first order correction due to bending. However as explained in Sec. II.3.3 our experimental measurement scheme enables to access only even modes. Thus, in Fig. II.25 we present our results for $\omega_{0,0}$, $\omega_{0,2}$ and $\omega_{0,4}$ which scale with the length as described in Eq. (II.23). If we take $\rho = 3$ g.cm^{-3}, we obtain an estimate of the tensile stress $\frac{T}{w\,e} = 850\pm80$ MPa (high stress) and 120 ± 50 MPa (low stress). Note however the deviation from the calculation without correction as we enter in the flexural limit which enables an estimate of the Young modulus $E = 200\pm150$ GPa, compatible with the manufacturer data. In this limit of short beams, the contribution of the undercut could also renormalise our frequencies from Eq. (II.23) due to underetch in the fabrication process [Gavan *et al.* 2009]. Note that a large undercut can also relax part of the stress [Defoort *et al.* 2013b], which could explain the deviation for longer beams (experiencing the biggest undercut).

(a)   (b)
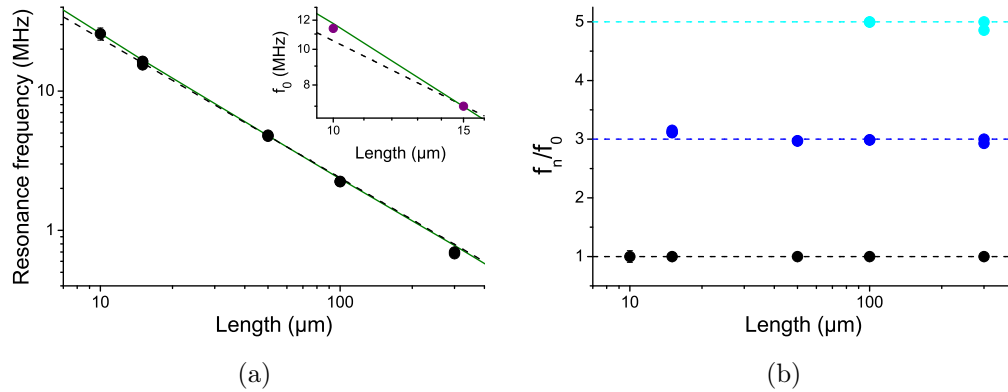
Figure II.25: Resonance frequencies of high (main) and low (inset) stress doubly-clamped beams as a function of the length (*a*) and the mode (*b*). The green line is the full calculation from Eq. (II.23) while the dashed black line does not take into account the bending correction. The size of the symbols is about the reproducibility of the devices, $\pm5\%$. Note that as we measure longer beams, we are able to detect higher modes because of lower frequencies and better quality factors.

On the other hand, the comprehension of the dissipation mechanisms in nanomechanical resonators is still a challenging puzzle. While experimental findings over the years show that the damping (measured linewidth at the resonance of a given mode) decreases as the volume of the devices increases [Carr *et al.* 1999] [Mohanty *et al.* 2002], the intrinsic mechanism is unclear. What has been experimentally demonstrated is that for most nano-devices, the clamping losses are completely negligible [Photiadis & Judge 2004, Judge *et al.* 2007] as well as thermoelastic damping [Lifshitz & Roukes 2000]. In particular, the measured damping is independent of the width of the structure [Verbridge *et al.* 2008, Schmid *et al.* 2011], while it does depend on temperature (see Sec. II.5.2). Some theoretical models attempt to describe the damping, in particular in Refs. [Unterreithmeier *et al.* 2010] [Schmid *et al.* 2011]. In these approaches, the microscopic origin of the energy relaxation is not discussed, but is simply assumed to be proportional to the stored bending energy E_{bend}: we write these bending losses ΔE_{bend}. The actual mechanisms behind this term shall be discussed in Chap. V.

Some approximative alternative versions of this model propose to locate most of the bending energy near the clamping points, where presumably the distortion is the biggest [Schmid *et al.* 2011, Suhel *et al.* 2012]. In the expressions below, we give the simple bulk version of the theory, where the quality factor $Q_n = \frac{\omega_{0,n}}{\Delta \omega_n}$ for mode n writes:

$$Q_n = \frac{E_{tens} + E_{bend}}{\Delta E_{bend}} \approx Q_{bend} \frac{E_{tens}}{E_{bend}}, \qquad (\text{II.24})$$

with E_{tens} the tensile stored energy and Q_{bend} the bending related quality factor. We obtain, again in the string limit with the lowest order bending correction:

$$E_{tens} \propto \frac{T}{l} \frac{(n+1)^2 \pi^2}{2},$$

$$E_{bend} \propto \frac{T}{l} \sqrt{\frac{E\,I}{T\,l^2}} (n+1)^2 \pi^2 + \frac{E\,I}{T\,l^2} \left(4\,(n+1)^2 \pi^2 + \frac{(n+1)^4 \pi^4}{2} \right),$$

$$Q_n \approx Q_{bend} \frac{1}{2 \sqrt{\frac{E\,I}{T\,l^2}} \left[1 + \sqrt{\frac{E\,I}{T\,l^2}} \left(4 + \frac{(n+1)^2 \pi^2}{2} \right) \right]}. \qquad (\text{II.25})$$

It is important to note that we only have here *one fitting parameter* Q_{bend} (which is independent of mode or geometry) to explain any dissipation in the string limit, for a given material. We show in Fig. II.26 our experimental quality factors together with the calculation from Eq. (II.25), and find a good agreement for most Qs, varying both lengths and mode number. Nevertheless, we see for the shortest ones that the dissipation of the second harmonic flexural mode ($n = 2$) seems larger, as if some extra damping alters the predicted one. The flexural dissipation model thus seems to be a good starting point, but is clearly not enough to encompass all experimental results. For instance, while all published data present quality factors that essentially scale with the length of the beams [Carr *et al.* 1999, Unterreithmeier *et al.* 2010],
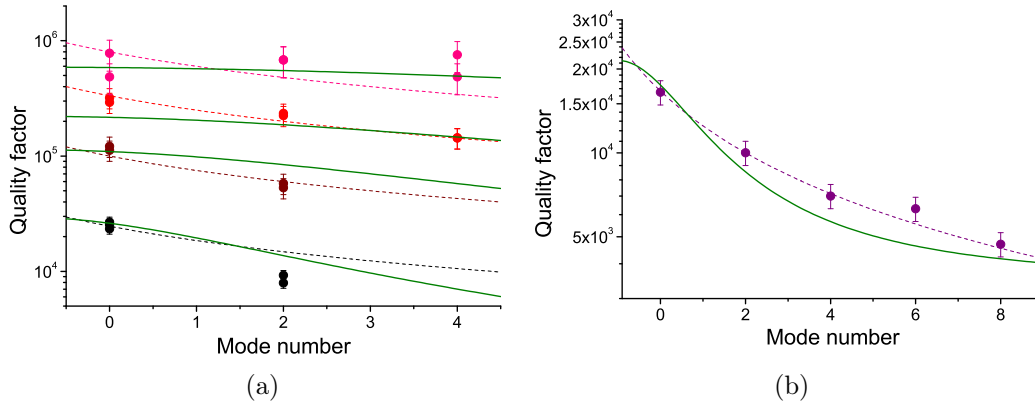
Figure II.26: Quality factors deduced from the measured resonance frequencies and their respective linewidth of high (*a*) and low (*b*) stress doubly-clamped beams as a function of the mode number for different lengths (black and purple: 15 μm, dark red: 50 μm, red: 100 μm, pink: 300 μm). The full green lines correspond to the calculation from Eq. (II.25) with $Q_{bend} = 1900$ for high stress and 3400 for low stress beams. The dashed lines follow the phenomenological approach of Ref. [Suhel *et al.* 2012] where the authors assume that the dissipation mainly comes from the beam distortion at the clamping points, which is nonetheless compatible with our findings. The error bars is the reproducibility of the devices, typically about 10 %.

this feature cannot be reproduced by Eq. (II.24) in the unstressed limit: Q_n is then independent of mode number, and length. The only way to reconcile the modeling with these experimental facts is to postulate a further dependence in-built in the Q_{bend} term characteristic of the microscopic friction mechanisms (see Chap. V).

II.5.2 The temperature dependence

As described in the calibration technique in Sec. II.4, the NEMS properties change with temperature. While the shift in frequency is measured with a better accuracy, the variation of the linewidth has a bigger impact on the NEMS dynamics. Indeed the resonance frequency shifts less than a percent from tens of K to mK while the linewidth might get reduced by orders of magnitude, and as the linewidth gets narrower the displacement amplitude gets bigger at fixed force amplitude [Eq. (II.30)], leading to easier and more accurate measurements.

We present in this section the temperature dependencies of our samples from 1.5 K to 30 K. Theoretical models of mechanical dissipation shall be discussed in Chap. V. The experimental setup is described in Sec. II.3.1. After a small thermalisation time (at worse few minutes) the NEMS thermalises to the desired temperature which is regulated from the resistance bridge. On the other hand the current in the structure is kept small enough to avoid extra heating, as opposed to the technique described in Sec. II.4.

Furthermore, in the calibration procedure the Joule heating generates a non-uniform temperature along the structure while in the present section the whole

(a)   (b)
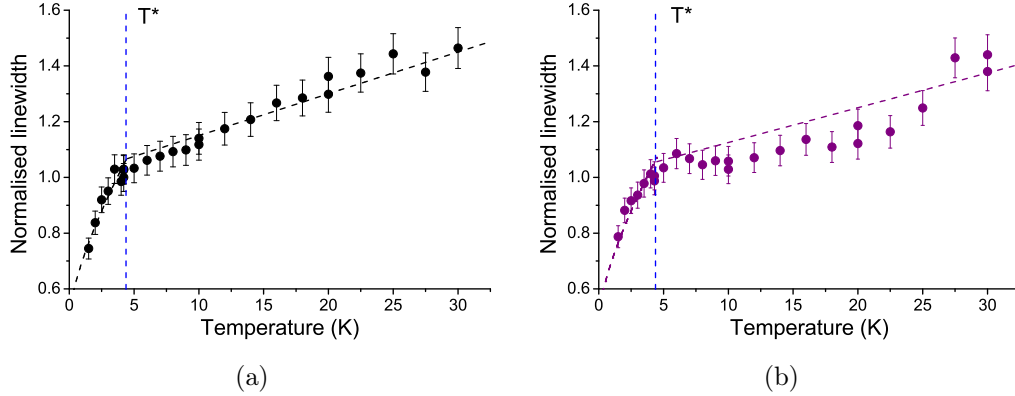
Figure II.27: Increase of the linewidth of the 15 μm long doubly-clamped high stress (*a*, black) and low stress (*b*, purple) beams. Both qualitatively show the same behaviour, with an almost linear dependency above a threshold temperature $T^\star$ (vertical blue dashed line), and a power law dependence below (dashed lines, see Chap. V). Note that the "kink" between the two fitting functions arising at $T^\star$ is only due to the mathematical display.

sample holder is kept at uniform temperature. Note that in the present discussion the metal (aluminium) is kept in the normal state and never becomes superconducting.

(a)   (b)
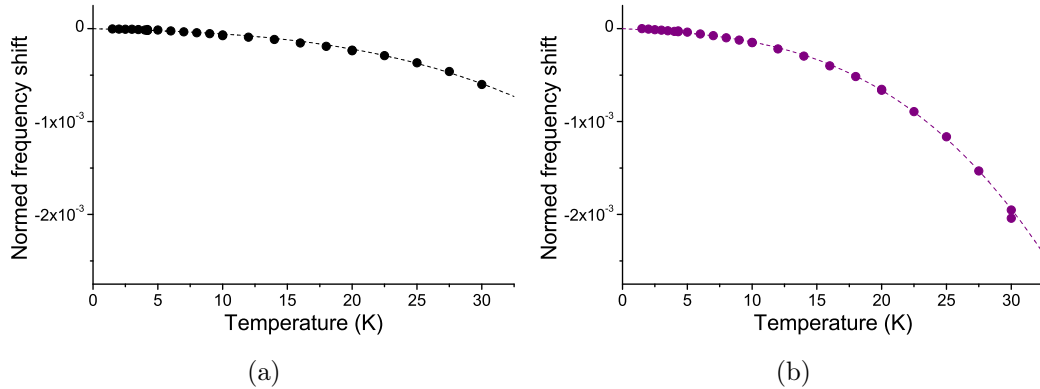
Figure II.28: Shift of the resonance frequency of the 15 μm long doubly-clamped high stress (*a*, black) and low stress (*b*, purple) beams. The dashed lines are guide for the eyes, of the form $a\,T + b\,T^3$.

In Fig. II.27 and Fig. II.28 we show two examples of frequency shifts and dissipation variation (linewidth) with temperature, in low and high stress doubly-clamped beams. As explained in Sec. II.4.1, one should never forget to remove any loading effect in order to measure the real intrinsic frequency and linewidth of the NEMS. As far as dissipation is concerned, the variations in both devices behave in the same way: above a threshold temperature $T^\star$ the dissipation slightly increases almost linearly with temperature (of the order of the percent per kelvin). Below
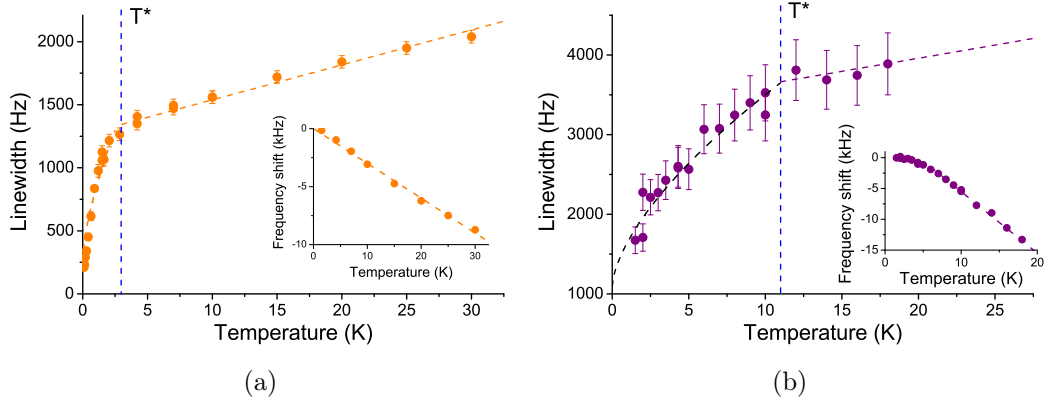
Figure II.29: Linewidth (main) and resonance frequency (inset) variation with respect to the temperature for the goalpost (*a*) and the third mode of the 15 μm low stress doubly-clamped beam (*b*). Again, the same tendencies as on Fig. II.27 and Fig. II.28 are seen.

$T^\star$, the dissipation falls with a power law which requires millikelvin temperatures to be properly defined. For the frequency shifts, essentially all data can be fit to $aT + bT^3$. Depending on the device, the former (linear) or latter (cubic) term can dominate. Comparing our different devices, presumably the linear term arises from the Young's modulus temperature dependence while the cubic one corresponds to the thermal stress stored in the structures (bimetallic strip effect arising from the thermal contraction coefficients mismatch).

In Fig. II.29 we present the temperature dependencies of the goalpost structure and of the third mode of the low stress doubly-clamped beam. Again, we see the same behaviours as for the other devices presented within the same orders of magnitude. Since the geometry, the mode shape and even the mechanical material are varied, we have to conclude that to some extent these features are linked to the only common feature between these devices: the Al metallic layer. The same argument applies to anelastic features (see Sec. II.5.4) and has been demonstrated by changing the overlayer [Collin *et al.* 2010b]. A more comprehensive discussion on the role of the metallic layer shall be given in Chap. V.

II.5.3 The Duffing non-linearity

As explained in Sec. II.3.5, our NEMS devices can essentially be considered as Duffing resonators when driven at large amplitudes. We recall the expression of the displacement:

$$x = \frac{F_L}{2\,m\,\omega_0} \frac{1}{(\omega_0 + \beta\,x^2 - \omega) + i\,\frac{\Delta\omega}{2}}, \tag{II.26}$$

with $\beta = \dfrac{3\,\gamma}{8\,\omega_0}$ and γ the non-linear coefficient. Basically this quadratic correction to Eq. (II.8) bends the initial Lorentzian lineshape into a so-called "Duffing" resonance

with the opening of an hysteresis in frequency for $x > x_c$ defined in Eq. (II.18), see Fig. II.30.
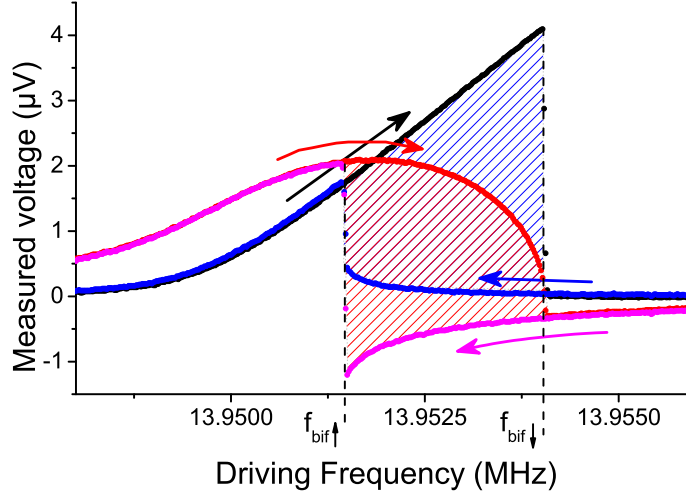
Figure II.30: In-phase (black/blue) and quadrature (red/magenta) components of a Duffing resonance with a positive non-linearity (here of a 15 μm long high stress doubly-clamped beam). The dashed region represents the hysteresis where two physical solutions coexist. At the edge of the hysteresis ($f_{bif\uparrow}$ and $f_{bif\downarrow}$), the system might switch by itself to the other solution (see Chap. IV).

In this region, two of the three solutions of Eq. (II.26) are (meta-)stable (the small and the large oscillation amplitudes) and one is unstable (the intermediate amplitude). The actual chosen amplitude of the system's motion is then determined by the NEMS' frequency sweeping history.

As we get closer to the edges of the hysteresis, the system might bifurcate to the other stable solution, a phenomenon which is described in Chap. IV, and we call $\omega_{bif\downarrow}$ and $\omega_{bif\uparrow}$ the frequencies delimiting those edges. As we increase the drive, the hysteresis gets bigger and thus the resonance frequency shifts. For a large non-linear term, the resonance frequency ω_{res} (frequency at which the mechanical mode reaches its maximal motion amplitude) almost merges with $\omega_{bif\downarrow}$ and shifts as:

$$\omega_{res} = \omega_0 + \beta\, x_{max}^2, \tag{II.27}$$

as shown in Fig. II.31.

The non-linear coefficient γ is of geometrical origin, as already explained in Sec. II.3.5. Non-linear extensions of beam theories can be used to quantify γ [Lifshitz & Cross 2008, Nayfeh & Mook 1995]. The expression reads:

$$\gamma = \frac{1}{2}\frac{E}{l^4\,\rho}\left(\int_l \Psi'^{\,2}(z)\,dz\right)^2. \tag{II.28}$$
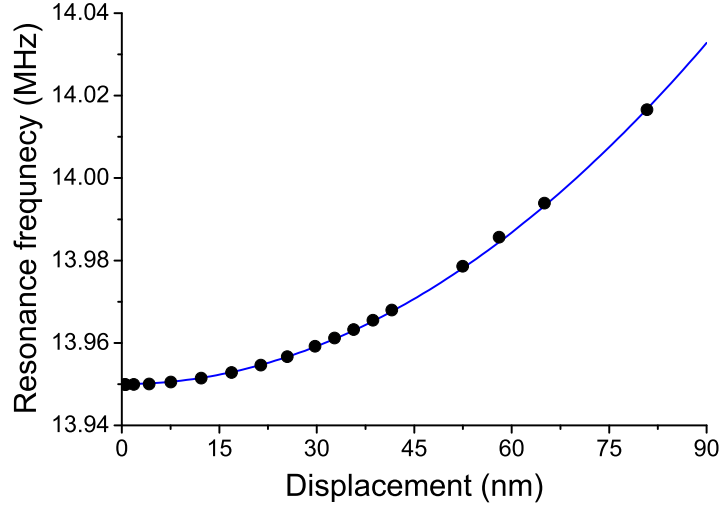
Figure II.31: Shift of the resonance frequency as we increase the excitation, and thus the motion amplitude (same device as Fig. II.30). From a quadratic fit we can extract the Duffing coefficient (here $\beta = 22$ Hz/nm^2). Note that with the lock-in technique, the signal in-phase is maximum at resonance while the out-of-phase one crosses zero.
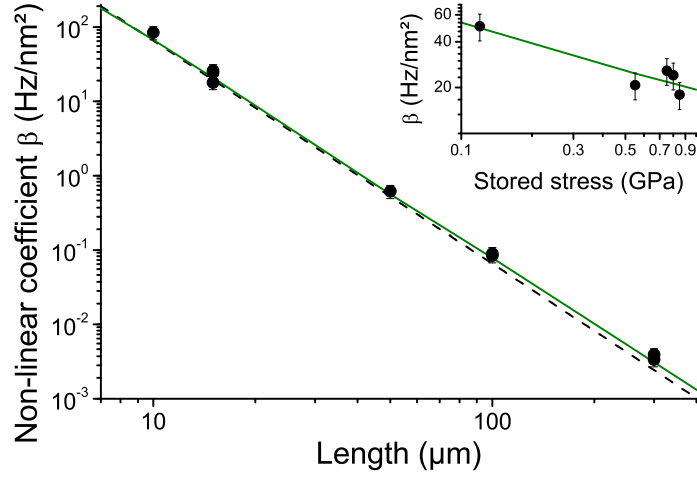
Figure II.32: *Main*: non-linear coefficient of the fundamental mode as a function of the length of the high stress doubly-clamped beams. The black dashed line is a calculation of the non-linear coefficient from Eq. (II.29), which follows the inverse of a cubic power law with respect to the length of the beam, while the green full line takes into account a correction due to a small flexural contribution (as in Fig. II.25). *Inset*: β as a function of the stress stored for the 15 μm long beams. We observe that the data follows the expected square-root power law (green line). Note that all error bars are of the order of 20 %, which is the reproducibility between our devices.

In the high stress limit, this leads to:

$$\beta = \frac{3}{16\,\pi} \frac{E}{l^3 \sqrt{\rho \frac{T}{e\,w}}} \left(\int_l \Psi'^{\,2}\left(z\right) dz \right)^2 . \tag{II.29}$$

In Fig. II.32 we plot our experimental findings together with this expression, as a function of the length and the stress of the beams. Some devices' calibrations were deduced from the one of the 15 μm long structure presented in Fig. II.30. For these NEMS the tedious calibration procedure of Sec. II.4 had not been preformed, but the deduced coefficients are consistent with the measured ones. This procedure could be the cause of the reproducibility error bars in Fig. II.32. The power law dependencies are verified [Defoort *et al.* 2013b], and the quantitative agreement is quite good, in accordance with Ref. [Matheny *et al.* 2013].

However in the case of the goalpost device, its geometry is such that the non-linear coefficient is intrinsically nearly non-existent, making it extremely linear even in the 100 nm motion amplitude range. As described in Eq. (II.15) in Sec. II.3.4, the gate electrode can be used to change the non-linearity of the NEMS. With this coupling, it is possible to tune on demand the non-linear term for a fixed drive amplitude (Fig. II.33). The non-linear behaviour can be augmented by increasing either the displacement (Fig. II.34), or the voltage (Fig. II.35), and we extract the voltage-dependent Duffing coefficient $\beta = -0.0467\,V_g^2$ Hz/nm^2 from these two plots. Note that when x is about the size of the gap between the gate electrode and the resonator, $|\gamma|$ starts to decrease because the Taylor series approach of Sec. II.3.4 loses its validity.
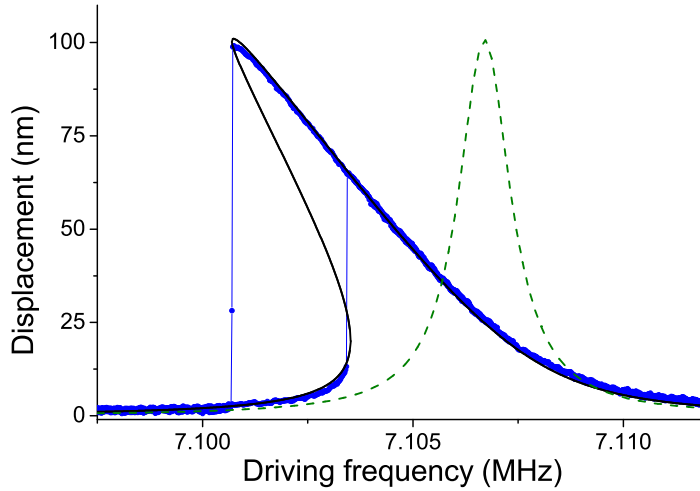
Figure II.33: Non-linearity induced by the gate voltage (here $V_g = 4.7$ V) on the goalpost device. We show here the magnitude of the displacement $V_R = \sqrt{V_X^2 + V_X^2}$. While the hysteresis is large (blue data points and black line fit), the displacement amplitude remains the same as for the linear regime (green dashed line, $V_g = 0$ V). Note that the non-linear line is also shifted by a term $\propto \frac{\partial C}{\partial x} V_g^2$ [see Eq. (II.15)], which has been subtracted for readability.

From the coupling nature of the gate, the non-linearity created for out-of-plane motion is negative [Kozinsky *et al.* 2006], and as seen in Fig. II.30 the intrinsic non-linearity of beams is positive. By fine tuning the voltage on the gate, one could think
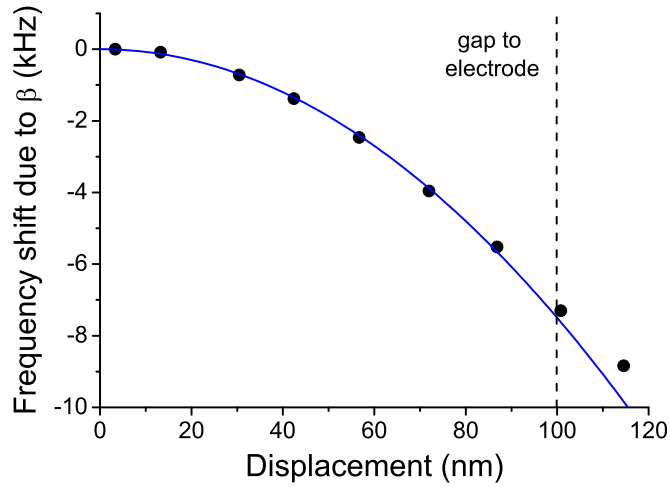
Figure II.34: Frequency shift due to the induced non-linearity (here $V_g = 4$ V) as a function of the displacement amplitude. The shift from the spring constant alteration is already taken into account. We see a deviation from the quadratic law for displacements above 100 nm, where the Taylor expansion breaks down [Eq. (II.22)].
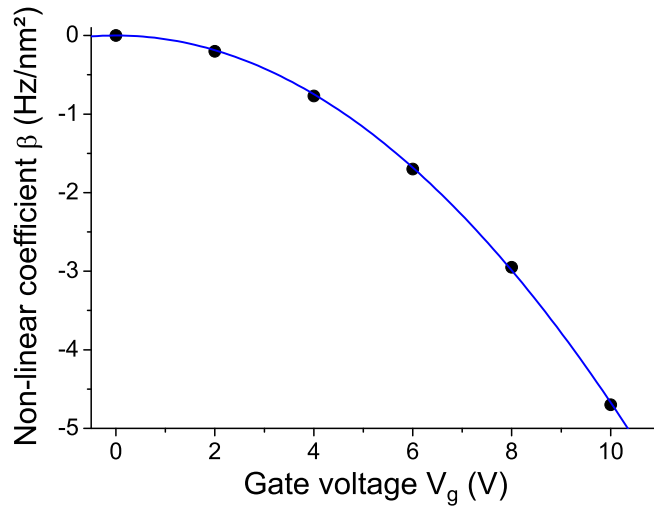
Figure II.35: Extracting the non-linear coefficient at different gate voltages as presented in Fig. II.34, we can recover the dependence of γ with respect to V_g.

of suppressing most of the intrinsic β. Unfortunately, the distance from the gate to the NEMS and the applied voltages have to be such that we could not achieve it in our experiments. On the other hand, the non-linear coefficient β (intrinsic or voltage-created) can be used to implement interesting non-linear schemes, as presented in Chaps. III and IV.

II.5.4   From the linear response to the anelastic regime

In the linear regime described by Eq. (II.8), an applied force on the NEMS results in a displacement which reaches its maximum when the oscillating force frequency is at the resonance frequency ω_0 of the NEMS' studied mode. Plotting the displacement x as a function of the force F_L on the mode (Fig. II.36), we can extract the associated spring constant k through:

$$x = \frac{F_L\,Q}{k}, \tag{II.30}$$

which is obtained by solving Eq. (II.10) at $\omega = \omega_0$.
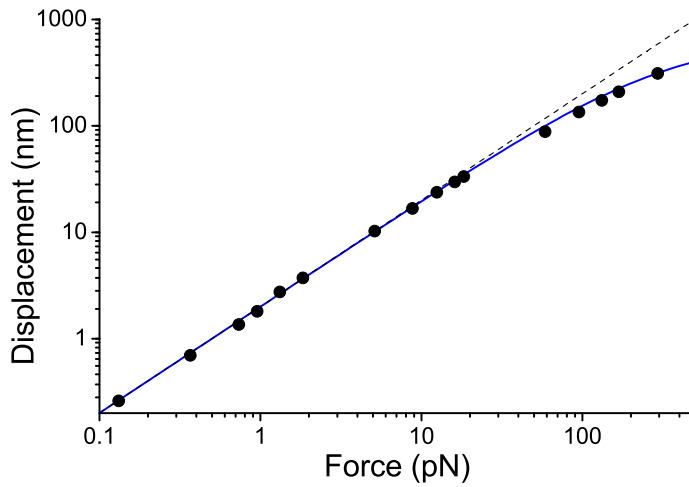
Figure II.36: Displacement amplitude as a function of the driving force for the goal-post device. With the dashed line we fit a linear response from which we extract a spring constant $k = 2.34$ N.m^{-1}. At large displacements, we need to incorporate a small deviation to this linear behaviour, as presented with the full blue line.

With x and F_L properly calibrated (see Sec. II.4) and $Q = \frac{\omega_0}{\Delta\omega}$, we obtain the mode's spring constant k and then deduce the associated mass m from its resonance frequency (Sec. II.5.1). Extracted values are compatible with calculations within $\pm 5\,\%$ approximately. Note that for a Duffing resonance (Sec. II.5.3), Eq. (II.30) is still valid if the amplitude x is measured on the upper branch of the bistable solution, sweeping the frequency in the direction defined by the sign of β (i.e. upward for $\beta > 0$).

However for large applied forces, we see in Fig. II.36 a deviation from the linear expression Eq. (II.30). One can phenomenologically fit the deviation replacing Eq. (II.30) by:

$$x = \frac{F_L\,\omega_0}{k\,\Delta\omega\,(1 + \alpha\,x)} \quad \text{for} \quad x > x_{thr}, \tag{II.31}$$

$$x = \frac{F_L\,\omega_0}{k\,\Delta\omega} \qquad\qquad \text{for} \quad x < x_{thr}. \tag{II.32}$$

These expressions are interpreted as a signature of the anelasticity of the metallic layer [Collin *et al.* 2010b, Collin *et al.* 2011a]. Above an amplitude threshold x_{thr}, the damping starts to increase roughly linearly with the motion amplitude. When x_{thr} is particularly small the linear linewidth dependence on x seems to start from $x = 0$, while sometimes a linear frequency shift can be resolved as well on top of the Duffing dependence [Collin *et al.* 2008]. The actual microscopic origin behind the phenomenon is still unclear, but the phenomenological approach is sufficient to characterise thoroughly the dynamics of all our devices from the linear up to the strongly non-linear range.

II.6 Conclusion

In this chapter we presented the basics of the NEMS characterisation, which is the first step before actually using them to investigate any physical phenomena. After describing the fabrication process involved to make our devices, we presented the experiment in which the NEMS are measured. We use an electric set-up, the devices being kept under vacuum in a cryogenic environment. Using the magneto-motive scheme we excite and detect our NEMS motion. Their mechanical resonances follow a Lorentzian law at small excitations, and they are fully characterised in the linear regime by their resonance frequency, their linewidth and their maximum displacement amplitude. Using the capacitive coupling created by a gate electrode, we can change those properties: tune the resonance frequency, or modify the non-linear Duffing behaviour.

We then explained in detail the calibration procedure used to obtain the NEMS resonance in real units, using the shift of the resonance frequency and the linewidth broadening as an in-situ measurement of the actual current seen by the NEMS. Our high impedance set-up is unique in the literature, and enables high precision measurements of mechanical dissipation [Collin *et al.* 2012]. Through this technique, we detected the actual displacement of our resonators, for different modes and different nano-beams' properties. We measured the scaling laws of the resonance frequencies, the quality factor and non-linear coefficients as a function of the length of our nano-wires and for different in-built stresses. We also measured the evolution of both ω_0 and $\Delta\omega$ as a function of the temperature of the devices. To finish with, we presented the implications of the Duffing non-linearity in the measurement of the resonance line, and how the gate electrode non-linear tuning affects the measurements.

This non-linear parameter is the essence of new complex physics and will be at the core of the Chaps. III and IV.

II.7   Perspectives

The investigation of new physical phenomena using NEMS resonators increased since the last decade, and their characterisation with respect to the geometries or the materials gets continuously updated as projects evolve. Thus, developing new schemes of actuation/detection and being sensitive to different NEMS properties to improve the presented characterisation might be more important than getting more samples with different sizes or stresses. Indeed, only symmetric out-of-plane flexural modes have been addressed in this thesis, and new capacitive/magnetomotive set-ups could be extremely valuable: with asymmetric electrode patterns, or two-axes coils enabling to drive/detect odd and in-plane modes. Compared to other schemes aiming at the same possibilities (acoustic or dielectric drives), this would enable to build on the capabilities of the combined electro-magnetomotive layout.

As far as calibration is concerned, the presented magnetomotive scheme suffers from its own advantage. Since the NEMS sees a high impedance environment its loading is hence relatively small, which is essential when it comes to measure the very small linewidth of the long doubly-clamped beams. On the other hand the end impedance mismatch to the 50 Ω lines induces the necessity of a thorough calibration in order to measure the NEMS parameters in proper units. To bypass this procedure, one could think of implementing a cryogenic voltage follower (which has a high impedance input and a low impedance output) working in the MHz-GHz range. However, such a voltage follower is not a trivial electronics component and essentially a devoted HEMT first-stage transistor would need to be developed specifically for this purpose.

II.8   Résumé

Les résonateurs nano-mécaniques offrent aujourd'hui de nouvelles possibilités en physique de la matière condensée. Cependant, avant de les utiliser comme sondes ou comme système modèle, il est important de maitriser quelques étapes préliminaires: la fabrication, la mise en place du dispositif expérimental, la calibration et la caractérisation des différents NEMS utilisés. Dans le cadre de cette thèse, on distingue deux types de résonateurs. D'une part, grâce à Jean-Savin Heron, nous avons utiliser des NEMS en forme de portique, en Silicium. D'autre part, grâce à Kunal Lulla et Thierry Crozes, nous avons obtenu une large gamme de nano-fils en Nitrure de Silicium, de différentes tailles et avec un matériau plus ou moins contraint. Tous nos échantillons sont ensuite couvert d'Aluminium (Fig. II.2) afin d'obtenir un contact électrique avec notre NEMS.

L'échantillon est alors collé au sein d'une cellule expérimentale pompée à 10^{-4} mbar que nous plongeons dans un cryostat à 4.2 K, relié à l'environnement 300 K par un dispositif électrique haute impédance (Fig. II.3). A l'aide du champ magnétique produit par une bobine entourant la cellule, nous pouvons exciter nos NEMS grâce à la force de Laplace et détecter sa résonance en utilisant la loi de Lenz. L'oscillation du NEMS, décrite en régime linéaire par une résonance Lorentzienne, est caractérisée par une fréquence de résonance ω_0, une amplitude de résonance x, et une largeur de raie à mi-hauteur $\Delta\omega$ (Fig. II.8). De part la nature de ce dispositif expérimental, nous n'étudierons uniquement que les modes de résonance dont la forme est décrite par un nombre pair de nœud. Afin d'en avoir un contrôle plus approfondi, nos NEMS font face à une électrode de grille. Grâce à ce dispositif supplémentaire, nous pouvons exciter nos nano-résonateurs, contrôler leur fréquence de résonance et leur non-linéarité. Sujet au cœur de cette thèse, les phénomènes non-linéaires sont à l'origine d'une physique riche qui sera plus détaillée dans les chapitres suivants. Issue de la tension engendrée par le déplacement du nano-résonateur, la non-linéarité de Duffing a pour principale effet de transformer la résonance Lorentzienne en une résonance bistable.

Afin que toutes nos mesures soient effectuées en vraies unités (mètres, Newton) et afin de comparer quantitativement nos résultats théoriques et expérimentaux, le dispositif expérimental doit être entièrement calibré [Collin *et al.* 2012]. D'une part, dû à la nature de l'excitation et de la détection du NEMS, le champ magnétique appliqué par la bobine affecte la largeur de raie $\Delta\omega$ mesurée, qu'il faut corriger pour obtenir la largeur réelle (Fig. II.14). D'autre part, l'ensemble du dispositif électrique étant désadapté du générateur au NEMS, le courant haute fréquence perçu par ce dernier diffère de celui imposé à la sortie du générateur. Afin d'effectuer une calibration *in situ* de nos nano-résonateurs, nous avons utilisé l'effet Joule sur le NEMS. En plus d'un premier courant permettant de mesurer l'oscillation du NEMS, un second est appliqué hors-résonance pour chauffer ce dernier. Ce chauffage *local* altère les propriétés mécaniques du matériau, modifiant la fréquence de résonance (Fig. II.16) et la largeur de raie (Fig. II.17). En contrôlant la fréquence à laquelle

le second courant est appliqué et en observant les variations des paramètres du NEMS, on extrait la transmission des lignes à cette fréquence, ce qui nous permet de connaitre la réelle puissance fournie à la structure, calibrant ainsi nos lignes d'injection (Fig. II.18). Il est ensuite possible de remonter à la transmission de notre ligne de détection afin de mesurer en mètre le déplacement du nano-résonateur (Fig. II.23).

Suivant la nature du matériau, de la géométrie et de la taille de la structure, les propriétés des NEMS peuvent varier de plusieurs ordres de grandeur. Nous rassemblons dans cette section les résultats obtenus sur plus d'une dizaine d'échantillons avec des tailles allant de 10 μm à 300 μm et des contraintes internes (en tension) de 100 MPa à 850 MPa (Fig. II.24) [Defoort *et al.* 2013b]. Prédit par les équations d'Euler-Bernoulli, nous avons vérifié la dépendance de la fréquence de résonance en fonction de la taille et de la tension de nos poutres doublement encastrées (Fig. II.25). La dissipation de ces échantillons, sujet beaucoup plus difficile à étudier d'un point de vue théorique, a pu être comparé aux derniers modèles proposé avec un accord qualitatif (Fig. II.26). Contrôlant la température du NEMS à l'aide d'un thermomètre résistif (Allen-Bradley), nous avons étudié l'évolution de la fréquence de résonance ω_0 et de la dissipation $\Delta\omega$ de nos NEMS (Fig. II.28). Nous avons observé en particulier un changement de régime de la dissipation à basse température, que l'on suspecte provenir des systèmes à deux niveaux présent dans nos structures. Mesurant l'amplitude de résonance de nos NEMS, nous avons pu étudier, en fonction de la taille et de la tension, la non-linéarité β de nos résonateurs de Duffing, correspondant quantitativement aux prédictions de la mécanique du solide (Fig. II.32). Nous exposons enfin le déplacement de nos NEMS en réponse à une force excitatrice, du régime linéaire au régime anélastique où la déformation des matériaux altère la dissipation mécanique (Fig. II.36).

From coupling modes to cancelling non-linearities

Contents

III.1   Introduction

Non-linearities are at the heart of rich and complex phenomena. For instance, it enables to couple two degrees of freedom (modes of the same device, or even of different ones) so that one affects the other. In the framework of quantum mechanics, non-linearities provide quantum information read-out schemes, and it is now usual to couple a quantum bit (a spin $\frac{1}{2}$ quantum state) to a micro-wave cavity in order to measure its state [Regal *et al.* 2008, Palomaki *et al.* 2013]. As far as nanomechanics is concerned, recent works show that it is possible to cool down a NEMS in its ground state and to control its quantum dynamics [O'Connell *et al.* 2010, Chan *et al.* 2011]. Moreover, it has been suggested that one could use the non-linear coupling between different modes of the same resonator in order to measure the quantum state of the fundamental one [Mahboob *et al.* 2012]. This interest in mode-coupling has been continuously increasing since the revealing of such features in NEMS [Westra *et al.* 2010]. Recent works even address the issue of coupling different mechanical devices, with emerging features like frequency synchronisation [Cross *et al.* 2004, Matheny *et al.* 2014]. In this chapter, while we do not focus on quantum information or multiple systems, we present how mode-coupling on its own can induce very particular properties within a single resonator's dynamics.

In a first part, we describe the mode-coupling scheme in the case of NEMS, with a state-of-the-art section and our measurements of this effect. In this technique, the structure is driven at two frequencies corresponding to two modes of the resonator. Then we describe a new scheme which follows on from the mode-coupling: the "self-coupling", or how to couple one mode with itself. In this case the frequency of the two drives are only slightly detuned and excite one single mode. We present experimental results and calculations which describe the NEMS behaviour. The last section of this chapter is confidential.

III.2 Non-linear coupling between modes

III.2.1 Coupling two modes

As described in Sec. II.3.3, the resonators that we characterised can be driven at different modes. These modes, which are independent in the linear response limit get coupled all together as soon as non-linearities come into play. Through the canonical Duffing non-linearity (see Sec. II.5.3), it is then possible to couple them within the same mechanical resonator in a dispersive way [Westra *et al.* 2010, Dunn *et al.* 2010]. The general idea can be described and explained easily for doubly-clamped beams with the tensile non-linear effect generating the Duffing behaviour. Driving an ideal device at its resonance frequency will make it vibrate at a given oscillation amplitude. Expanding the calculation for large enough amplitudes, this oscillation will generate a stress in the material, and as the drive amplitude increases the resonance line experiences a shift in frequency (through the tensioning), modifying the Lorentzian shape to a Duffing one (as explained in Sec. II.5.3). This property exists for any mode, each one having a different non-linear coefficient γ_n, n being the mode number.

If we now drive two modes simultaneously at large enough amplitude, a similar behaviour is observed. Since the stress generated by the oscillation amplitude of one mode affects the material properties of the whole beam, it thus affects the second driven mode, and vice versa (Fig. III.1).
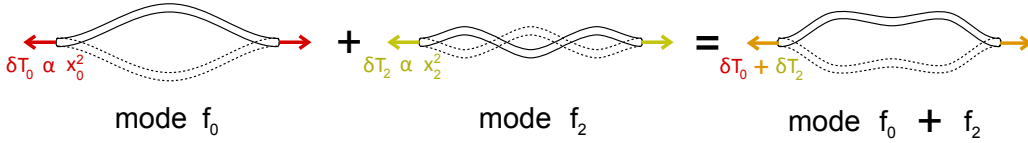
Figure III.1: Schematic of the shape of a mechanical motion induced by two drives, each one exciting a different flexural mode (here the fundamental at f_0 with motion amplitude x_0 and the second harmonic at f_2 with x_2). In a time-resolved picture, the shape of the resonator's motion is imprinted by both excitations, which are coupled through the tension terms δT_0 ($\propto x_0^2$) and δT_2 ($\propto x_2^2$).

This mode-coupling behaviour can be derived theoretically from beam theory [Lulla *et al.* 2012] and the solution resulting from the calculation describes the dispersive coupling between the two modes as:

$$\omega_n = \omega_{0,n} + \beta_n x_n^2 + \beta_{n,m} x_m^2, \qquad \text{(III.1)}$$

with ω_n the resonance frequency of mode n entering in its lineshape Lorentzian expression, and containing a Duffing $\beta_n x_n^2$ component as well (see Sec. II.5.3, where the n index was dropped). The coupling with the mode m is produced through the quadratic term $\beta_{n,m} x_m^2$ (x_m being the motion amplitude of mode m). The

non-linear coefficient $\beta_{n,m}$ reads:

$$\beta_{n,m} = \frac{1}{4\,\pi} \frac{E}{l^3 \sqrt{\rho\frac{T}{e\,w}}}$$

$$\times \left(\frac{\int_l \Psi_n'^2(z)\,dz \int_l \Psi_m'^2(z)\,dz}{2} + \left(\int_l \Psi_n'(z)\,\Psi_m'(z)\,dz \right)^2 \right). \quad \text{(III.2)}$$

Note the similarities with Eq. (II.29). Also, it is important to stress the fact that while the non-linear term $\gamma\,x^3$ in the dynamics equation is the essence of this coupling, none of the two modes needs to be in the non-linear regime. The strong implication of Eq. (III.1) is that one mode can be used to detect another one through its resonance position (Fig. III.2): we can *transduce* a displacement amplitude (of mode m) into a frequency shift (of mode n) [Matheny *et al.* 2013].
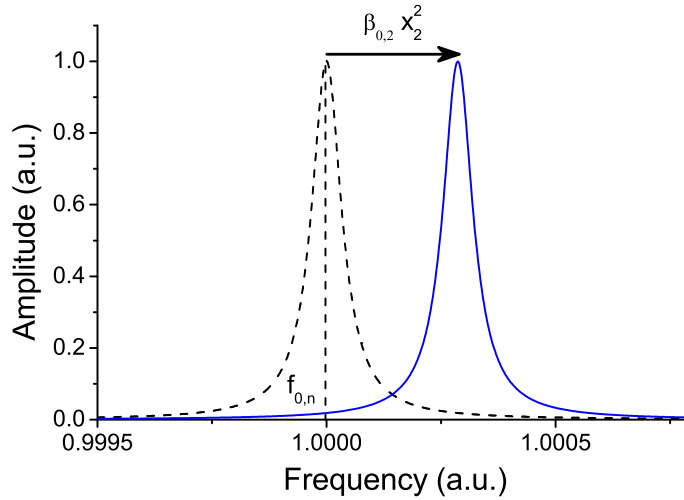
Figure III.2: Schematic representation of the mode coupling effect (plot of the amplitude R in normalised units). As we drive another mode (here the second harmonic), the first one (here the fundamental flexure) is altered and its resonance frequency shifts quadratically with the amplitude of the former one while remaining perfectly linear. We can thus detect a high-order mode by looking at the frequency shifts of another of lower frequency, and vice-versa.

This scheme is particularly efficient in the case of large enough non-linear coefficients, since it enables more accurate measurements than with a direct voltage detection technique. Indeed, as far as the electric set-up is concerned, the standard detection is limited by the voltage noise of the experiment while the mode-coupling scheme is only limited by the (small) phase noise in the circuit: for very high frequency resonances, the voltage to be detected resulting from the motion may be vanishingly small, while the frequency shift can be perfectly measurable.

Using this technique on the 15 μm low stress doubly-clamped beam (on which we found the larger Duffing non-linear coefficient, see Fig. II.32), we could measure many higher modes while a direct magnetomotive read-out only detected noise (see Fig. III.3).
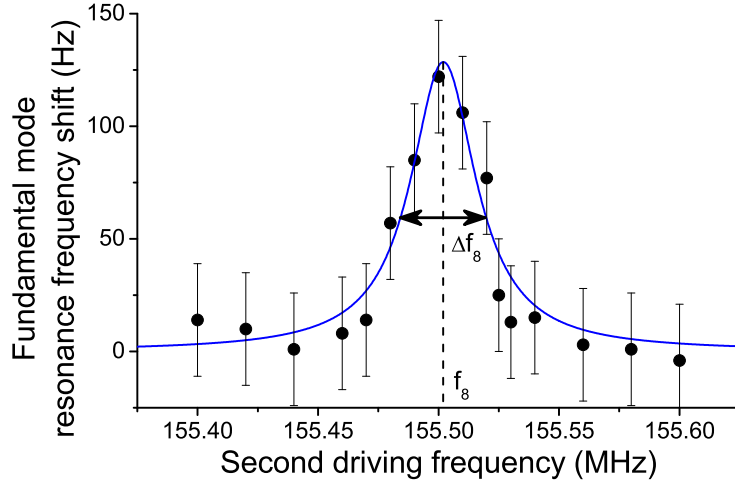
Figure III.3: mode-coupling between the fundamental mode an the 8th harmonic. As explained in Fig. III.2, a shift in the resonance frequency is generated from this coupling, and by tracking f_0 we can recover both f_8 and Δf_8. Note that in a direct measurement technique we could only measure noise when sweeping in the same frequency region.

From the mode-coupling scheme, we could then extract resonance frequency and linewidth of each of these high order modes. In practice, the set-up is the same as the one used for the calibration technique, or the bifurcation experiment (Fig. II.13). With an adder, we send the two oscillating current components (one around ω_n, the other one around ω_m) down the cryostat to the NEMS, generating thus the two Laplace forces (Sec. II.3), one on each mode. Every single data point in Fig. III.3 involved the measurement of a full first mode resonance line to extract the frequency shift (for each high-frequency drive chosen, for a fixed excitation amplitude), hence the detection of the coupled mode takes few minutes. However, one could easily think of an algorithm tracking the resonance frequency of mode n as we sweep mode m, which measurement is then about as long as a standard sweep of mode m. In order to optimise this technique, the tracking of mode n should be performed where the variation of the amplitude is the steepest with respect to frequency: a tiny frequency shift is then easily detected [Venstra *et al.* 2012]. For a homodyne measurement set-up, this occurs at the resonance frequency but tracking the out-of-phase signal, as presented in Fig. III.4.
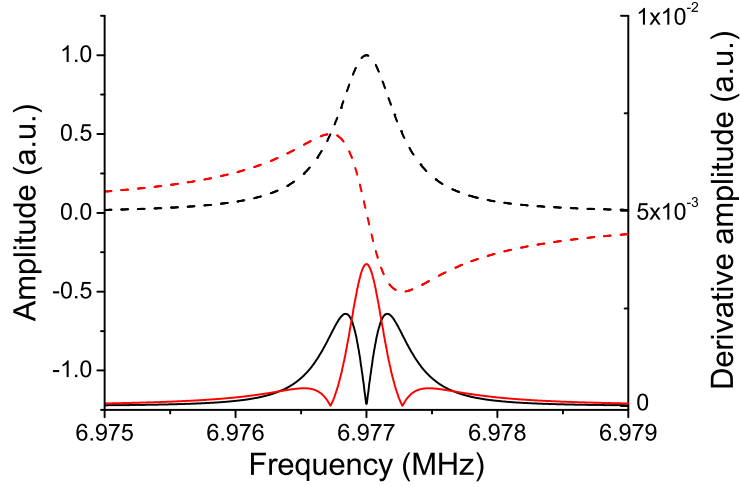
Figure III.4: Representation of Eq. (II.11) and their first derivative for the fundamental harmonic of the 15 μm long doubly-clamped beam (respectively dashed lines and full lines, with in-phase in black and quadrature in red), showing a maximal slope on the quadrature signal at resonance frequency. Hence, tracking the quadrature signal on resonance is the most sensitive way of measuring mode-coupling.

III.2.2   The "self-coupling" limit

A very important and interesting point in Eq. (III.1) is that no assumption was made on the couple of values (n, m). Hence this property should still be valid for $n = m$, the physical interpretation of which is to couple one mode *with itself*. Note that this is however different from the basic Duffing non-linear effect, since we assume that two distinct excitation tones are present for the same mode n. What is actually studied is the coupling between the two tones. This idea of "self-coupling" has already been mentioned in Sec. II.4, and we present here the detailed analysis of this effect for $n = m = 0$ without losses of generality (dropping the indexes when possible).

As for the mode-coupling scheme, we use two driving forces but exciting the *same* mode at slightly detuned frequencies. Note that this phenomenon has been introduced by the group of E. Buks in Refs. [Almog *et al.* 2006, Almog 2007], where theoretical calculations are developed. However, since our work is performed in a different limit, leading to different results, we briefly expose in the following the basics of the self-coupling theory for our schemes obtained with the help of Andrew Armour, and we will compare our findings with those of Refs. [Almog *et al.* 2007] in the next section.

Starting from the second law of Newton, we have:

$$\ddot{x} + \Delta\omega\, \dot{x} + \omega_0\, x + \gamma\, x^3 = f_{L,p} \cos\left(\omega_p\, t\right) + f_{L,s} \cos\left(\omega_s\, t + \delta\phi\right), \qquad \text{(III.3)}$$

with $f_{L,s}$ and $f_{L,p}$ the "sweep" and "pump" forces (normalised to the mode mass)

driving the NEMS respectively at ω_s and ω_p, with $f_{L,s} < f_{L,p}$, $\omega_s \neq \omega_f$ and $\delta\phi$ the phase difference between the two signals. The experimental set-up is again the same as presented in Sec. II.4, with an adder which combines both signals at ω_s and ω_p.

Since we work close to the resonance frequency of the NEMS, we define for clarity:

$$\omega_p = \omega_0 + \delta_p \qquad \omega_s = \omega_p + \delta_s, \tag{III.4}$$

where δ_p and δ_s are the new sweeping parameters relative to ω_0. By construction, we have $\delta_s \neq 0$.

Writing x_0 the general solution of Eq. (III.3) we assume that it has the form:

$$x_0 = \frac{X_0 \, e^{i\,\omega_p\,t} + X_0^\star \, e^{-i\,\omega_p\,t}}{2}. \tag{III.5}$$

Replacing in Eq. (III.3) with $\beta = \frac{3\,\gamma}{8\,\omega_0}$, we obtain:

$$\dot{X}_0 = -\left(\frac{\Delta\omega}{2} + i\,\delta_p\right) X_0 + i\,\beta\,X_0^2\,X_0^\star + \frac{1}{2\,i\,\omega_0}\left(f_{L,p} + f_{L,s}\,e^{i\,\delta_s\,t + \delta\phi}\right), \tag{III.6}$$

where we assumed that X_0 is a slow variable ($\dot{X}_0 \ll \omega_0\,X_0$), that we are in the high quality factor limit ($\Delta\omega \ll \omega_0$), and working close to the resonance frequency $\left(\frac{\omega_p^2 - \omega_0^2}{2\,\omega_p} \approx \delta_p\,,\ \frac{\beta}{\omega_p} \approx \frac{\beta}{\omega_0}\right)$. At first order, we can solve Eq. (III.6) by writing:

$$X_0 = a_p + a_s\,e^{i\,\delta_s\,t} + a_i\,e^{-i\delta_s\,t}, \tag{III.7}$$

with a_p, a_s, a_i the complex variable amplitudes of the NEMS respectively at ω_p, $\omega_p + \delta_s$, $\omega_p - \delta_s$, with a_p the leading term governed by $f_{L,p}$ (the "pump", resonating at $\omega_0 + \delta_{p,max}$), a_s mostly controlled by $f_{L,s}$ (the "sweep", resonating at $\omega_p + \delta_{s,max}$) and a_i its symmetric image through a_p (the "idler", resonating at $\omega_p + \delta_{i,max}$). We thus have $|a_s|$, $|a_i| < |a_p|$, and we will assume that a_s and a_i are small enough not to induce any non-linear terms.

Replacing Eq. (III.7) in Eq. (III.6) and using again the rotating wave approximation, we obtain the following system of equations for the different components of angular frequency relative to ω_p:

$$e^{i\,0} \ : \quad a_p = \frac{f_{L,p}}{2\,\omega_0}\frac{1}{\beta\,|a_p|^2 - \delta_p + i\,\frac{\Delta\omega}{2}}, \tag{III.8a}$$

$$e^{i\,\delta_s} \ : \quad a_s = \frac{\frac{f_{L,s}\,e^{i\,\delta\phi}}{2\,\omega_0} - \beta\,a_p^2\,a_i^\star}{2\,\beta\,|a_p|^2 - \delta_p - \delta_s + i\,\frac{\Delta\omega}{2}}, \tag{III.8b}$$

$$e^{-i\,\delta_s} \ : \quad a_i = \frac{-\beta\,a_p^2\,a_s^\star}{2\,\beta\,|a_p|^2 - \delta_p + \delta_s + i\,\frac{\Delta\omega}{2}}. \tag{III.8c}$$

Isolating each variable and expressing them as a function of a_p, we finally have:

$$a_p = \frac{f_{L,p}}{2\,\omega_0}\ \frac{1}{\beta\,|a_p|^2 - \delta_p + i\,\frac{\Delta\omega}{2}}, \tag{III.9a}$$

$$a_s = \frac{f_{L,s}\,e^{i\,\delta\phi}}{2\,\omega_0}\ \frac{1}{2\,\beta\,|a_p|^2 - \delta_p - \delta_s + i\,\frac{\Delta\omega}{2} - \dfrac{\beta^2\,|a_p|^4}{2\,\beta\,|a_p|^2 - \delta_p + \delta_s - i\,\frac{\Delta\omega}{2}}}, \tag{III.9b}$$

$$a_i = \frac{f_{L,s}\,e^{-i\,\delta\phi}}{2\,\omega_0}\ \frac{1}{2\,\beta\,|a_p|^2 - \delta_p + \delta_s + i\,\frac{\Delta\omega}{2} - \dfrac{\beta^2\,|a_p|^4}{2\,\beta\,|a_p|^2 - \delta_p - \delta_s - i\,\frac{\Delta\omega}{2}}}$$

$$\times \frac{\beta\,a_p^2}{2\,\beta\,|a_p|^2 - \delta_p - \delta_s - i\,\frac{\Delta\omega}{2}}. \tag{III.9c}$$

We observe that Eq. (III.9a) is exactly the same as Eq. (II.26), remembering that $\delta_p = \omega_p - \omega_0$ is the frequency sweep variable for the component a_p. We thus have a single Duffing resonance at ω_p. However, while Eq. (III.9a) is a non-linear equation in a_p, both Eq. (III.9b) and Eq. (III.9c) are *linear* with respect to a_s and a_i.
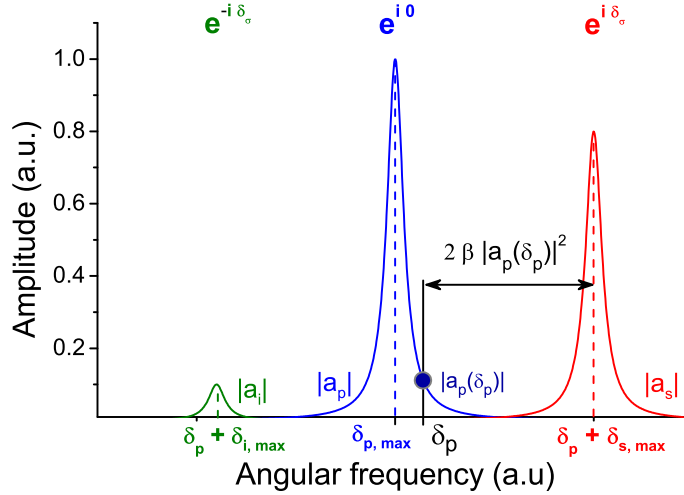
Figure III.5: Overall schematic of the resonances around $\delta_{p,\,max}$ (shifted from ω_0) in the limit of small displacements (normalised amplitude R), with a leading term $|a_p|$ at $\delta_{p,\,max}$, a small term $|a_s|$ at $\delta_p + \delta_{s,\,max}$ which shifts with respect to $|a_p\,(\delta_p)|$ and its symmetric $|a_i|$ at $\delta_p + \delta_{i,\,max}$ which is extremely small.

To better understand Eq. (III.9b) and Eq. (III.9c), let us first consider the simple case where a_p is linear ($\beta\,|a_p|^2 \ll \frac{\Delta\omega}{2}$, but still $|a_s|, |a_i| < |a_p|$). At lowest order in

a_p we have:

$$a_p = \frac{f_{L,\,p}}{2\,\omega_0}\; \frac{1}{-\delta_p + i\,\frac{\Delta\omega}{2}}, \tag{III.10a}$$

$$a_s = \frac{f_{L,\,s}\,e^{i\,\delta\phi}}{2\,\omega_0}\; \frac{1}{2\,\beta\,|a_p|^2 - \delta_p - \delta_s + i\,\frac{\Delta\omega}{2}}, \tag{III.10b}$$

$$a_i = \frac{f_{L,\,s}\,e^{-i\,\delta\phi}}{2\,\omega_0}\; \frac{1}{2\,\beta\,|a_p|^2 - \delta_p + \delta_s + i\,\frac{\Delta\omega}{2}}\; \frac{\beta\,a_p^2}{2\,\beta\,|a_p|^2 - \delta_p - \delta_s - i\,\frac{\Delta\omega}{2}}. \tag{III.10c}$$

In this configuration we observe that a_s and a_i, where the sweeping parameters are δ_s and $-\delta_s$, behave like shifted linear Lorentzian resonance lines (see Fig. III.5). Note that in Eq. (III.10c) the last term of the right hand side can be approximated to $\frac{2\,i\,\beta\,a_p^2}{\Delta\omega}$ when a_s is close to resonance, reducing a_i to almost zero.
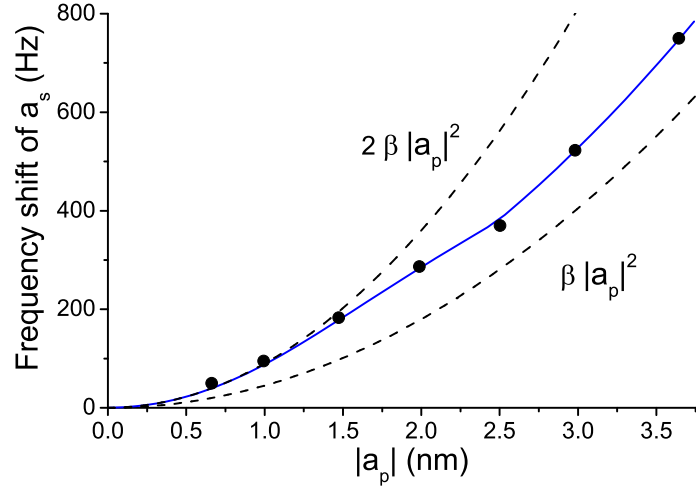
Figure III.6: Frequency shift of the a_s component as a function of the amplitude of a_p, with the data points in black and the analytical calculation from Eq. (III.9b) in blue. At small amplitudes, the shift of a_s follows the $2\,\beta\,|a_p|^2$ dependence, as expected from Eq. (III.10b), and should reach $\beta\,|a_p|^2$ at very large ones (dashed lines).

The important feature in Eq. (III.10b) is that the shift of a_s scales as $2\,\beta\,|a_p|^2$ (Fig. III.6): we can deduce the amplitude of a_p by measuring the shift of a_s (lighter data in Fig. III.7). We thus transduce a displacement into a frequency shift, just as in the mode-coupling scheme, but using one single mode driven with two tones. Note that the shift goes as $2\,\beta$, as we have indeed $\beta_{n,\,m=n} = 2\,\beta_n$ in Eq. (III.2) with β_n the standard Duffing parameter of mode n. For our low stress 15 μm long doubly-clamped beam, it represents a shift of $2\,\beta \approx 90$ Hz.nm^{-2}. However, as we increase a_p eventually the pump component reaches the non-linear regime ($2\,\beta\,|a_p|^2 \approx \frac{\Delta\omega}{2}$), Eq. (III.10) looses validity, and the frequency shift in the expression of a_s tends towards $\beta\,|a_p|^2$ in a non-trivial way (Fig. III.6 and darker data in Fig. III.7). The

amplitude a_i approaches the one of a_s, being its exact symmetric with respect to ω_p.
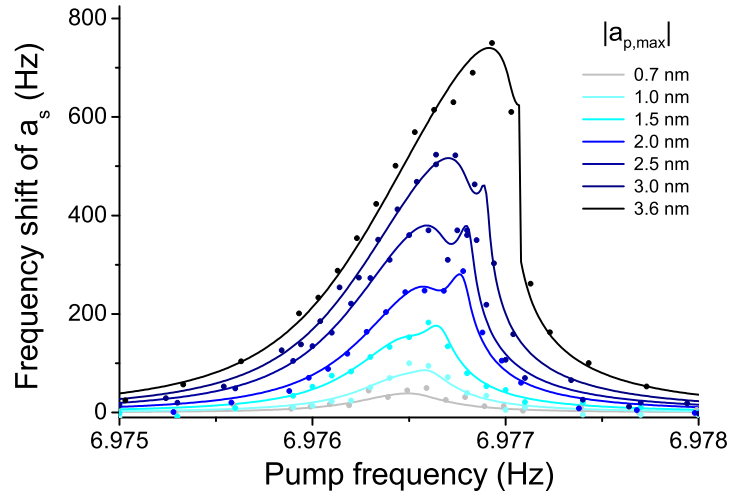
Figure III.7: Shift of the resonance frequency of a_s (linear resonance of amplitude 1 nm) as we sweep through a_p for different excitation amplitudes (inset). At small amplitudes, the shift of a_s follows the resonance shape of $|a_p|$, but as a_p starts to be non-linear new features emerge (see "spiky" zones).

Transducing motion (meters) into frequency (hertz), our measurement only suffers from our ability to define the position of the a_s resonance (see scatter in Fig. III.6 and Fig. III.7). Ultimately, this is limited by the phase noise of the whole circuit, electronics and NEMS included. Optimising the technique, it becomes possible to measure the a_p resonance line (Fig. III.7) at various excitation amplitudes with a very good precision [Defoort *et al.* 2013a].

III.3 Confidential

This section is confidential.

III.4   Conclusion

New features emerge from non-linearities, and we saw in this chapter that in particular we can use them as a way to couple mechanical modes in NEMS. In a first section we exposed how the modes of a resonator may affect each other within the same device. Through this dispersive coupling deriving from the Duffing term $\gamma\,x^3$ in the dynamics equation, a driven mode alters another one by shifting its resonance frequency with the square of the former's amplitude of motion. This technique enables the measurement of the resonance frequency and the linewidth of a mode by looking at another one's position: we transduce the displacement (meters) into a shift in frequency (hertz). Applying this property for a *single* mode, we then show both analytically and experimentally that it is possible to couple one mode with itself in a so-called "self-coupling" scheme, and to reproduce in a similar manner at first order the features observed in mode-coupling. It is thus possible to measure precisely one mode by looking at its own resonance frequency with a two-tone drive scheme [Defoort *et al.* 2013a].

III.5 Perspectives

This section is confidential.

III.6   Résumé

Une des implications directe des phénomènes non-linéaires dans un système est la possibilité de le coupler avec son environnement. En particulier, deux modes de résonance d'un même NEMS peuvent être couplés entre eux. Dû à la tension présente dans l'ensemble de la structure lors de l'excitation d'un mode n, la forme d'un autre mode m en est altérée, ce qui a pour effet de décaler sa fréquence de résonance ω_0 en fonction du couplage non-linéaire $\beta_{n,m}$ entre les modes n et m, et du carré de l'amplitude de déplacement x du mode n (Fig. III.2). Le dispositif expérimental à double-ton permettant d'exciter le NEMS simultanément aux dréquences de résonance des modes n et m peut alors être considéré comme une nouvelle technique de détection précise d'un mode en en observant un autre. Cette technique nous a permis de mesurer des modes jusque là inaccessibles dans notre configuration expérimentale (Fig. III.3).

Dans le cadre de notre travail, nous avons également mis à profit la non-linéarité de nos résonateurs pour coupler un mode avec lui-même. Pour cette configuration, le dispositif expérimental est similaire à celui du couplage standard. Un premier signal est envoyé sur le NEMS pour scanner la résonance d'un mode n tandis qu'un second signal excite le même mode n, mais à fréquence fixe et très légèrement décalé de la fréquence de la première excitation, si bien que ce signal n'a pour effet que de décaler la raie de résonance perçu par la première excitation (Fig. III.5). Les deux excitations sont couplées dispersivement dans la structure. A l'aide de notre collaborateur Andrew Armour, nous avons développé le modèle théorique analytique permettant de prédire le décalage de la raie de résonance perçu à la fréquence d'excitation du premier signal, en fonction de la fréquence et de l'amplitude d'excitation du deuxième signal. Comparant cela avec nos résultats, nous observons un accord quantitatif entre le modèle analytique et nos mesures (Fig. III.7). Notons que, pour des excitations suffisamment faibles, le paramètre de couplage entre ces deux excitations correspond précisément au double du coefficient non-linéaire β de ce même mode (Fig. III.6). Dans le régime linéaire, ce dispositif expérimental permet donc de traduire une raie de résonance initialement mesurée avec la loi de Lenz en Volt, en une résonance déduite de ses mesures en décalage en fréquence en Hertz, dont la précision est alors idéalement limitée uniquement par le bruit en phase du circuit [Defoort *et al.* 2013a].

La dernière section de ce chapitre est confidentielle.

CHAPTER IV

Dynamical bifurcation

Contents

IV.1   Introduction

The bifurcation process is of ubiquitous importance in Science in both static and dynamical systems. This effect has been studied over the years in different fields: transitions in Josephson junctions [Turlot *et al.* 1989], fluctuations in SQUIDs [Kurkijärvi 1972], magnetisation reversal in molecular magnets [Novak *et al.* 1995], switches in cells [Ozbudak *et al.* 2004], stochastic switching in micro-cantilevers [Venstra *et al.* 2013], the list being non-exhaustive. This non-linear phenomenon can be described at first order by a particle evolving in a pseudo-potential escaping with a sort of attempt frequency Γ from a metastable state to a stable one separated by the analogue of an activation energy E_a. While being present in various disciplines, the analytical scalings of E_a and Γ are supposed to be universal with the detuning from the bifurcation point, at least when very close to it.

Measuring those two parameters (Γ and E_a) in a wide range requires specific and demanding properties of the measuring tool. In the case of dynamical systems, the resonating period needs to be high enough to decorrelate the oscillation and the bifurcation frequency, while the dissipation needs to be high enough to guarantee immediate relaxation in the time-scale of the bifurcation process. Nano-mechanical resonators can be made in order to satisfy those two requirements, while still having a good quality factor for accurate measurements. They are thus perfect candidates to probe the bifurcation phenomenon. In the case of our goalpost, another feature makes it ideal for this study: it is intrinsically highly linear. By means of the capacitive gate voltage, we can thus control the non-linearity at a fixed driving amplitude (Chap. II), opening a new dimension of investigation: the non-linear coefficient itself, which is at the core of the phenomenon, is here a control parameter.

In this chapter we first present in a brief section different bifurcation phenomena and some of the work done to understand their behaviour, both theoretically and experimentally. In a second step we introduce the basics of the analytical theory which leads to the universal scaling laws and present the numerical calculation that will be compared to the experimental results. We then explain the experimental procedure used to measure the relaxation process and we show that the resonance frequency presents an intrinsic noise that needs to be carefully characterised. We will finish by presenting the measurement of the scaling laws obtained with our NEMS as a function of both detuning and non-linearity, from the analytical range up to two orders of magnitude beyond its limit. The results will also be compared to exact numerical calculations, and their implication will be discussed.

IV.2   State-of-the-art

IV.2.1   Hysteresis and bifurcation process

Non-linearities are the essence of complex systems, and new physics emerge from them with interesting new behaviours. The hysteresis is a perfect example of the richness and the complexity of non-linear dynamics. A hysteresis can be defined by the following: a system in which different states exist at a given working point with the actual steady state depending on the system's history. Hysteresis is not just a mathematical concept, it is expressed in physics, in biology, in finance [Blanchard & Summers 1986] and even in social science (Fig. IV.1). Nevertheless, this concept is of crucial importance in experimental physics, and in many mechanisms one has to be careful about the dynamical path followed by the system.

(a)   (b)
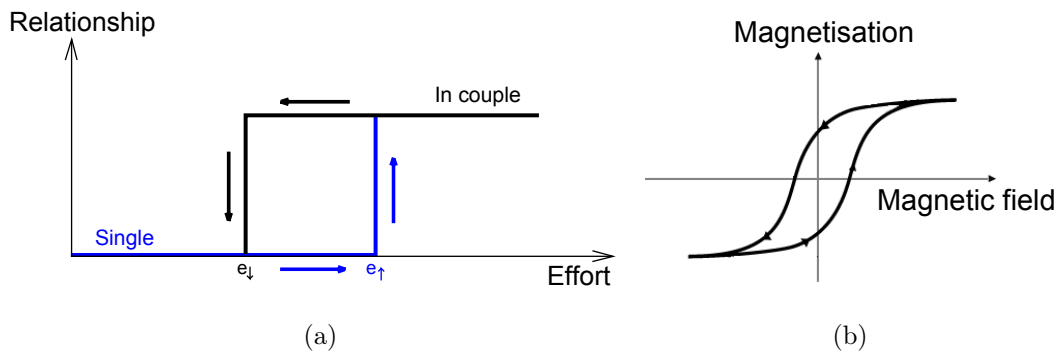
Figure IV.1: Examples of a hysteresis in different fields. *a*: In social science, when a single person tries to be in a relationship, he/she will make some efforts until reaching this status (here at $e_\uparrow$). If now this person decreases its amount of efforts, a strange phenomenon appears: the couple might still exist even below $e_\uparrow$. It's only when the person reduces its efforts below $e_\downarrow$ that he/she will go back to the single status. In-between $e_\downarrow$ and $e_\uparrow$, we observe a hysteresis: for the same amount of efforts, depending on its history, the person might be either single or in a relationship. *b*: In physics, example of a ferromagnetic polarisation hysteresis. As the magnetic field increases/decreases, the magnetisation of the magnet can be smoothly oriented upwards/downwards with respect to the field axis. While due to microscopic domain reorientation, the curve is continuous on a macroscopic level.

Note that in physics there are commonly two types of hysteretic behaviours: the one originating from a first order transition, and the others. As such, the first derivative of a hysteresis as a function of the sweeping axis can be either discontinuous or continuous in the transition range. The transition from liquid to gas with the nucleation of bubbles as a function of temperature is abrupt, similarly to the process shown in Fig. IV.1a. On the other hand, the ferromagnetic polarisation in a soft ferromagnet occurs smoothly along the magnetic field's axis (Fig. IV.1b). In this chapter, we will only focus on the former kind of hysteresis, encountered in first order transitions.

This emergent phenomenon can be described through a tilted double well potential (typically by a polynomial equation of the 4th order, with respect to some configuration parameter X), with a particle in one of those wells (Fig. IV.2).
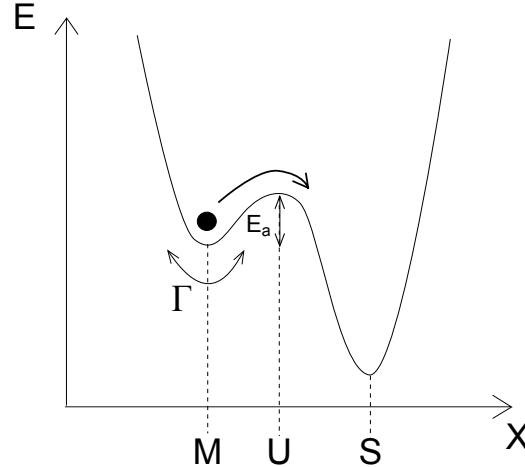
Figure IV.2: Particle evolving in a double well potential (energy as a function of a configuration parameter X). If the particle has enough energy, it can cross the unstable state U of energy barrier E_a with an attempt frequency Γ and switch from the metastable M to the stable state S.

If this particle has enough energy to overcome the barrier that separates the two wells, it has a probability to switch to the deeper well: the particle relaxes from the metastable state M to the stable state S, crossing the unstable one U. This transition between two states is called the bifurcation process. The phenomenon is stochastic with a Poissonian distribution of events, leading to an exponential distribution of escape times:

$$P_{bif}\left(t\right) = \Gamma_{esc}\, e^{-\Gamma_{esc}\, t}, \qquad\qquad (IV.1)$$

with Γ_{esc} the rate of the transition and P the probability to bifurcate from one state to the other. This principle is exactly what is behind the transitions in chemical reactions [Kramers 1940] - transition from the reactants (state M) to the products (state S), which is described by the Arrhenius law:

$$\Gamma_{esc} = \Gamma\, e^{-\frac{E_a}{k_B T}} \qquad\qquad (IV.2)$$

with Γ the attempt frequency, E_a the activation energy needed to switch, and $k_B T$ the thermal fluctuations' energy of the system (Fig. IV.2). When the energy barrier E_a vanishes to zero, metastable and unstable states merge: we call this limit the bifurcation point. However, if the energy barrier is non-zero, thermal noise would eventually make the system relax to the stable state.

This equation describes the transition rate for any bifurcation phenomena, even though the dynamics differs. In the case of the transition from liquid to gas of a droplet, the system is static, while the fluctuations in SQUIDs are dynamic: the

system is oscillating at some high frequency ω. But in the latter case, the bifurcation is studied within this oscillation, such that in the SQUID's dynamics referential the phenomenon is similar to the static case.

In the 80's analytical calculations demonstrated remarkable universal features behind this transition process (mostly Refs. [Dykman & Krivoglaz 1979] and [Dykman & Krivoglaz 1980]). These theoretical results state that, under restrictive conditions, any hysteretical system has the same dependency on the distance to the bifurcation point, and shall be described as:

$$\Gamma = \Gamma_0 \, \delta^\zeta \qquad E_a = E_0 \, \delta^\xi \qquad\qquad \text{(IV.3)}$$

with Γ_0 and E_0 the prefactors of Γ and E_a, δ the distance to the bifurcation point and ζ and ξ the exponents predicted to be universal with values $\zeta = \frac{1}{2}$ and $\xi = \frac{3}{2}$.

IV.2.2   Investigation with MEMS/NEMS

Recently, the accuracy and the versatility of MEMS and NEMS have been used to probe these dependencies. Indeed those oscillators eventually become "Duffing" non-linear when driven at high enough amplitude (Sec. II.5).
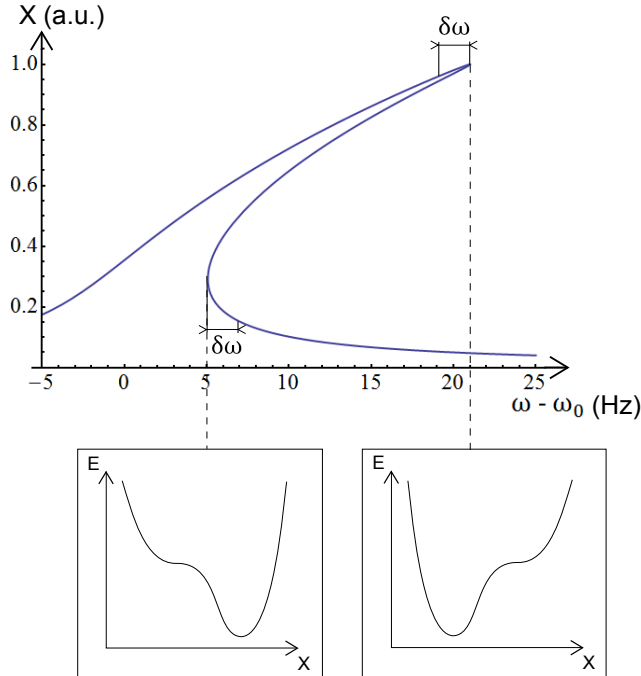
Figure IV.3: Resonance line of a Duffing oscillator presenting a large hysteresis (here for $\beta > 0$). As we reduce the detuning $\delta\omega$ from the edges of the hysteresis the energy barrier in the pseudo-potential also reduces, until vanishing at the bifurcation frequencies as shown in the insets.

In this regime, an hysteresis opens within the resonance line, leading to two dynamic states: one with large and the other one with small amplitude, see Fig. IV.3. In the metastable state, the energy barrier E_a vanishes as we get closer to the edges of the hysteresis (which are the bifurcation points), until the system relaxes to the low energy state. The distance to the bifurcation point δ is then directly linked to the detuning to the edge of the hysteresis $\delta\omega \propto \delta$. The control of this detuning is thus an open window to probe the universal exponents ζ and ξ. By measuring an appropriate amount of relaxation [Eq. (IV.1)], one can extract Γ_{esc} and investigate the bifurcation phenomenon.

J.S. Aldridge and A.N. Cleland worked on extracting both ξ and E_a using an aluminium nitride beam at cryogenic temperature with a magnetomotive scheme [Aldridge & Cleland 2005].
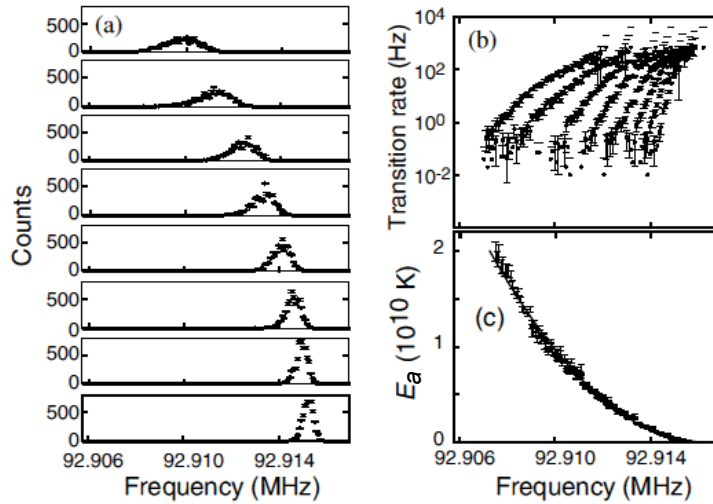
Figure IV.4: Figure adapted from Ref. [Aldridge & Cleland 2005]. *a* Switching histograms for different noise intensities at the right-side bifurcation frequency: from high to low amplitude state. Noise intensity is increased from bottom to top. *b* Transition rates extracted from switching histograms. *c* Calculated activation energy E_a extracted from transition rates and variation in noise intensity.

They drove the NEMS in the Duffing regime (positive stretching non-linearity) and measured the *saddle-node bifurcation* phenomenon. The experimental procedure was to sweep the frequency through the bifurcation point in the presence of noise at a low enough rate to be in the adiabatic regime, and to record the exact frequency at which the system relaxes to the stable state. Since the bifurcation process is of statistical origin, the experiment has to be repeated enough times to extract relevant parameters. For a given set of parameters, they could obtain a histogram of relaxation frequencies (Fig. IV.4) and extract Γ_{esc} from it. Changing the noise level I_N (analogue of $k_B T$ in Eq. [IV.2]), they could separate Γ from E_a, and then E_0 from δ with the histograms of the relaxation frequencies. They

hence measured quantitatively the activation energy E_a and the universal exponent ξ for both edges of the hysteresis. They obtained an agreement between numerical calculations and the experiment within a factor 2, and found $\xi = 2$, which they compared to the configuration where the activation energies between the two states are the same, as presented in Ref. [Dykman & Krivoglaz 1979]. The factor of 2 off on E_a (quite large considering the exponential dependency) was attributed to the noise calibration, which appears to be a parameter difficult to measure accurately.
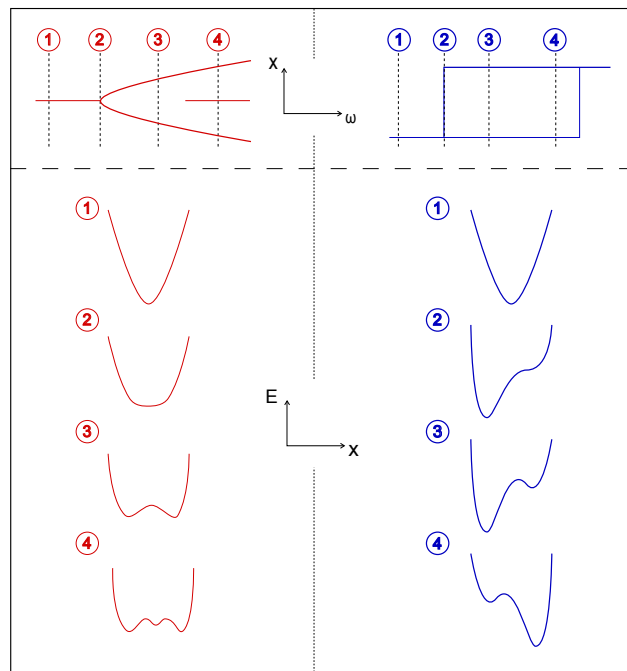
Figure IV.5: Representation of the pitchfork (red) and the saddle-node Duffing (blue) bifurcation processes. The sketches at the top represent the transition from a single position state x to a multi-state configuration while tuning an arbitrary parameter (here the drive frequency ω). The sketches at the bottom show the energy of the system as a function of the displacement amplitude at the given configuration (represented by the numbers). For the pitchfork process the bifurcation occurs when entering in the multi-stable states regime, while the system is kept in the stable state for the Duffing process. In the Duffing regime, the bifurcation only appears close to the opposite edge of the hysteresis. Note that in this regime the hysteresis ends by a single-state solution while the pitchfork' hysteresis continues by a triple-state solution.

H.B. Chan and co-workers studied the phenomenon through a different procedure. Using a torsional MEMS, they measured the relaxations in a passive way: in the non-linear regime and close to the bifurcation point, they let the driving frequency fixed and waited for the MEMS to relax due to injected noise. This procedure, much more adiabatic than the first one, was experimented with two drive amplitude methods. With a standard capacitive drive leading at high amplitudes to

a Duffing oscillator behaviour (with negative non-linearity), they could extract the power scaling law ξ of two similar samples measured at different temperatures: at liquid nitrogen and helium [Stambaugh & Chan 2006]. They measured power laws of respectively 1.38±0.15 and 1.4±0.15, which is in good agreement with the theory [Eq. (IV.3)].

The other method was to drive the resonator in a parametric regime, where motion is induced at half the modulation frequency [Chan & Stambaugh 2007]. In this regime the two bifurcation points have a different potential behaviour. At the entrance of the multi-stable regime, the monostable state splits in two symmetric stable states separated by the unstable one at zero-motion amplitude (Fig. IV.5). The new stable states, having the same motion amplitude, differ by a π phase. As the driving frequency crosses the second bifurcation point, the zero-motion state becomes stable again and the system is now composed of three states, with a switch in both amplitude and phase. This is typical of the *pitchfork bifurcation* process, and in this specific case the potential is symmetric and the universal scaling law is $\xi = 2$ for both bifurcation points [Dykman *et al.* 1998]. In Ref. [Chan & Stambaugh 2007] the authors experimentally find 2.0±0.1 for the first bifurcation point and 2.0±0.03 for the second one. Note that for large detunings, they measured a deviation from the universal behaviour.
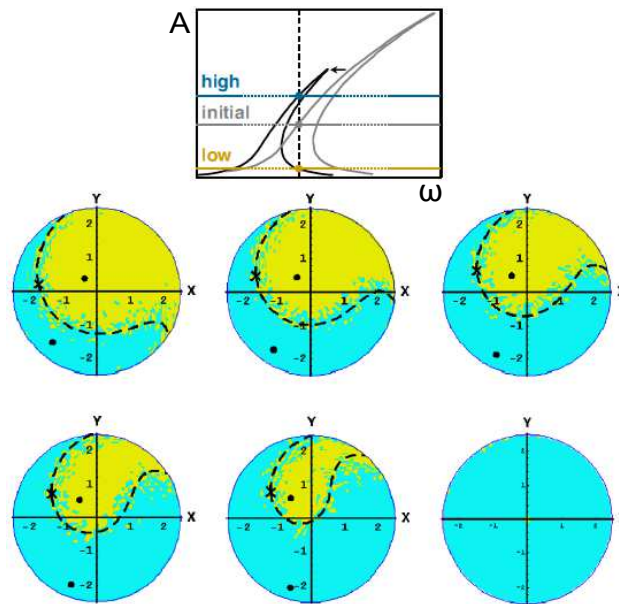
Figure IV.6: Figures extracted from Ref. [Kozinsky *et al.* 2007]. The top figure shows the experimental process, as explained in the text, with A the amplitude of oscillation and ω the drive frequency. The six circles are the results for different final drive amplitudes. Each circle shows whether the NEMS moves to the high (blue) or to the low (yellow) amplitude as a function of the initial drive and the phase difference with the final drive (represented here by X and Y, the in-phase and quadrature signals).

Another experimental set-up was presented from the group of M.L. Roukes using a doubly-clamped platinum nano-wire [Kozinsky *et al.* 2007]. They experimentally defined the two basins of attraction of a positive non-linear Duffing resonator - around the high amplitude state and the low one. Initiating the NEMS at a given amplitude (in the bistable regime or not), they switched the initial drive to the final one, tuning both phase and amplitude, and measured whether the NEMS finished in the high or in the low amplitude state (Fig. IV.6). According to those results they could map out the bifurcation process as a function of the two variables of the problem: phase and amplitude.

Those works are not the only ones existing, but they introduce different ways of analysing the bifurcation process in MEMS/NEMS. In our experiment, we chose to excite a NEMS with a standard drive in the bistable regime close to one of the bifurcation points and to wait for the NEMS to relax in presence of noise, performing the so-called "saddle-node bifurcation process" (essentially the same technique as the one presented for a MEMS in Ref. [Stambaugh & Chan 2006]). Our first motivation is to understand how the bifurcation process evolves as we tune the parameter at the core of the phenomenon: the non-linearity itself. Using this new free parameter, it is possible to explore the range where the approximated analytical theory supposedly breaks down [Eq. (IV.3)] and to probe the behaviour and the universal exponents ζ and ξ of the bifurcation in this region. To achieve such an experiment, it is first important to understand the non-linear dependency and the limit of applicability of Eq. (IV.3).

IV.3 Theory

IV.3.1 The approximated 1D theory

Some of the works presented here are inspired by the papers of M.I. Dykman and M.A. Krivoglaz [Dykman & Krivoglaz 1979, Dykman & Krivoglaz 1980]. However in these cited papers, the experiment proposed to test the theory consisted in fixing the driving frequency and tuning the driving amplitude, while we are willing to do the opposite. It is essentially a question of renormalisation, but since the essence of the experiment is to compare measured results with theory, it is convenient to summarise here the ideas of the *saddle-node bifurcation* process and rewrite the relevant expressions. In the following we present the work done by Vadim Puller and Fabio Pistolesi, our collaborators.

Starting from the Duffing oscillator equation Eq. (II.5), we have to take into account the noise injected in the system:

$$\ddot{x} + \Delta\omega\,\dot{x} + {\omega_0}^2\,x + \gamma\,x^3 = f_0\,cos(\omega\,t) + f_N(t) \tag{IV.4}$$

with f_0 and f_N the drive and noise forces normalised to the mass m. In the following, we will assume that the NEMS is bistable, which is expressed in non-linear terms by Eq. (II.18). The noise is characterised by the correlation function:

$$\langle f_N(t)\,f_N(t')\rangle = 2\,I_N\,\delta\left(t - t'\right) \tag{IV.5}$$

with I_N the force noise spectral power intensity, an analogous (within a factor $\Delta\omega$) to the thermal noise energy $k_B\,T$ in Eq. (IV.2). We can then write the system of equations:

$$\dot{x} = y \tag{IV.6a}$$

$$\dot{y} = -\Delta\omega\,y - {\omega_0}^2 x - \gamma\,x^3 + f_0\,\cos(\omega\,t) + f_N(t). \tag{IV.6b}$$

We introduce the new motion variable z such that:

$$x(t) = z(t)\,e^{i\,\omega\,t} + z(t)^*\,e^{-i\,\omega\,t} \tag{IV.7a}$$

$$y(t) = i\,\omega\,z(t)\,e^{i\,\omega\,t} - i\,\omega\,z(t)^*\,e^{-i\,\omega\,t} \tag{IV.7b}$$

assuming z is a slow variable: $\dot{z} \ll \omega z$. We then obtain from Eq. (IV.6b) the equation for the new variable in the rotating wave approximation:

$$\dot{z} = -\left[i\,(\omega - \omega_0) + \frac{\Delta\omega}{2}\right]\,z + i\frac{3\gamma}{2\,\omega}\,|z|^2\,z - i\,\frac{f_0}{4\,\omega} - i\,\frac{f_N(t)\,e^{-i\,\omega\,t}}{2\,\omega} \tag{IV.8}$$

in the limit where $\omega \approx \omega_0$. It is convenient to define the new time variable $\tau = \frac{\Delta\omega\,t}{2}$ and to normalise the motion variable z:

$$Z(\tau) = \sqrt{\frac{3\,\gamma}{\omega\,\Delta\omega}}\,z\left(\frac{2\,\tau}{\Delta\omega}\right). \tag{IV.9}$$

Note that until the end of this section, the "dot" notation will now refer to the derivative with respect to τ. From Eq. (IV.8) we now have:

$$\dot{Z}(\tau) = -\left(i\,\Omega + 1\right)Z(\tau) + i\,|Z(\tau)|^2\,Z(\tau) - i\,F_0 - i\,F_N(t), \tag{IV.10}$$

with

$$\Omega = \frac{2\,(\omega - \omega_0)}{\Delta\omega}, \quad F_0 = \frac{\sqrt{3\,\gamma}\,f_0}{2\,(\omega\,\Delta\omega)^{3/2}}, \quad F_N(t) = \frac{\sqrt{3\,\gamma}\,f_N(t)\,e^{-i\omega t}}{(\omega\,\Delta\omega)^{3/2}}, \tag{IV.11}$$

respectively the relative normalised driving frequency and the renormalised drive and noise forces. Without noise we obtain the stationary solution:

$$Z_0 = \frac{F_0}{|Z_0|^2 - \Omega + i} = |Z_0|\,e^{i\,\phi_0}, \tag{IV.12}$$

with

$$|Z_0| = \frac{F_0}{\sqrt{\left(|Z_0|^2 - \Omega\right)^2 + 1}}, \tag{IV.13a}$$

$$\sin\left(\phi_0\right) = \frac{-1}{\sqrt{\left(|Z_0|^2 - \Omega\right)^2 + 1}}, \quad \cos\left(\phi_0\right) = \frac{|Z_0|^2 - \Omega}{\sqrt{\left(|Z_0|^2 - \Omega\right)^2 + 1}}. \tag{IV.13b}$$

To simplify the calculations, we turn the phase of our variable Z to fix the stationary solution real with $\widetilde{Z}(\tau) = Z\left(\tau\right)e^{-i\,\phi_0}$.

If we now look separately at both real and imaginary parts of Eq. (IV.10) using $\widetilde{Z}(\tau) = \widetilde{Z}_{\mathbb{R}}\left(\tau\right) + i\,\widetilde{Z}_{\mathbb{I}}\left(\tau\right)$ [with $\widetilde{Z}_{\mathbb{R}}, \widetilde{Z}_{\mathbb{I}} \in \mathbb{R}$], we write:

$$\dot{\widetilde{Z}}_{\mathbb{R}} = -\widetilde{Z}_{\mathbb{R}} + \Omega\,\widetilde{Z}_{\mathbb{I}} - \left(\widetilde{Z}_{\mathbb{R}}^2 + \widetilde{Z}_{\mathbb{I}}^2\right)\widetilde{Z}_{\mathbb{I}} - F_0\,\sin\left(\phi_0\right) - \Re\left[i\,F_N(t)\,e^{-i\,\phi_0}\right], \tag{IV.14a}$$

$$\dot{\widetilde{Z}}_{\mathbb{I}} = -\widetilde{Z}_{\mathbb{I}} - \Omega\,\widetilde{Z}_{\mathbb{R}} + \left(\widetilde{Z}_{\mathbb{R}}^2 + \widetilde{Z}_{\mathbb{I}}^2\right)\widetilde{Z}_{\mathbb{R}} - F_0\,\cos\left(\phi_0\right) - \Im\left[i\,F_N(t)\,e^{-i\,\phi_0}\right]. \tag{IV.14b}$$

With the new definitions, the stationary point verifies $\widetilde{Z}_{0\,\mathbb{R}} = |Z_0|$ and $\widetilde{Z}_{0\,\mathbb{I}} = 0$, leading to:

$$-\widetilde{Z}_{0\,\mathbb{R}} - F_0\,\sin\left(\phi_0\right) = 0, \quad \left(\widetilde{Z}_{0\,\mathbb{R}}^2 - \Omega\right)\widetilde{Z}_{0\,\mathbb{R}} - F_0\,\cos\left(\phi_0\right) = 0. \tag{IV.15}$$

Linearising near the stationary point, $\widetilde{Z}_{\mathbb{R}} = \widetilde{Z}_{0\,\mathbb{R}} + \widetilde{\delta Z}_{\mathbb{R}}$, $\widetilde{Z}_{\mathbb{I}} = \widetilde{Z}_{0\,\mathbb{I}} + \widetilde{\delta Z}_{\mathbb{I}}$, we obtain:

$$\dot{\widetilde{\delta Z}}_{\mathbb{R}} = -\widetilde{\delta Z}_{\mathbb{R}} + \left(\Omega - \widetilde{Z}_{0\,\mathbb{R}}^2\right)\widetilde{\delta Z}_{\mathbb{I}}, \tag{IV.16a}$$

$$\dot{\widetilde{\delta Z}}_{\mathbb{I}} = \left(3\,\widetilde{Z}_{0\,\mathbb{R}}^2 - \Omega\right)\widetilde{\delta Z}_{\mathbb{R}} - \widetilde{\delta Z}_{\mathbb{I}}, \tag{IV.16b}$$

with the associated eigenvalues:

$$\lambda_{1,2} = -1 \pm \sqrt{\left(\Omega - \widetilde{Z}_{0\,\mathbb{R}}^2\right)\left(3\,\widetilde{Z}_{0\,\mathbb{R}}^2 - \Omega\right)}. \tag{IV.17}$$

In the region we will explore (in the hysteresis of the NEMS), three solutions coexist: two stable states (small and large amplitude oscillation, one being metastable) and an unstable state (the saddle point). At the bifurcation point ($\omega = \omega_{bif}$), the unstable state merges with the metastable one and one of the eigenvalue is zero,

$$\lambda_1 = 0, \quad \lambda_2 = -2. \tag{IV.18}$$

We then have at the bifurcation point:

$$\widetilde{Z}_{bif}^2 = \frac{2\,\Omega_{bif} \pm \sqrt{\Omega_{bif}^2 - 3}}{3}, \quad \Omega_{bif} = \frac{2\,(\omega_{bif} - \omega_0)}{\Delta\omega} \tag{IV.19}$$

with $\widetilde{Z}_{bif}$ and Ω_{bif} the normalised amplitudes and frequencies at the bifurcation points. Near these points, Eq. (IV.16) takes the form:

$$\dot{\widetilde{\delta Z}}_{\mathbb{R}} = -\widetilde{\delta Z}_{\mathbb{R}} + \left(\Omega - \widetilde{Z}_{bif}^2\right)\widetilde{\delta Z}_{\mathbb{I}} = -\widetilde{\delta Z}_{\mathbb{R}} + \cot\left(\phi_{bif}\right)\widetilde{\delta Z}_{\mathbb{I}}, \tag{IV.20a}$$

$$\dot{\widetilde{\delta Z}}_{\mathbb{I}} = \left(3\,\widetilde{Z}_{bif}^2 - \Omega\right)\widetilde{\delta Z}_{\mathbb{R}} - \widetilde{\delta Z}_{\mathbb{I}} = \tan\left(\phi_{bif}\right)\widetilde{\delta Z}_{\mathbb{R}} - \widetilde{\delta Z}_{\mathbb{I}}, \tag{IV.20b}$$

with

$$\sin\left(\phi_{bif}\right) = \frac{-1}{\sqrt{\left(\widetilde{Z}_{bif}^2 - \Omega_{bif}\right) + 1}}, \quad \cos\left(\phi_{bif}\right) = \frac{\widetilde{Z}_{bif}^2 - \Omega_{bif}}{\sqrt{\left(\widetilde{Z}_{bif}^2 - \Omega_{bif}\right) + 1}}. \tag{IV.21a}$$

We can now introduce the variables corresponding to the eigenvalues calculated above:

$$\widetilde{Z}_{1,2} = \widetilde{\delta Z}_{\mathbb{R}}\sin\left(\phi_{bif}\right) \pm \widetilde{\delta Z}_{\mathbb{I}}\cos\left(\phi_{bif}\right), \tag{IV.22}$$

which leads to:

$$\dot{Z}_1 = 0, \tag{IV.23a}$$

$$\dot{Z}_2 = -2\,Z_2. \tag{IV.23b}$$

From this set of equations, we see that at first order Z_2 relaxes much faster than Z_1. This means that as far as the relaxation times measured are larger than $\frac{1}{\Delta\omega}$, the fast variable Z_2 already relaxed to zero and is stable, and only the slow variable Z_1 matters in the evolution process. We thus conclude that in this configuration the initially 2D theory reduces to a rather convenient 1D analytical problem.

It is important to note that this approximation is possible only close to the bifurcation point ω_{bif}. Indeed, if we now look at the frequency where the NEMS' amplitude reaches its maximum ω_{max}, both eigenvalues at this stable point are equal: $\lambda_{1,2} = -1$. Hence at ω_{max} the separation between fast and slow variables loses meaning. Thus the driving frequency ω needs to be in between ω_{bif} and ω_{max}, which also writes:

$$4\,\Omega_{bif}\,|\Omega - \Omega_{bif}| \ll 1. \tag{IV.24}$$

Note also that in most of the relaxation configurations we will present in the following, the NEMS will relax from the upper branch with a large hysteresis ($\Omega_{bif} \gg 1$). In this limit, we have:

$$\sin(\phi_{bif}) \approx 1, \quad \cos(\phi_{bif}) \approx \frac{-1}{2\,\Omega_{bif}}, \quad \widetilde{Z}_{bif} \approx \sqrt{\Omega_{bif}} \qquad \text{(IV.25)}$$

If we now get to the second order in Eq. (IV.16) including the noise and still using the eigenvectors $Z_{1,2}$, we obtain a single equation for the slow variable Z_1:

$$\dot{Z}_1 = g + a\,Z_1 - b\,Z_1^2 + \eta, \qquad \text{(IV.26)}$$

which can be reduced to:

$$\dot{\widetilde{Z}}_1 = \widetilde{g} - b\,\widetilde{Z}_1^2 + \eta, \qquad \text{(IV.27)}$$

with:

$$\widetilde{Z}_1 = Z_1 - \frac{a}{2b}, \quad \tilde{g} = g + \frac{a^2}{4b}, \qquad \text{(IV.28a)}$$

$$g = \frac{|\Omega - \Omega_{bif}|}{2\,\sqrt{\Omega_{bif}}}, \quad a = |\Omega - \Omega_{bif}|\,\Omega_{bif}, \quad b = \frac{\Omega_{bif}^{3/2}}{2}, \qquad \text{(IV.28b)}$$

$$\eta = -\Re[F_N(t)], \quad \langle \eta(\tau)\,\eta(\tau')\rangle = 2\,\widetilde{I}_N\,\delta(\tau - \tau'), \quad \widetilde{I}_N = \frac{3\,\gamma\,I_N}{4\,\omega^3\,\Delta\omega^2}, \qquad \text{(IV.28c)}$$

and from Eq. (IV.24), we have $\tilde{g} \approx g$. Eq. (IV.27) can be described by the Langevin process:

$$\frac{d\widetilde{Z}_1}{d\tau} = \frac{dU}{d\widetilde{Z}_1} + \eta, \quad U\left(\widetilde{Z}_1\right) = \tilde{g}\,\widetilde{Z}_1 - \frac{b}{3}\,\widetilde{Z}_1^3, \qquad \text{(IV.29)}$$

where U is the effective cubic potential in which the NEMS evolves (an approximation at small detunings of the 4th order potential represented in Fig. IV.2). As described in Ref. [Dykman & Krivoglaz 1980], from this one-dimensional problem one can have access to the average escape rate Γ_{esc} needed for the system to relax for the first time from the metastable state to the stable one:

$$\Gamma_{esc} = \frac{\Delta\omega\,\sqrt{bg}}{2\,\pi}\,e^{-E}, \quad E = \frac{4\,g^{3/2}}{3\,\widetilde{I}_N\,b^{1/2}}. \qquad \text{(IV.30)}$$

Using the parameters in Eq. (IV.29), we obtain:

$$\Gamma_{esc} = \frac{\Delta\omega\,\sqrt{|\Omega_{bif} - \Omega|\,\Omega_{bif}}}{4\,\pi}\,e^{-E}, \quad E = \frac{8\,\omega^3\,\Delta\omega^2\,|\Omega - \Omega_{bif}|^{3/2}}{9\,\gamma\,\Omega_{bif}^{3/2}\,I_N}. \qquad \text{(IV.31)}$$

If we now re-write the expression using the experimentally defined parameters, and if we compare with Eq. (IV.3) we finally obtain:

$$\Gamma_{esc} = \Gamma\,e^{\frac{-E_a}{I_N}}, \qquad \text{(IV.32a)}$$

$$\Gamma = \Gamma_0\,|\delta\omega|^{1/2}, \quad E_a = E_0\,|\delta\omega|^{3/2} \qquad \text{(IV.32b)}$$

$$\Gamma_0 = \frac{x^2}{2\,\pi}\,|\beta|^{1/2}, \quad E_0 = \frac{\omega^2\,\Delta\omega^2}{3\,x^3}\,|\beta|^{-5/2}, \qquad \text{(IV.32c)}$$

with x the peak amplitude of motion at the working point (frequency ω) and $\beta = \frac{3\gamma}{8\omega_0}$. From those equations we can effectively extract the universal exponents in Eq. (IV.3): $\zeta = 1/2$ and $\xi = 3/2$ given that $\delta\omega = \omega_{bif} - \omega$ is our detuning parameter. The other remarkable exponents come from the non-linear dependency. As discussed before, the non-linearity is at the core of the Duffing oscillator, and Eq. (IV.32c) shows also standard power law dependencies on β for both the attempt frequency and the activation energy.

Yet, those analytical results suffer from a very narrow range of applicability. One should always satisfy Eq. (IV.24) while $\Omega_{bif} \gg 1$. But the larger Ω_{bif} is, the narrower the detuning $\delta\omega$ can be (see Fig. IV.7).
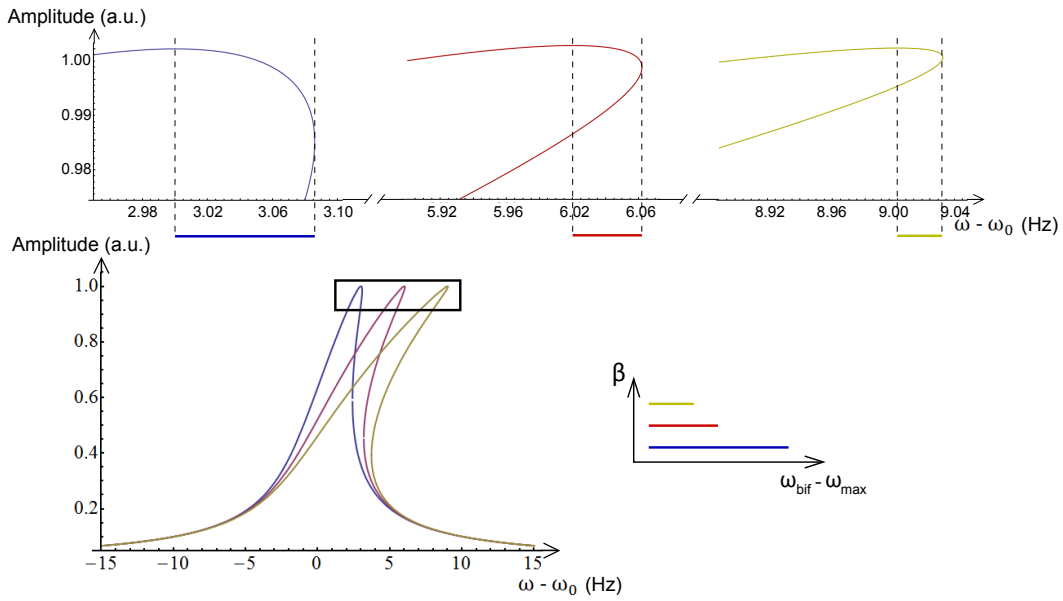
Figure IV.7: Visual representation of the condition Eq. (IV.24). The bottom left plot shows in arbitrary units three resonance lines, with a Duffing non-linear coefficient β varying from simple to triple. At the top we see an identical zoom of each line close to the bifurcation point, and observe that the maximum detuning available $\omega_{bif} - \omega_{max}$ decreases as the non-linearity increases. A global view is represented at the bottom right of the figure.

If on one hand it is difficult to achieve those conditions while we want to map out the non-linear dependency, on the other hand it is both interesting and challenging to investigate what is beyond the analytical theory. However, in order to check the validity of our measurements in this region, we need a theoretical support. While no work has been successful to our knowledge on the 2D analytical theory, comparing our experimental results with numerical calculations is already an achievement.

IV.3.2 Solving the Fokker-Planck equation

Since those 1D results are only an approximation of the full 2D theory and no other valuable analytic approximations has been reached up to now, our collaborators worked on numerical simulations to test the exactness and the limits of these expressions, with the final aim of comparing theory with our experimental results.

The calculation starts from the separation between real and imaginary parts in Eq. (IV.14), taking Z instead of $\widetilde{Z}$ as the stationary solution:

$$\dot{Z}_\mathbb{R} = f\left(Z_\mathbb{R}, Z_\mathbb{I}\right) - \Re\left[i\, F_N(t)\right], \tag{IV.33a}$$

$$\dot{Z}_\mathbb{I} = g\left(Z_\mathbb{R}, Z_\mathbb{I}\right) - \Im\left[i\, F_N(t)\right]. \tag{IV.33b}$$

where

$$f\left(Z_\mathbb{R}, Z_\mathbb{I}\right) = -Z_\mathbb{R} - \left(Z_\mathbb{R}^2 + Z_\mathbb{I}^2 - \Omega\right) Z_\mathbb{I}, \tag{IV.34a}$$

$$g\left(Z_\mathbb{R}, Z_\mathbb{I}\right) = -Z_\mathbb{I} + \left(Z_\mathbb{R}^2 + Z_\mathbb{I}^2 - \Omega\right) Z_\mathbb{R} - F_0. \tag{IV.34b}$$

A description equivalent to that provided by Eq. (IV.33) is obtained by means of a Fokker-Planck equation, which in this case takes the form:

$$\partial_t P\left(Z_\mathbb{R}, Z_\mathbb{I}, t | Z_{\mathbb{R}0}, Z_{\mathbb{I}0}\right) = \widehat{L}_{FP}\, P\left(Z_\mathbb{R}, Z_\mathbb{I}, t | Z_{\mathbb{R}0}, Z_{\mathbb{I}0}\right), \tag{IV.35}$$

where $P\left(Z_\mathbb{R}, Z_\mathbb{I}, t | Z_{\mathbb{R}0}, Z_{\mathbb{I}0}\right)$ is the conditional probability density for the system to be found at the point $Z_\mathbb{R}, Z_\mathbb{I}$ at time t given that it started from $Z_{\mathbb{R}0}, Z_{\mathbb{I}0}$ at $t = 0$. The Fokker-Planck operator is defined here as:

$$\widehat{L}_{FP}\, W\left(Z_\mathbb{R}, Z_\mathbb{I}\right) = -\partial_{Z_\mathbb{R}}\left[f\left(Z_\mathbb{R}, Z_\mathbb{I}\right) W\left(Z_\mathbb{R}, Z_\mathbb{I}\right)\right] - \partial_{Z_\mathbb{I}}\left[g\left(Z_\mathbb{R}, Z_\mathbb{I}\right) W\left(Z_\mathbb{R}, Z_\mathbb{I}\right)\right]$$
$$+ \frac{\widetilde{I}_N}{2}\, \partial_{Z_\mathbb{R}}^2\, W\left(Z_\mathbb{R}, Z_\mathbb{I}\right) + \frac{\widetilde{I}_N}{2}\, \partial_{Z_\mathbb{I}}^2\, W\left(Z_\mathbb{R}, Z_\mathbb{I}\right), \tag{IV.36}$$

for an arbitrary probability density W. It can be shown further that when the finite mean escape time exists, it obeys the equation:

$$\widehat{L}_{FP}^\dagger\, \tau_{esc}\left(Z_\mathbb{R}, Z_\mathbb{I}\right) = -1, \tag{IV.37}$$

where the adjoint operator to the Fokker-Planck operator is:

$$\widehat{L}_{FP}^\dagger\, W\left(Z_\mathbb{R}, Z_\mathbb{I}\right) = -f\left(Z_\mathbb{R}, Z_\mathbb{I}\right)\, \partial_{Z_\mathbb{R}} W\left(Z_\mathbb{R}, Z_\mathbb{I}\right) - g\left(Z_\mathbb{R}, Z_\mathbb{I}\right)\, \partial_{Z_\mathbb{I}} W\left(Z_\mathbb{R}, Z_\mathbb{I}\right)$$
$$+ \frac{\widetilde{I}_N}{2}\, \partial_{Z_\mathbb{R}}^2\, W\left(Z_\mathbb{R}, Z_\mathbb{I}\right) + \frac{\widetilde{I}_N}{2}\, \partial_{Z_\mathbb{I}}^2\, W\left(Z_\mathbb{R}, Z_\mathbb{I}\right). \tag{IV.38}$$

The solution $\tau_{esc}\left(Z_\mathbb{R}, Z_\mathbb{I}\right)$ then provides the mean time that it takes for the system to escape this region, if it starts its motion at the point $Z_\mathbb{R}, Z_\mathbb{I}$ [Pistolesi *et al.* 2008].

Applying our different sets of experimental parameters to the Fokker-Planck equation, it is thus possible to produce theoretically what we should measure in our experiments, as far as the Langevin process is valid. One can verify that indeed within the experimental range explored, the relaxation probability is exponential versus time. It also enables to have theoretically access to the universal exponents and to the dependence of the bifurcation process on the non-linearity beyond the limit where the 1D theory breaks down, as was also investigated in Ref. [Kogan 2008].

IV.4   Experiment

IV.4.1   Motivations and experimental set-up

Investigating both ζ and ξ is challenging since Γ has a logarithmic precision over Γ_0. Extracting the different power scaling laws requires thus accurate measurements of the average escape time $t_{esc} = \dfrac{1}{\Gamma_{esc}}$.

As described in Chap. II, we first need a low temperature environment to prevent noise on the measured signal, but also to "freeze" intrinsic materials dynamics as much as possible. Experiments show that if the set-up warms up to liquid nitrogen temperature (typically above 50 K), previous measurements will not be perfectly compatible with the new ones even though the NEMS is cooled down again to Helium temperatures. This mismatch is due to all sorts of non-reproducible thermally-activated alterations of the NEMS, like the exact atomic configuration due to dilation/compression or the intrinsic two-level systems (TLS) dynamics (see Sec. IV.4.3 and Chap. V). While the parameters of the oscillator shift at worse by a few percents, the exponential dependencies on E_a in Γ_{esc} [Eq. (IV.2)] and Γ_{esc} in P [Eq. (IV.1)] make the experiment sensitive to such small deviations. Nevertheless, only the NEMS' parameters are expected to change with temperature while the general behaviour of the bifurcation process should not be affected. To confirm the reproducibility of the phenomenon we did two thermal cycles above 50 K, leading to three different sets of data. For clarity, we will mainly focus on one of them and compare with the others only when necessary.

One of the main objectives of this experiment is to understand the behaviour of the bifurcation phenomenon as a function of the non-linearity generating the bistable regime (Chap. II). This regime, as presented earlier, depends on both the non-linear parameter γ and the displacement amplitude x through βx^2. In most experiments γ is of geometrical origin (hence fixed) and the non-linearity is induced by increasing the displacement. While this would be enough for an ideal Duffing oscillator, it is no longer true if extra non-linear terms exist (see Sec. II.3.5). Indeed, depending on the material, the geometry or the type of excitation, new non-linearities can emerge from the standard equation with terms like $\alpha_1 x \ddot{x}$ or $\alpha_2 x \ddot{x}$, and even anelastic effects may appear (see Sec. II.5.4). Tuning the displacement might then affect those extra terms and completely change the physics studied. Furthermore, the dependence on x in the activation energy E_a does not reduce to the standard Duffing term βx^2, see Eq. (IV.32). As a result, tuning *independently* the non-linear coefficient and the displacement amplitude is required for a better understanding of the relaxation process since β and x are not interchangeable quantities.

In our case we use an intrinsicaly highly linear resonator: the goalpost presented in Chap. II, which geometrical non-linearity is almost inexistent even for large displacements. By means of a D.C. gate voltage (Sec. II.3.4), we tune in-situ the Duffing non-linear parameter such that $\gamma \propto -V_g{}^2$ [Eq. (II.15)]. Note that our γ is

hence negative unlike most NEMS' Duffing coefficients which are usually positive. The polarity is irrelevant as far as the formulae quoted in Sec. IV.3.1 are concerned (they involve absolute values of β).

This distinctive tunability feature enables to control the non-linearity at a fixed displacement amplitude, but one first needs to take into account side effects of this capacitive coupling, i.e. the contribution of the other orders in the Taylor expansion [Eq. (II.13)]. In the D.C. range we are going to explore (up to 10 V), the gate voltage will also shift the resonance frequency ω_0 as described in Eq. (II.22). For clarity, in the whole chapter ω_0 will always refer to the resonance frequency shifted by the applied D.C. gate voltage (written $\omega_{0,g}$ in Sec. II.4.3).

The principle of the experiment is to detect transitions from a metastable state to a stable one for different NEMS' parameters. By doing so we will tune both the activation energy and the attempt frequency, which will change the escape time by orders of magnitude. Controlling the noise level I_N we can catch up this modification to keep overall measurement times in a convenient range. This control can be achieved by changing the temperature or using a noise source generator. Since the effective temperatures involved in the bifurcation process for our NEMS' parameters are of the order of 10^4 K, the latter option is clearly more appropriate.
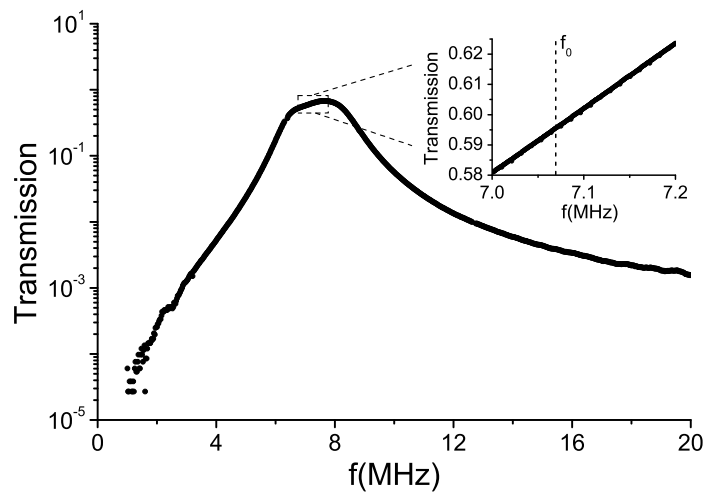
Figure IV.8: Normalised response of the passive filter in log scale. The inset highlights the flatness around the resonance frequency ω_0. The loss factor due to the filter is about 1.65.

Through the magnetomotive set-up described in Chap. II, a voltage noise source generator added to the actual harmonic drive is used to produce the noise force acting on the NEMS (Fig. II.13). In practice, we used the second channel of our Tektronix generator which has a noise function (white, Gaussian, distributed from D.C. to 240 MHz). Since we do not want to warm up the sample, we reduce its frequency range using a passive filter with a bandwith of 1 MHz around 7 MHz.

The characteristics of this filter is presented in Fig. IV.8. We then use the active adder presented in Chap. II to combine the harmonic drive with the noise voltage. As pointed out in Ref. [Aldridge & Cleland 2005], it is rather delicate to appreciate the exact amplitude of the noise experienced by the NEMS. We took extreme care in its calibration, measuring the noise spectrum at room temperature with a spectrum analyser on both the input signal (after the adder) and on the Ohmic voltage (at the level of the lock-in detector). Nevertheless, this parameter is certainly the less accurately known in absolute units (arguably up to $\pm 20\,\%$ here), and we shall comment this point at the end of the Chapter.

To detect the metastable/stable state transitions, as described in Sec. IV.3, we need to be close to one of the two bifurcation points of the Duffing oscillator (Fig. IV.9). The relaxation occurs either close to the linear resonance frequency ω_0, from the small amplitude state (metastable) to the large one (stable) at the frequency $\omega_{bif\uparrow}$, or close to the maximum displacement's frequency $\omega_0 + \beta x^2$, from the large amplitude state (metastable) to the small one (stable) at the frequency $\omega_{bif\downarrow}$. The latest is the most experimentally studied one and the most theoretically described, thus the biggest part of our experiment is done close to $\omega_{bif\downarrow}$.
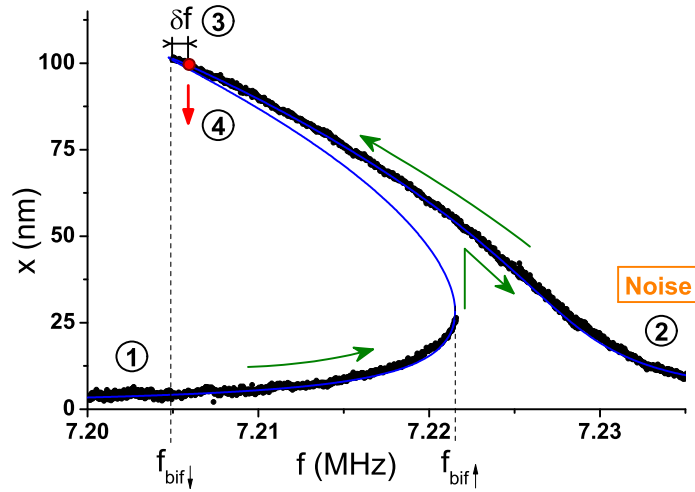
Figure IV.9: Duffing response of the NEMS at $V_g = 9.4$ V. Two bifurcation points delimit the hysteresis: transition from the high to low amplitude at $f_{bif\downarrow}$ and the opposite at $f_{bif\uparrow}$. The blue line is a fit to the data. In the experimental scheme, we start from an arbitrary position ①, sweep upward through $f_{bif\uparrow}$ until ② and turn the noise on, sweep downward until the detuning δf is reached ③, wait for the NEMS to relax ④, and restart all over again.

The basic idea of the experiment is to measure the time needed for the NEMS to relax to its stable state for a given set of parameters. First of all, we need to initiate the NEMS in the metastable state in the upper branch. We fix our harmonic drive and apply a reasonable D.C. gate voltage to open the hysteresis up to the desired value. Since our non-linearity is negative, we sweep the frequency

upwards through the hysteresis, up to a few linewidths after the bifurcation point $\omega_{bif\uparrow}$. We then turn the noise on and we sweep backwards until reaching the desired detuning $\delta\omega = \omega - \omega_{bif}$ from the bifurcation point $\omega_{bif\downarrow}$.

One crucial parameter in this procedure is the rate at which the sweep is done. Indeed, sweeping too fast makes the system non-adiabatic and relaxes the NEMS to the low amplitude state before reaching $\delta\omega$. On the other hand, sweeping too slow leads to an undefined relaxation time. The first condition only matters when the driving frequency ω is close to the bifurcation point, thus we use two sweeping rates: we first sweep fast (typically hundreds to kHz/sec), and as we get closer to $\omega_{bif\downarrow}$ we reduce the rate (typically few Hz/sec) until reaching the right detuning. Those two rates change with the size of the hysteresis defined by the applied voltage V_g, as it will be described in Sec. IV.4.3. Thanks to the exponential dependence of the escape time to the detuning parameter, the time needed to park at $\delta\omega$ essentially does not affect the measurements.

When the NEMS is properly initiated at a fixed driving force, noise I_N, detuning $\delta\omega$ and non-linear Duffing coefficient γ, we measure the relaxation time to switch from the high amplitude branch to the low one, and start over again the measurement procedure. Since the phenomenon is of statistical origin, the most straightforward way of analysing the relaxation times is by creating histograms. A large amount of data is needed to have a consistent histogram, we thus have measured about a thousand relaxations for each set of parameters.
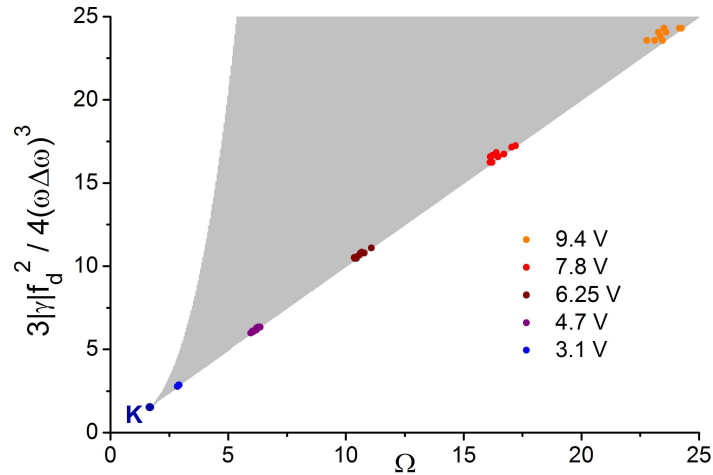
Figure IV.10: Bifurcation parameter space (normalised non-linearity as a function of normalised frequency, as defined in Sec. IV.3.1). The grey area is the bistability regime of the NEMS where the right edge is the transition from a high amplitude oscillation to a low one at $\omega_{bif\downarrow}$, (the left edge is the opposite, at $\omega_{bif\uparrow}$) and K is the spinode point where hysteresis starts to open. We show within the bistability the data points at different voltages V_g.

For our sets of parameters, the force is fixed to 65 pN, leading to a displacement amplitude of about 100 nm, which is the reasonable limit before deviations on the Taylor expansion of the capacitance (Sec. II.3.4). At this displacement, no distortion of the Lorentzian resonance curve due to intrinsic non-linearities can be seen, and the hysteresis only starts to open for an applied D.C. gate voltage of about 2.1 V, which is called the spinode point K in Fig. IV.10. To explore a wide range of the bifurcation parameter space we used five different non-linearities, from small hysteresis (3.1 V) to hysteresis of about ten linewidths (9.4 V) as seen in Fig. IV.10. For each non-linearity we measured at least three detunings, from tens of Hz at the smallest hysteresis, up to hundreds of Hz for the largest. In order to extract with a good accuracy E_a and Γ in $P(t)$, we measured three different noises for each of these $\delta\omega$ and γ, leading to average escape times t_{esc} from about 0.5 to 50 sec.

The main interest in this experiment is to investigate both the region were the analytical results apply and what happens beyond this limit. As described by Eq. (IV.24), this limit depends on the working point ω with respect to the frequency position at which the NEMS reaches its maximal amplitude ω_{max} (Fig. IV.7). If the driving frequency ω is in between ω_{bif} and ω_{max} then the analytical calculations apply. Beyond ω_{max}, no present analytical prediction exists, although some numerical calculation was done in the case where the driving amplitude was the sweeping parameter [Ryvkine *et al.* 2004, Kogan 2008]. While the injected noise needed to bifurcate beyond ω_{max} seems quite high for small hysteresis, this is no longer true for large non-linearities, and for $V_g = 6.25$ V we can already overcome the limit. In total, we explored a range such that $0.13 < 4\,\Omega_{bif}\,|\Omega - \Omega_{bif}| < 71$. Let us note that we also measured the relaxation times at $\omega_{bif\uparrow}$ from the small amplitude branch to the large one, and at $\omega_{bif\downarrow}$ but reducing the maximal displacement amplitude by a factor $\sqrt{2}$ and 2. While those extra-configurations could not be studied in the framework of the bifurcation process itself, their implications for our results will be discussed in the next sections.

IV.4.2   Measurements and analysis techniques

The measurement of the relaxation time starts right after $\delta\omega$ is reached and ends when the measured oscillation amplitude passes below a threshold value, arbitrarily fixed to half of the maximum amplitude. When enough relaxation times have been recorded for each set of data (a thousand typically takes about a day), a pre-analysis is done to prevent experimental artefacts to be kept in the final histograms.

Indeed, a few undesired features have to be removed from the analysis:

- From an instrumental point of view, it is important to note that the GPIB acquisition process takes about 40 ms to measure one point, which means we cannot measure too short escape times. It is also important to check that this acquisition time does not vary too much within one histogram (because of computer's extra processes), in order to guarantee the acquisition stability in terms of sweep rate.
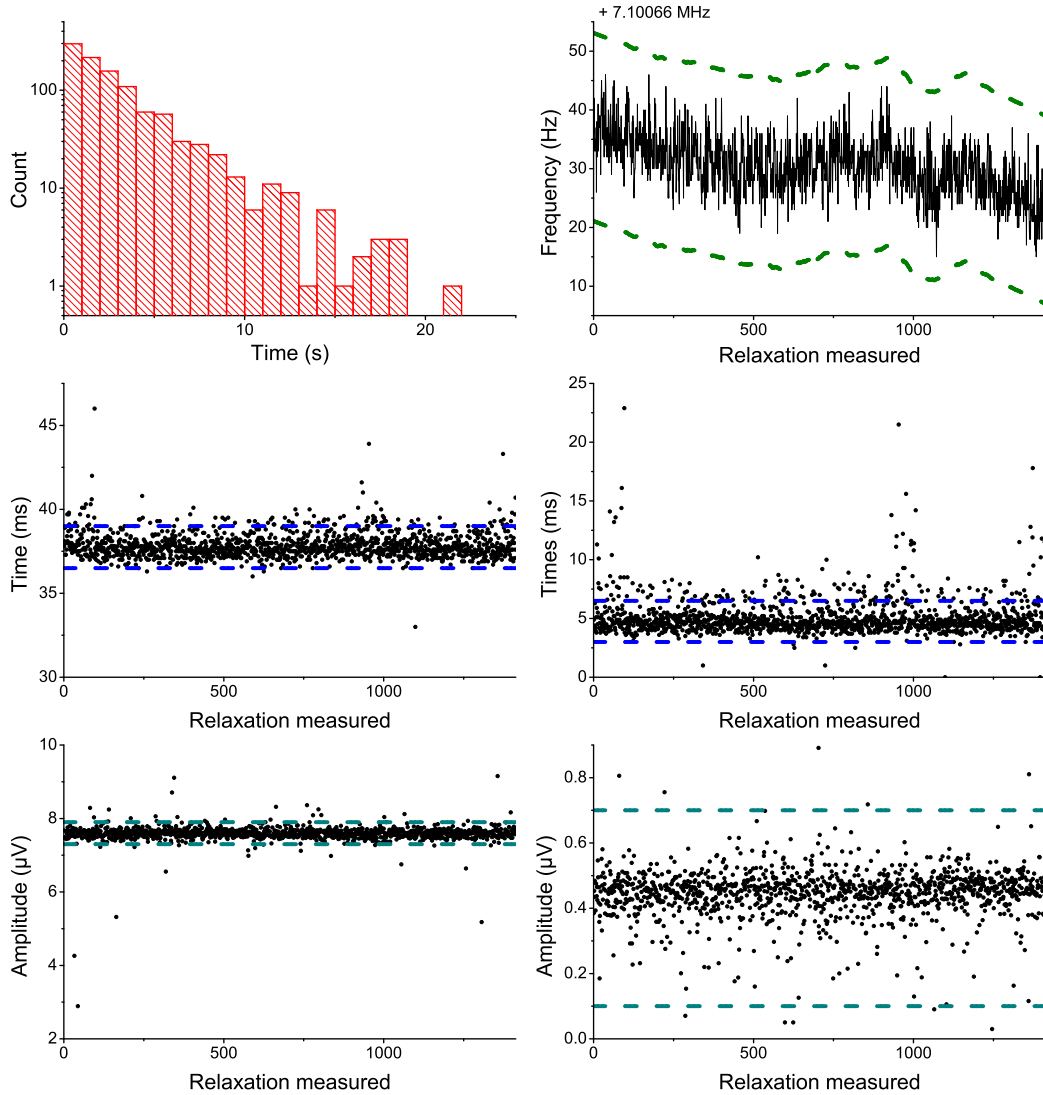
Figure IV.11: Typical output of the Python routine (here $V_g = 4.7$ V, $\delta f = 100$ Hz, $I_N = 32$ fN^2/Hz), presenting the results of the pre-analysis as described in the text. The dashed lines are the analysis thresholds detailed below. *Top left*: histogram of the relaxations after analysis. *Top right*: shift in frequency as the relaxations occur. Any too large shift in frequency (typically five standard deviations) is removed from the analysis (dashed line). Here, none occured as opposed to Fig. IV.14. *Center Left*: averaged measurement time between each data point. If the measurement time is shorter or faster for one relaxation, we remove it. *Center right*: standard deviation of measurement time for each relaxation. If the measurement time fluctuates too much, we also remove the point. *Bottom left*: averaged jump amplitude of the relaxation for the in-phase component. This jump represents the amplitude difference between the high and the low state, and should remain the same for a fixed set of parameters. *Bottom right*: standard deviation of the amplitude before relaxation. If the amplitude fluctuates too much before the relaxation occurs, we remove the point as well.

- The amplitude of the jumps from one branch to the other is also carefully measured to check that the NEMS is stable during the whole acquisition at the desired working point.

- As described above, the materials of the NEMS may have defects inducing additional features such as *two level systems* (TLS), which change the resonance frequency of the NEMS and thus the working point $\delta\omega$. Tracking ω_{bif} is hence of crucial importance in order to exactly know the detuning at which the relaxation takes place. Fortunately, the activation of single and large TLS is a rare (and probabilistic) event, but each time it permanently shifts ω_{bif} until it kicks back in after an unknown amount of time (Fig. IV.14). By measuring the bifurcation frequency without injected noise before each relaxation time acquisition, we can recover these rare global shifts. However, since we do not know whether the TLS was activated during the measurement of ω_{bif} or during the previous escape time measurement, both data points are excluded from the final analysis. The overall measured bifurcation frequency displays also a slow random drift which can be attributed e.g. to the thermal stability of the room (typically about 10°C). Note that, as presented in Fig. IV.11 (top right), a small low frequency noise remains which shall be described in Sec. IV.4.3.

- To finish with, the relaxation time measurement has two cutoffs: a minimum value of about 40 ms due to the GPIB and a maximum value of about 40 sec. Some relaxations might occur before 40 ms, but we observe that their contribution is negligible compared to the total number of relaxations. These data points are disregarded as being "early" switchings. However, the number of relaxations after 40 sec might be quite large depending on the set of parameters. While we obviously cannot determine the histogram of those relaxations, we can know the total amount of relaxations that were not measured. This is required for a proper normalisation of the relaxation histograms. Note that $\frac{1}{\Delta\omega} < 40$ ms, hence the relaxation occurs within one amplitude point measurement and we automatically satisfy the condition of being resolving only the slow variable evolution [Eq. (IV.23)].

Those different experimental issues were taken care of using a Python written routine, and a typical result of this pre-analysis is presented in Fig. IV.11.

From those relaxation times left after filtering, we compute histograms from which we can obtain the average escape time t_{esc} (Fig. IV.12). Plotting them as a function of the noise intensity I_N with an exponential law [Eq. (IV.32a)], we should be able to extract both activation energy and attempt frequency, and finally their detunings and non-linear dependencies. Nevertheless, only few histograms are as good-looking as the ones in Fig. IV.12: when the detuning is too small a "curved" histogram is obtained, even in log-scale (Fig. IV.13).

Fitting an exponential does not seem to be appropriate, something is missing either in the theory or in the analysis. From the "curved" behaviour of the histogram,
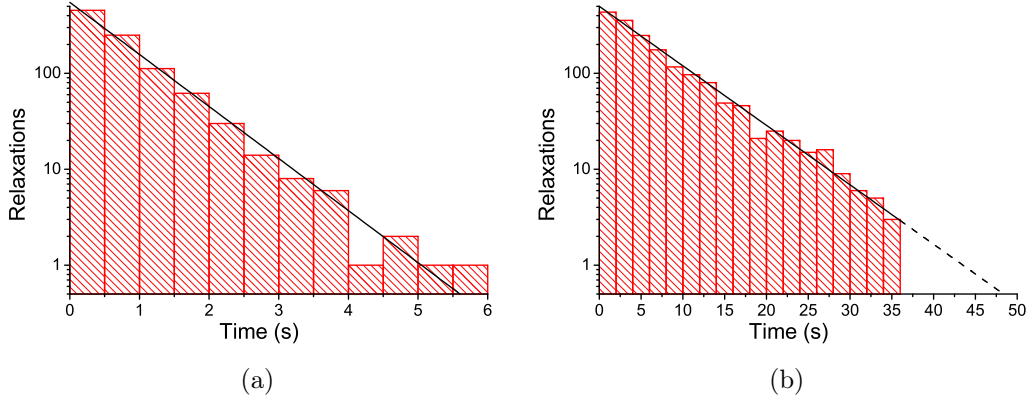
Figure IV.12: Typical histograms at large detuning. The figures a) and b) differ by the set of parameters used (respectively $V_g = 9.4$ V, $\delta f = 400$ Hz, $I_N = 10$ fN^2/Hz and $V_g = 6.25$ V, $\delta f = 170$ Hz, $I_N = 15.7$ fN^2/Hz), leading to different escape times. The black lines are exponential fits. In b) case, the histogram is cut at the end due to the measurement procedure as explained above (dashed line). However, we know the total number of relaxations that should be present in the histogram, and hence the fitting procedure does not have any free parameter except from the average relaxation time.
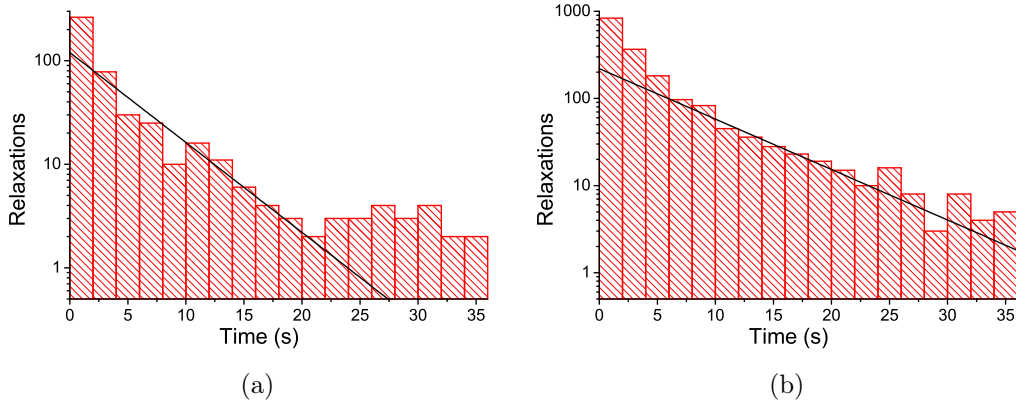
Figure IV.13: Unusual histograms at small detuning (a: $V_g = 7.8$ V, $\delta f = 30$ Hz, $I_N = 0.32$ fN^2/Hz, b: $V_g = 4.7$ V, $\delta f = 30$ Hz, $I_N = 5.1$ fN^2/Hz). Note the curved aspect compared to Fig. IV.12. The lines are just guides for the eyes.

one can deduce that a parameter is not fixed during a single set of measurements, leading to a *dynamical* average of the relaxation times.

Regarding stability, the bifurcation process is indeed extremely demanding due to the exponential/power law dependencies. The key is in the frequency stability, the requirements are less stringent on the other parameters. The question is what could experimentally limit our precision. As a matter of fact, it appears that the biggest uncertainties seem to come from the NEMS itself with the remaining low-frequency fluctuation of ω_{bif} (see Fig. IV.11, top right). Indeed, in a standard measurement
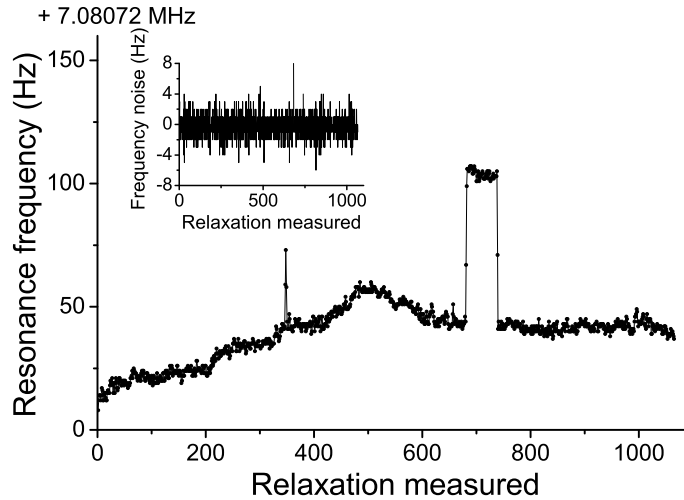
Figure IV.14: Bifurcation frequency shift as a function of the relaxation number during the same set of parameters ($V_g = 3.1$ V, $\delta f = 30$ Hz, $I_N = 25.9$ fN^2/Hz). Each relaxation takes about 2 minutes. Three different fluctuations are observed: the rare large frequency jump, the slow fluctuation during the day and the faster fluctuation making f_{bif} non-reproducible between each relaxation measurement. Inset: "fast" frequency fluctuation extracted after filtering the slow one and the jumps.

the resonance frequency of an oscillator is known within its linewidth. With the bifurcation process, this precision is highly improved [Aldridge & Cleland 2005].

As described above, for each relaxation time measured, we look for the actual bifurcation frequency. It hence takes about two minutes to acquire one relaxation time, since we need to be careful about the sweeping procedure. Plotting the time ordered measured ω_{bif}, we show the evolution of two bifurcation frequency sets during the day in Fig. IV.11 (top right) and Fig. IV.14. Three major features emerge from these graphs as already pointed out: a very slow drift of the resonance frequency over the day, the presence of large frequency jumps, and a slow but faster fluctuation around the (local) mean.

While important, the global drift over the day is recovered by the bifurcation frequency tracking method since the fluctuation is over tens of relaxation records. However the large frequency jumps represent rare TLS events, which are well-known to affect measurements in mechanical resonators. Over the months of acquisition, we observed a general behaviour emerging from this characteristic feature. Among the parameters we control for the bifurcation process, only the gate electrode and the drive amplitude are relevant for this specific study, the noise power I_N being negligible compared to the energy released during the relaxation process itself (the noise generator is always off). As one could suspect from TLS, most of the "up" jumps are followed with "down" jumps of the same amplitude (as presented in Fig. IV.14), with an effective "life time" of the activated TLS which varies from the minimum measurement time (about one minute) to hours.

We show in Fig. IV.15 the dependency of the amplitude of these jumps. While
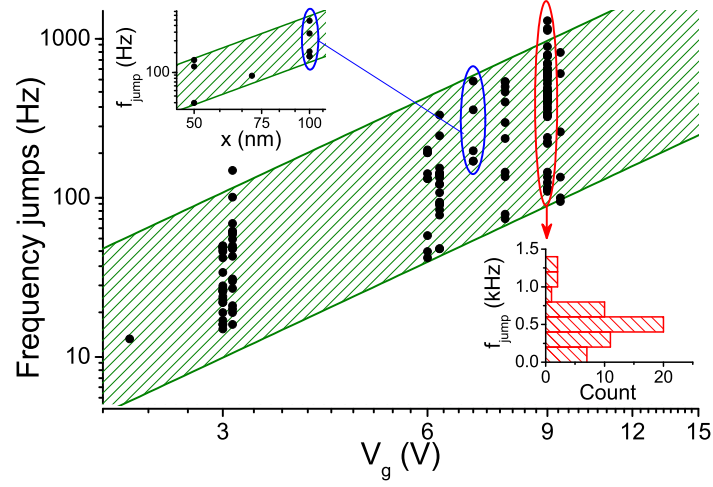
Figure IV.15: *Main*: frequency jump amplitudes as a function of the applied voltage V_g on the gate electrode for $x = 100$ nm. The green surface is a guide for the eyes, delimited by a quadratic dependency on both sides. Note that the data from three different cryo-cycles are all present in this graph. *Top inset*: jump amplitudes as a function of the displacement amplitude x for $V_g = 7$ V. The blue surface follows the same definition as in the main graph. *Bottom inset*: histogram of the jump sizes for $V_g = 9$ V, which is similar for the other voltages.
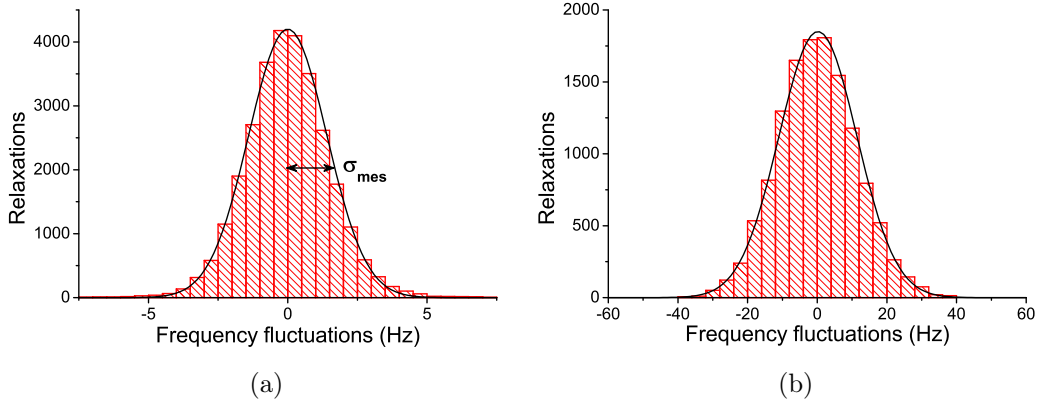
Figure IV.16: Example of histograms characterizing the zero-averaged frequency fluctuations of the bifurcation point. The black lines are Gaussian fit. a) Histogram obtained at $V_g = 3.1$ V, for a velocity of 1 Hz/sec, with a mean standard deviation of $\sigma_{mes} = 1.4$ Hz. b) Histogram obtained at $V_g = 9.4$ V, for a velocity of 5 Hz/sec, with a mean standard deviation of $\sigma_{mes} = 11.2$ Hz.

the data are scattered, we see in this log-log plot an overall square tendency of the amplitude as a function of both the gate electrode applied voltage V_g and the NEMS displacement x, which seems to be reproducible over cryo-cycles. Unfortunately, the probability of measuring a TLS being very small (in our case we see on average 1 TLS every 10^3 relaxations), the amount of measured jumps is not enough to extract

more information (like the correlation between jumps or between their size and time duration before return). But as far as bifurcation is concerned, it is fortunate that those experimental issues are rare events: we can easily take their effect into account in the analysis to study solely the bifurcation process.

However, after filtering the slow fluctuation process and the TLS jumps, we still see a (small) noise on ω_{bif} between each measurements (inset of Fig. IV.14). Creating a histogram out of this "faster" fluctuation data, we see that this noise is Gaussian with a standard deviation σ of a few Hertz for small hysteresis up to around ten Hertz for the largest one (Fig. IV.16). This means that, while we drive the NEMS at a fixed frequency ω, the bifurcation frequency ω_{bif} of the NEMS itself is fluctuating. Each relaxation time measurement is hence performed with an uncertainty on the detuning $\delta\omega$ of up to 15%, which is dramatic since t_{esc} depends both exponentially and in power laws on $\delta\omega$, and leads to a dynamical t_{esc} that explains the curved histograms we measured.

In order to analyse the bifurcation process with high precision we thus need to characterise and understand these frequency fluctuations, and then take them into account.

IV.4.3   The Gaussian distribution of the resonance frequency

A proper characterisation of the noise generating σ is not a trivial task. Indeed, the method used by sweeping through ω_{bif} with no injected noise is just a first indicator if one needs to extract and characterise the frequency noise out of it. The first matter one would need to take care of is to determine whether this noise is low or high frequency - that is if within one relaxation time measurement the bifurcation frequency shifts. To resolve the frequency of the noise, we need our measurement technique to be faster than this noise. Nevertheless, even by just sweeping through the bifurcation point over and over (which takes each time about a minute), we cannot measure ω_{bif} fast enough.

However, assuming the frequency of the noise is too high would mean that the relaxation times measurement at a detuning $\delta\omega$ close to σ is impossible: the NEMS would almost instantly relax because the actual driving frequency would have a high probability to be out of the hysteresis (that is for our case $\omega < \omega_{bif}$). But Fig. IV.17 clearly shows a reasonable average escape time while $|\delta\omega| < \sigma$ for no injected noise. From this result we can deduce that the frequency noise is too fast to be properly defined but still slow enough so that we can measure t_{esc} in a meaningful way.

Another important issue is to be able to measure the real σ: indeed the measured sigma σ_{mes} is different from the actual one we want to characterise. This comes from both the sweeping rate and the bifurcation process itself. If we sweep too slowly we might relax before ω_{bif} because of a bifurcation process occurring in the meantime (even for no injected noise, the system still has some intrinsic noise). Thus sweeping at a high rate seems the appropriate method to obtain almost instantly the bifurcation frequency, but again the bifurcation process might make the NEMS relax before ω_{bif} due to the high energy and non-adiabaticity involved in a fast
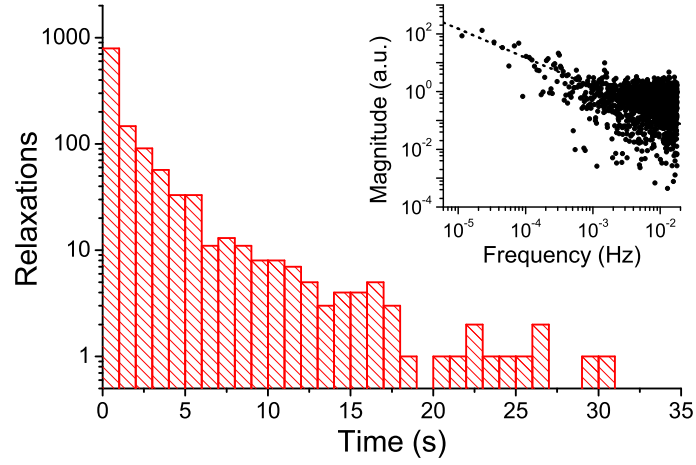
Figure IV.17: *Main*: Relaxation histogram without injected noise I_N for $\delta f = 2$ Hz at $V_g = 3$ V (with a Gaussian frequency fluctuation of $\sigma_\infty = 3$ Hz as defined in the following). Since the detuning is small, the histogram is curved, but we can clearly measure long escape times while the measurement is done within σ_∞. *Inset*: typical Fourier transform of the autocorrelation of the frequency noise. Note the $1/f$ fitted law in dashed line.

sweep. The most reasonable way is hence to measure σ_{mes} at different sweeping rates, not too slow and not too fast, and then to extrapolate to σ_∞ what would be the fluctuations in an ideal adiabatic *but* ultra-fast sweep (Fig. IV.18).
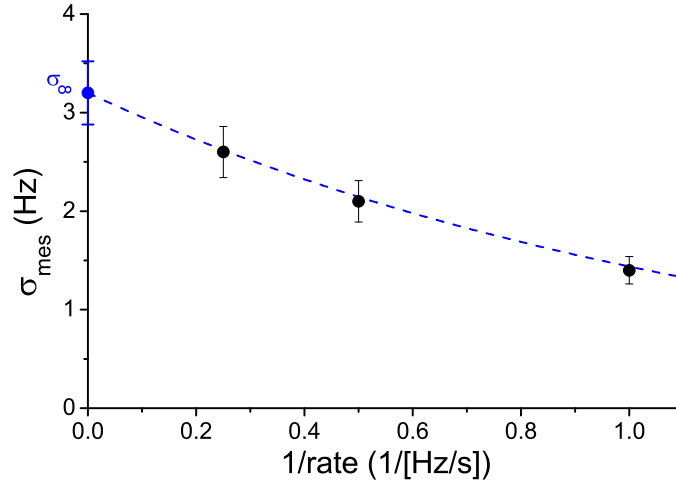
Figure IV.18: Typical example of the extrapolation of σ_∞ at infinite rate (note the inverse x-axis), for $V_g = 3.1$ V. The blue line is a guide for the eyes. This extrapolation keeps σ_∞ within the same order of magnitude than σ_{mes} (variation up to a factor of 2).

Doing this extrapolation for different gate electrode voltages V_g and different

NEMS amplitudes, we observe a quadratic dependence of the fluctuations on both parameters, as presented in Fig. IV.19, which seems to be robust even after different cryo-cycles. One could suspect that this frequency noise comes from the bifurcation phenomenon itself (ramping through ω_{bif} with a small but non-zero intrinsic noise remaining at ω_0 [Aldridge & Cleland 2005]). We show in dark cyan in the inset of Fig. IV.19 a fluctuation measurement taken on the other edge of the hysteresis at $f_{bif\uparrow}$, where the energies E_a involved scale in a completely different way from the bifurcation at $f_{bif\downarrow}$ [Dykman & Krivoglaz 1979, Kogan 2008]. We see however that the σ still scales with the same quadratic law with respect to motion amplitude. Thus it cannot be linked to scatter due to the bifurcation process, and fluctuations have to be genuinely coming from the resonance frequency itself.

From these analyses, we can phenomenologically construct a biquadratic equation that captures the dependencies of the fluctuations:

$$\sigma_\infty = \sigma_0 + \Sigma_1 V_g^2 + \Sigma_1' x^2 + \Sigma_2 V_g^2 x^2, \tag{IV.39}$$

with σ_0 the intrinsic fluctuation of the resonance frequency and Σ_1 (in Hz.V^{-2}), Σ_1' (in Hz.nm^{-2}) and Σ_2 (in Hz.V^{-2}.nm^{-2}) the prefactors describing the effect of the gate electrode and the displacement of the NEMS.

From the quadratic fits in Fig. IV.19 we extract $\sigma_0 + \Sigma_1' x^2 = 1 \pm 0.2$ Hz and $\Sigma_1 + \Sigma_2 x^2 = 0.2 \pm 0.03$ Hz.V^{-2}, and incorporating these results in the fits of the inset which depend on x, we find the general equation:

$$\begin{aligned}
\sigma_\infty = &(1 \pm 0.2) + (0.037 \pm 0.01) V_g^2 \\
&+ (0 \pm 0.5) \times 10^{-4} x^2 + (0.163 \pm 0.02) \times 10^{-4} V_g^2 x^2. \tag{IV.40}
\end{aligned}$$

We thus see three components inducing those small fluctuations in the resonance frequency: an intrinsic term σ_0 which presumably is due to the distribution of the "faster" TLS, the contribution of an electrostatic term $\Sigma_1 V_g^2$ and a mechanical energy-like contribution scaling with x^2. On one hand, the electrostatic term could be attributed to the imprecision of our voltage generator (error $\frac{\delta V}{V}$ of the order of 10^{-6} while the resonance frequency mainly shifts as $1770\ V_g^2$, see Sec. II.4.3). On the other hand, no experimental limitation that we know of could explain a $\Sigma_2 V_g^2 x^2$ component, which origin can only be speculated. We could suspect that it might be the signature of a coupling between the mechanical energy of the mode and low-energy TLS [Fong *et al.* 2012]. For instance, we can propose that TLS can be statically biased by the voltage term $\Sigma_1 V_g^2$, and also mechanically activated with a released energy (or more accurately power) $\propto x^2$. The variation with $\Sigma_2 V_g^2$ would then be interpreted as a voltage-dependence in the TLS-energy coupling term.

While we cannot be sure of this "fast" frequency-noise origin, let us note that we also saw it in *intrinsically* non-linear NEMS without any voltage bias. Measuring in the same way as described before, this other device (the 15 μm low stress SiN doubly-clamped beam, resonating at 7 MHz like the goalpost) shows an intrinsic frequency fluctuation which is represented by the purple star in Fig. IV.19. Remarkably, the
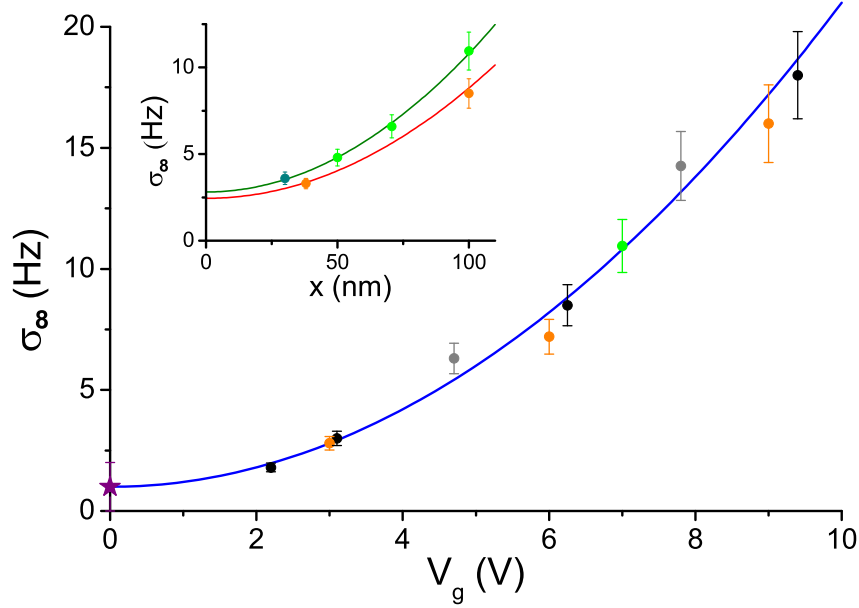
Figure IV.19: *Main*: variation of the bifurcation frequency fluctuation with respect to the applied voltage V_g. We present in black and grey the fluctuations measured for the set of data introduced in Fig. IV.10 (the grey ones being estimations from the extrapolation of the black ones), and in orange and green the two other sets of data after different cryo-cycles. However, all points were taken for a displacement x of 100 nm. Note the purple star which is the extrapolated σ of the low stress SiN doubly-clamped beam (zero voltage, same resonance frequency and extrapolated at zero motion to $\sigma_0 = 1 \pm 1$ Hz). The blue curve is a quadratic fit, as explained in the text. *Inset*: variation of the fluctuation with respect to the goalpost NEMS displacement. The colors respect the cryo-cycles defined in the main graph. The green data are at $V_g = 7$ V while the orange are at $V_g = 6$ V. Note the dark cyan lowest displacement point, which belongs to the same set of data as the green points, but was taken at the other bifurcation frequency $f_{bif\uparrow}$. Again, the curves are quadratic fits as explained in the text.

values of σ_0 for both goalpost and low stress doubly-clamped beam are almost equal. However, for the SiN device, the parameter Σ_1' appears to be clearly non-zero. The reason is unknown, but one could speculate that the coupling strength between TLS and mechanical energy depends on the stored stress in the structure.

To finish with, two high stress SiN doubly-clamped beams (resonating at 14 MHz for the 15 μm long and 21 MHz for the 10 μm long) also show intrinsic "fast" fluctuations of respectively 3 Hz and 15 Hz, which increases with the frequency rather than with the resonator's volume. These intrinsic fluctuations are hence present whatever the geometry/material and grow with f_0.
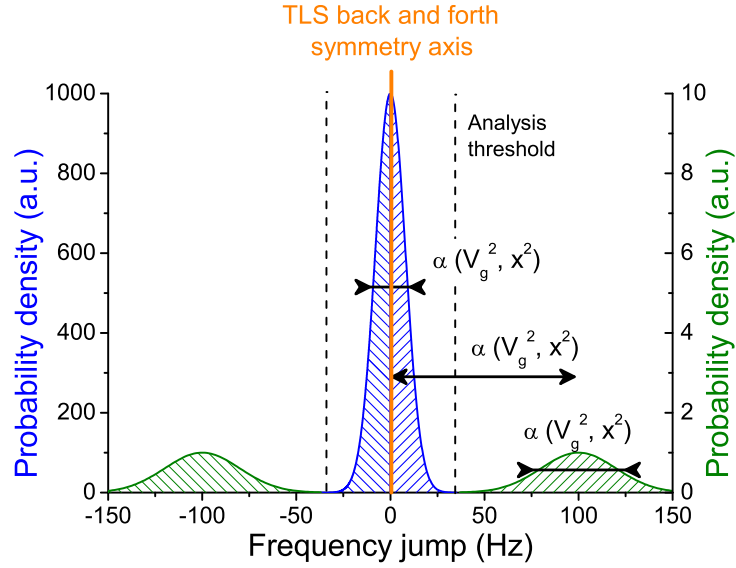
Figure IV.20: Schematic overview of the TLS signatures measured in our goalpost device, from Fig. IV.15 and Fig. IV.19 (here for $V_g = 6.25$ V and $x = 100$ nm). The "faster" but "smaller" frequency jumps probability density, which standard deviation increases as V_g^2 and x^2, is represented in blue (left axis). The "slower" but "larger" frequency jumps probability density is represented in green, which averaged value and width at half maximum increase with both V_g^2 and x^2 (right axis). The dashed lines are the Python routine thresholds, as described in the text. Note that in the TLS model the two levels are symmetric in energy, hence their repercussion on f_0 is symmetric in sign: to a positive jump necessarily corresponds a negative one of same amplitude.

If we now synthesise our understanding on the observed TLS, we list two kinds of frequency jumps after filtering the slow drift over the day: the "faster" but "smaller" ones and the "slower" but "larger" ones (Fig. IV.20). Note that in the analysis procedure, the Python routine considers any jump larger than 5 σ_{mes} as a "large" jump, which enables to clearly distinguish the two kinds of TLS. In the case of the "faster" jumps, we see a zero-centred Gaussian distribution which linewidth increases with both the applied gate voltage V_g^2 and the NEMS displacement x^2. For the "slower" jumps we also notice a peaked distribution (histogram inset of Fig. IV.15) which seems to broaden as V_g^2 and x^2 as well, but the amount of data we have is not enough to determine the distribution function. However, the average value of the large jumps is *non-zero* and increases with V_g^2 and x^2. This surprising result is counter-intuitive from the TLS model, which considers a zero-centred distribution uniformly spread. We can interpret our findings as a polarization effect on a portion of the intrinsic TLS of our device, dividing them from the "mother" distribution which remains centred. However, we would obviously need more data to construct a physical concept out of this large jumps which could explain these features, and the bifurcation scheme seems to be a good and accurate tool for measuring them.

IV.4.4   Implementing the frequency fluctuation issue

Now that the Gaussian frequency noise is characterised, we need to integrate it in the analysing method of the bifurcation phenomenon. For clarity, we now replace σ_∞ by σ. Since $\frac{\sigma}{\omega_{bif}} < 10^{-5}$ but $1\% < \frac{\sigma}{\delta\omega} < 15\%$, at first approximation the frequency noise only affects the detuning. Because the distribution is Gaussian, we can then write:

$$P_{exp}\left(t\right) = \frac{\int_{-\delta\omega}^{\infty} e^{-\frac{\varepsilon^2}{2\sigma^2}}\, \Gamma_{esc}\left(\delta\omega + \varepsilon\right)\, e^{-\Gamma_{esc}\left(\delta\omega+\varepsilon\right)t}\, d\varepsilon}{\int_{-\delta\omega}^{\infty} e^{-\frac{\varepsilon^2}{2\sigma^2}}\, d\varepsilon}, \tag{IV.41}$$

with ε the continuous frequency noise fluctuation. We integrate over the noisy detuning $\delta\omega + \varepsilon$ assuming it is fixed within one measurement. For $\delta\omega + \varepsilon < 0$ the NEMS relaxes before the timer starts because of a non-bifurcation process, this case is hence analytically removed from the integration and is experimentally already accounted for in the Python pre-analysis through the 40 ms cut-off.

(a)   (b)

(c)   (d)
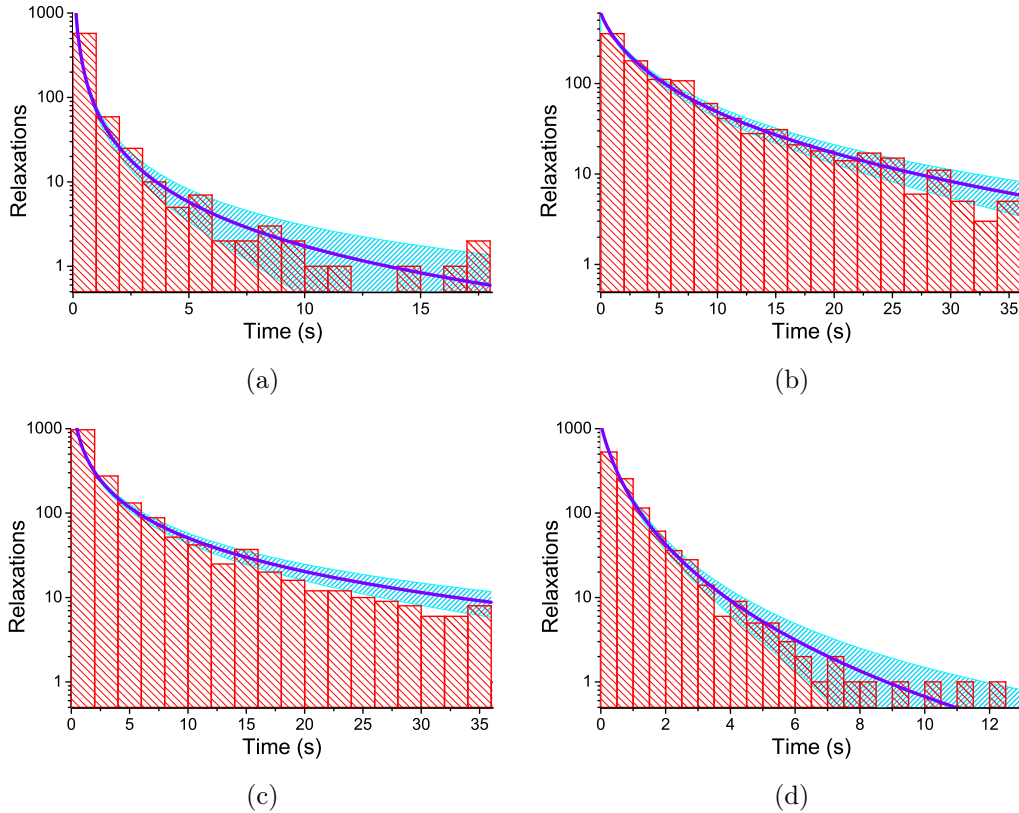
Figure IV.21: Histograms at small detunings for different non-linearities (a: $V_g = 7.8$ V, $\delta f = 30$ Hz, $I_N = 0.8$ fN^2/Hz, b: $V_g = 7.8$ V, $\delta f = 100$ Hz, $I_N = 2.5$ fN^2/Hz, c: $V_g = 6.25$ V, $\delta f = 30$ Hz, $I_N = 1.3$ fN^2/Hz, d: $V_g = 4.7$ V, $\delta f = 30$ Hz, $I_N = 8$ fN^2/Hz). The blue lines are fits according to Eq. (IV.41), which recovers the curved aspect of the histograms within the statistical error bar $\sqrt{N}$ (in dashed blue).

Unfortunately, Eq. (IV.41) is not solvable analytically and one needs to integrate numerically for each set of parameters to fit the histograms. However we see in Fig. IV.21 that we can now recover the curved histogram shape using the experimentally defined σ and still fit the straight ones.

One last important point to note about the frequency noise implementation in the fitting procedure is that there is always a non-zero probability to relax because of fluctuations of f_0 occurring *during* an escape time measurement: while we stay parked, a (large) frequency fluctuation can still eventually bring the system below the bifurcation point. In this case, the event should be removed from the analysis since it does not come from the physics of the bifurcation process, but is only due to the frequency-noise. While we cannot determine when those events occur, we can try to estimate their average probability. If we note P_{TLS} the probability for the NEMS to relax due to the frequency-noise, then the overall probability to relax in a measurement is:

$$P_{tot} = P_{bif} + (1 - P_{bif})P_{TLS}. \tag{IV.42}$$

This probability P_{TLS} can be approximated from the "stopping time theory" in statistics. The idea is to split the process in time steps t_ε (separated by Δt) during which the frequency can jump in discrete steps δ_ε. During the time interval, we need to know the average number of (discrete) frequency jumps $\Delta N = f_\varepsilon \, \Delta t$ (at frequency f_ε) that occurred and the probability $p\,(\delta_\varepsilon)$ of jumping below the frequency threshold $\delta\omega$. The result is a Pascal law:

$$P_{TLS}\,(t_\varepsilon) = [1 - p\,(\delta_\varepsilon)]^{n(t_\varepsilon)} \; p\,(\delta_\varepsilon)\,, \tag{IV.43}$$

with $n\,(t_\varepsilon) = t_\varepsilon \, f_\varepsilon$ the number of attempts to jump. Assuming we can take the problem to the continuous limit ($\Delta t \to 0$, which is *not* a trivial assumption) we write:

$$P_{TLS}\,(t) = p\,(\delta_\varepsilon) \; e^{-f_\varepsilon \, ln\,[1 - p\,(\delta_\varepsilon)]\,t}, \tag{IV.44}$$

f_ε being here the "attempt frequency" for the noise process. For our Gaussian distributed noise with $1/f$ spectrum, we can estimate p and f_ε by introducing cutoffs (ω_{low} and ω_{high}, defined by the experimental procedure) in the noise spectrum of amplitude A:

$$S_{TLS}\,(\omega) = \frac{A}{\omega}. \tag{IV.45}$$

We then have the standard deviation σ and the "attempt frequency" ω_ε of the frequency noise (both in Rad.s^{-1}), with the induced probability of jumping $p\,(\delta_\varepsilon)$

defined as:

$$\sigma^2 = \frac{1}{2\,\pi} \int S_{TLS}\left(\omega\right) d\omega = \frac{A}{2\,\pi}\,\log\left(\frac{\omega_{high}}{\omega_{low}}\right), \tag{IV.46}$$

$$\omega_\varepsilon = \frac{\int S_{TLS}\left(\omega\right)\omega\,d\omega}{\int S_{TLS}\left(\omega\right) d\omega} = \frac{\omega_{high}-\omega_{low}}{\log\left(\dfrac{\omega_{high}}{\omega_{low}}\right)}, \tag{IV.47}$$

$$p\left(\delta_\varepsilon\right) = 1 - \frac{\displaystyle\int_{-\delta\omega+\delta_\varepsilon}^{+\infty} e^{-\frac{\varepsilon^2}{2\,\sigma^2}}\,d\varepsilon}{\displaystyle\int_{-\infty}^{+\infty} e^{-\frac{\varepsilon^2}{2\,\sigma^2}}\,d\varepsilon}. \tag{IV.48}$$

If we now measure a relaxation histogram with no noise injected (hence no bifurcation process enabled), the relaxations shall be due solely to the frequency noise process described here. We were able to obtain decent average relaxation times of that sort, and we could fit these histograms to the continuous Pascal law [Eq. (IV.44)], as presented in Fig. IV.22.
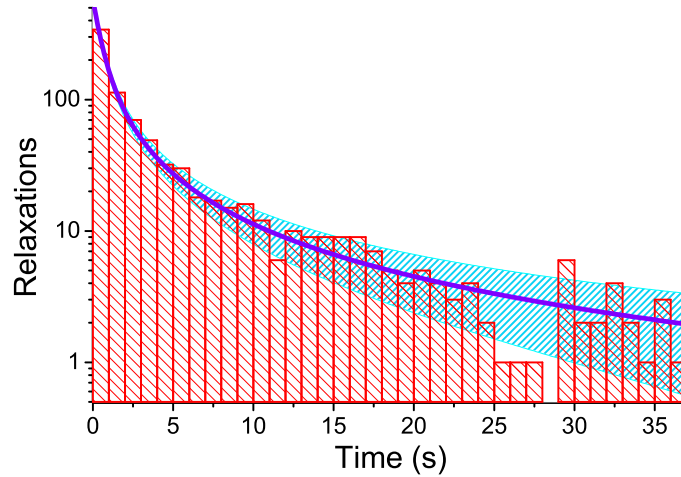
Figure IV.22: Histogram of relaxations due to the Gaussian frequency-noise with no injected noise I_N ($V_g = 9.4$ V and $\delta f = 30$ Hz). The line is a fit using the Pascal law, with the standard $\sqrt{N}$ error bar displayed (dashes).

Note that this kind of histogram (with no injected noise) can only be measured very close to the bifurcation point, far from the detunings at which we characterised the bifurcation process. Injecting in Eq. (IV.42) the Pascal law, we could calculate the impact of P_{TLS} on our results with the actual detunings we used for the bifurcation measurements, and found that the fluctuation contribution in the number of relaxations is only of a few events over the thousands we measure for each set of parameters. Clearly, the present modeling is far too simplistic to be quantitative, but this conclusion should be robust. This demonstrates that in our experiments relaxing because ω_{bif} might cross the driving frequency should not be relevant compared

to the bifurcation process itself. As a first approximation, we can hence remove this feature from the analysis and declare that the frequency noise mostly affects the uncertainty of $\delta\omega$ between each relaxation time measurement.

The frequency noise thus seems to be the main reason for the curved histogram, but since the fit is done numerically through the bifurcation equation itself, we cannot extract directly activation energy, attempt frequency, and detuning dependencies one after the other like in Ref. [Stambaugh & Chan 2006]: all the histograms need to be fit at once with one set of fitting parameters. All together, it is a 4 parameters fit (E_0, Γ_0, ζ and ξ) on about 9 histograms for each non-linearity. Thanks to the different scale dependencies, the uncertainty on each parameter should remain acceptable, but any extra parameter already present in the analysis alters the extraction of the fitting parameters. We shall thus be extremely careful in the numerical techniques used for the actual data fitting.

IV.4.5 Fitting procedure and results

The histogram is a graphic way of analysing large statistical data to give tendencies of a phenomenon. When it comes to have a complex quantitative fit, the bin size becomes a non-trivial parameter. Many different laws predict how one should tune the size of a bin as a function of the number of events and their distribution in the histogram. Since the statistical error on the number of events N in one bin is $\sqrt{N}$, with a bin of 10 events we already have more than 30% of uncertainty. In our case, those bins are mostly on the tail of curvature which contains a lot of information for the fitting procedure. For such a highly demanding experiment, we cannot afford extra-adjustable parameters which can change the values of the fitting parameters. We hence fit our data through another analysing method: integrating over the relaxations left to occur, the inverse of a so-called S-curve.

This procedure, essentially studied by Vadim Puller and Fabio Pistolesi, enabled to prevent the bin size issue. But their work also enabled to analyse the data with more rigour. Indeed, using Eq. (IV.41) to fit our results already assumes that Γ_{esc} depends on the detuning $\delta\omega$ with a power scaling law, while this is part of what we would like to find out. For $\delta\omega \gg \sigma$, one can expand the escape exponential distribution: $\Gamma_{esc}(\delta\omega + \varepsilon) = \Gamma_{esc} + \varepsilon\,\Gamma'_{esc}$. This gives the following distribution for the escape times:

$$P_{KS}(t) = \Gamma_{esc}\, e^{-\Gamma_{esc}\, t} \int \frac{e^{-\frac{\varepsilon^2}{2\sigma^2}}}{\sqrt{2\pi\sigma^2}}\, e^{-\varepsilon\,\Gamma'_{esc}\, t}\, d\varepsilon\,. \tag{IV.49}$$

From this equation, no assumption was made regarding the detuning dependency in Γ_{esc}. Furthermore, only two parameters are extracted from this fit: Γ_{esc} and the product $\Gamma'_{esc}\,\sigma$. Fitting Eq. (IV.49) to the data using the method of Kolmogorov-Smirnov [Eadie *et al.* 1971] and letting σ as a free parameter (see Fig. IV.23), our theoretical partners found the same behaviour for the frequency fluctuation and could extract t_{esc} as a function of the injected noise I_N (Fig. IV.24).
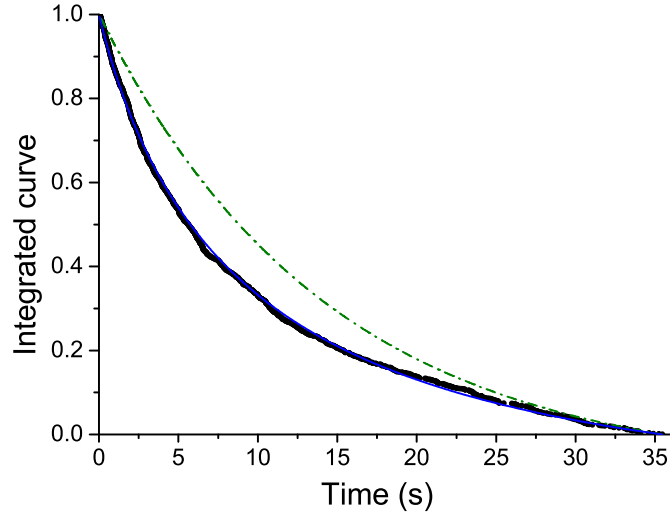
Figure IV.23: Normalised inverse integration of the relaxations through the escape time. The black points are the data, the dashed green line is an attempted fit without fluctuations on $\omega_{bif\downarrow}$ while the blue line takes σ into account as presented in Eq. (IV.49).
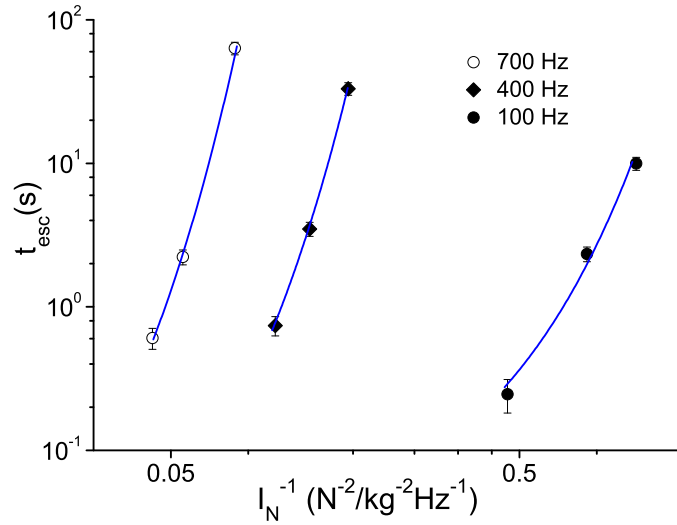
Figure IV.24: Average escape times for the set of parameters at $V_g = 9.4$ V in log-log scale. The X axis is also in log scale for display, due to the orders of magnitude in noise intensity between each detuning. The blue lines are exponential fits while the black points are data at different detunings, as specified in the legend.

The only drawback is that Eq. (IV.49) is only an approximation: for too large σ with respect to $\delta\omega$ this fitting procedure cannot be used, which removes 4 detunings out of the 15 that we initially measured.

From the fitted average escape times, we can extract attempt frequencies Γ and activation energies E_a as a function of the detuning $\delta\omega$ and the non-linear Duffing coefficient γ. Let us recall that the range we explore in the bifurcation

(a)

(b)
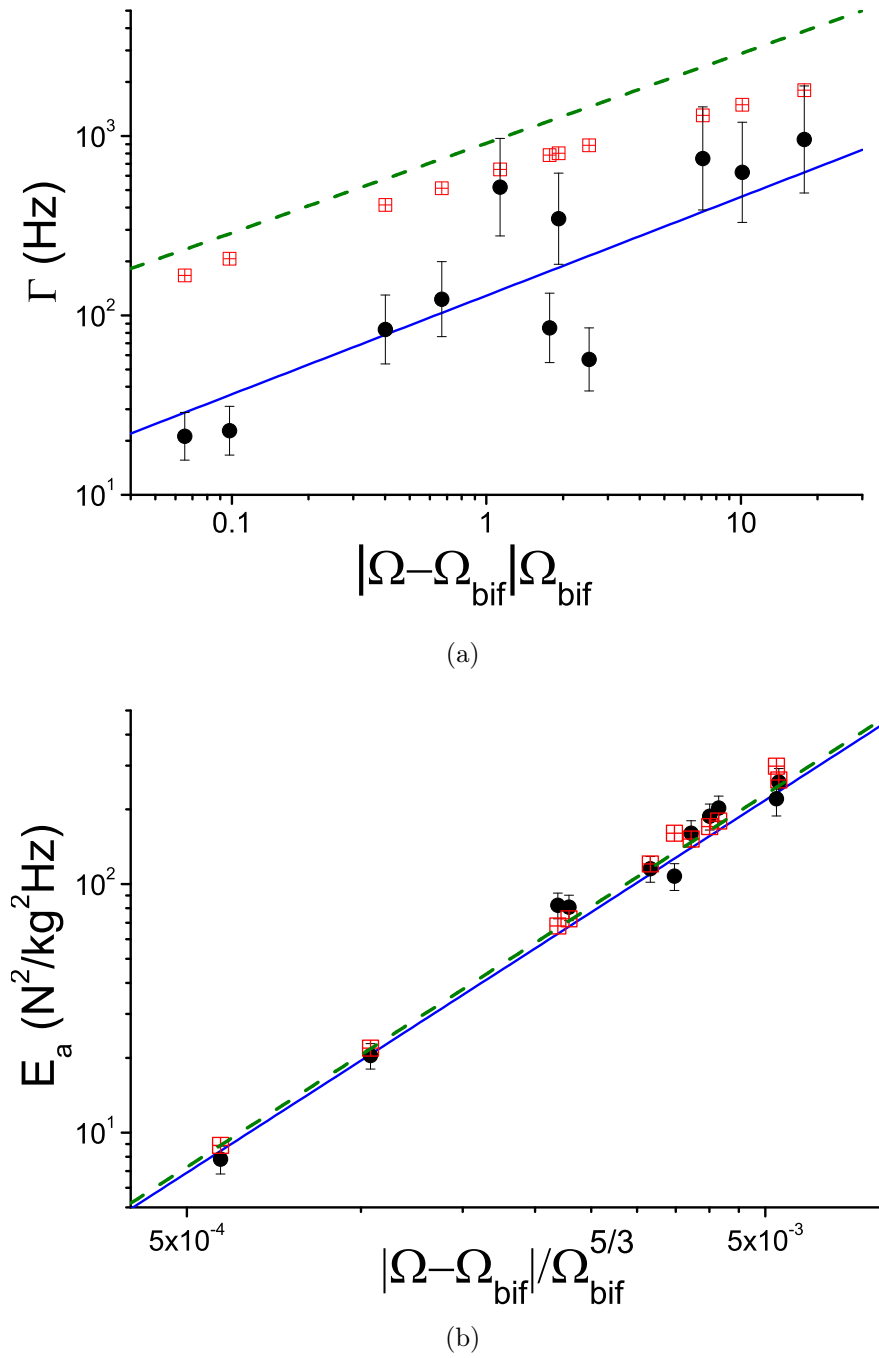
Figure IV.25: Attempt frequency Γ (a) and energy barrier E_a (b) dependencies as a function of the normalised detuning in log scales. The black circles represent the experimental data, the red squares show the numerical results of the Fokker-Planck equation, the dashed green line is the analytical result. The blue line is the fit on the data, with a slope of 0.55 ± 0.2 for Γ and 1.53 ± 0.04 for E_a.
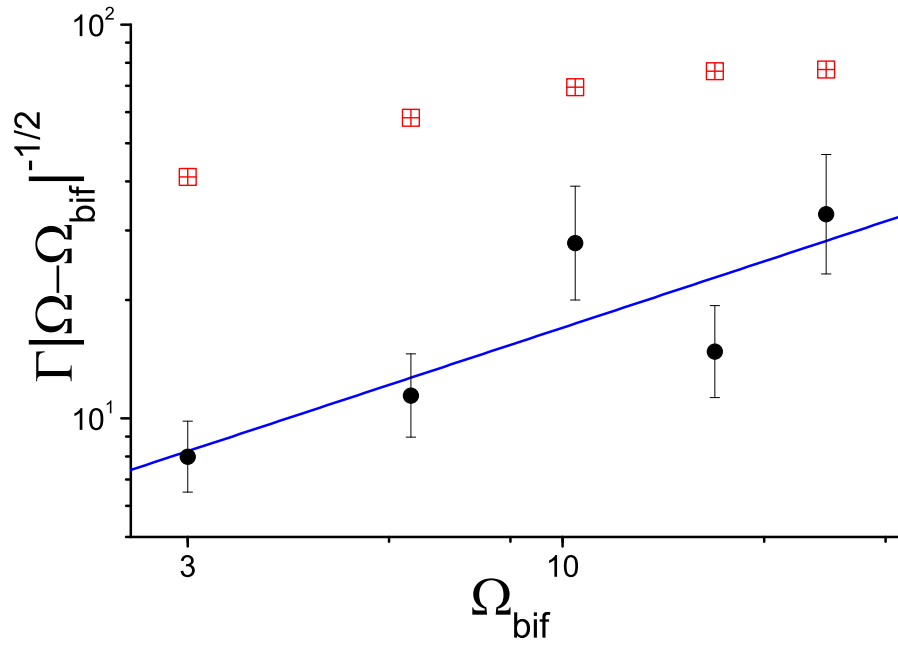
(a)
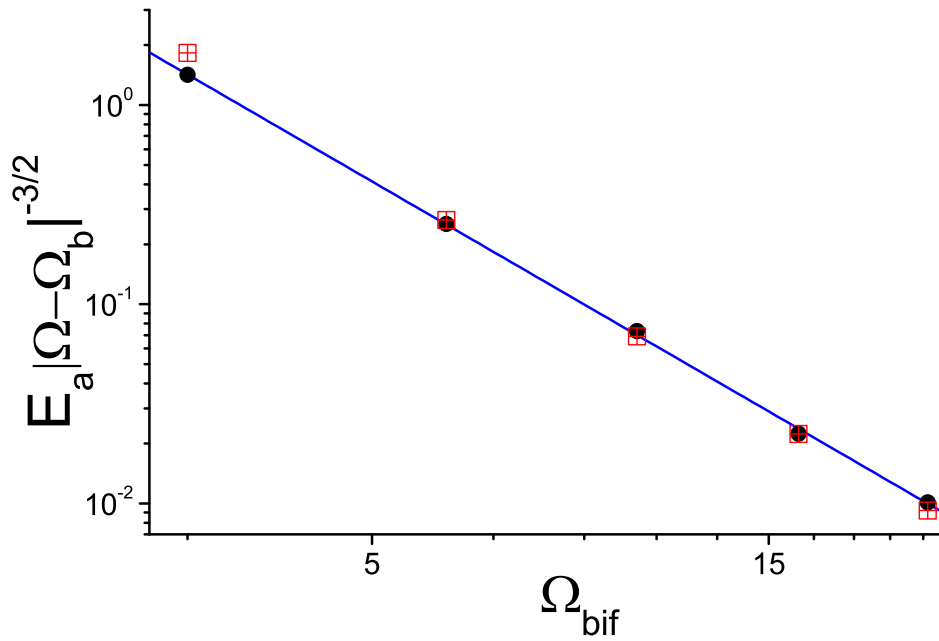
(b)

Figure IV.26: Normalised non-linearity dependencies for both attempt frequency and activation energy. The definitions follow the one in Fig. IV.25. The slope of the blue fits are $+0.6\pm0.1$ for Γ and -2.43 ± 0.05 for E_a.

process starts within the analytical solutions, about an order of magnitude before the approximation breaks down, and ends far beyond the validity of this regime, by about 2 orders of magnitude.

If we incorporate all data points taken at different non-linearities in a single plot for both Γ and E_a, we can see the general tendency of the bifurcation process with respect to the detuning (Fig. IV.25). The precision is clearly better for E_a than for Γ, due to the logarithmic sensitivity in Eq. (IV.3), and leads to large error bars for Γ. While this might affect the uncertainty we have on a single point for Γ, the overall tendencies can be extracted with a decent precision. A remarkable scaling is observed in all the experimental range, with a fitted power law of 0.55±0.2 for the attempt frequency and 1.53±0.04 for the activation energy as a function of detuning, which have to be compared to $\zeta = 0.5$ and $\xi = 1.5$ from Eq. (IV.3). As for the non-linear parameter (Fig. IV.26), we see respectively power laws of 0.6±0.1 and -2.43±0.05, which have to be compared respectively to 0.5 and -2.5 [Eq. (IV.32c)], which have never been reported to our knowledge.

In parallel to this fitting procedure and as described in Sec. IV.3, our collaborators could simulate the bifurcation phenomenon using exact 2D numerical calculations based on the Fokker-Planck equation. Implementing the exact same set of parameters we did experimentally, they could numerically obtain average relaxation rates directly from the general equation Eq. (IV.37). Comparing those numerical results to the measured data (Fig. IV.25 and Fig. IV.26), we observe for both E_a and Γ the same general behaviour, validating the whole analysis.

For the attempt frequency, we found Γ within a factor of 4 which is nonetheless remarkable considering the logarithmic precision, and no other measurement of this kind has been published to our knowledge. However, the numerical results also indicate that the exact scaling is expected to be slightly different from the analytical one. Indeed, it seems the behaviour of Γ cannot be described exactly by a simple scaling law at large detunings/non-linearities (Fig. IV.25a and Fig. IV.26a). Nevertheless the experimental precision is not high enough to probe this deviation. Moreover, changing the way of extracting Γ and E_a seems to slightly alter the tendencies: it is not really clear if this deviation in Γ comes from the actual bifurcation process or from the analysing method. The factor of 4 mismatch between theory and experiments could thus be due to the fit procedure, but no conclusive explanation could be obtained.

As far as activation energy is concerned, the scaling power laws are undistinguishable between numerical and experimental data. The quantitative match is also very good: the experimentally defined noise calibration factor has been renormalised by 15 % only in amplitude in order to match theory and experiment, all other parameters being known within a sufficient precision. Such an agreement is a large improvement on bifurcation phenomenon experimental results.

Those unprecedented results are the first attempts to measure the universal power law ζ of Γ and to investigate the general behaviour of the saddle-node bifur-

cation process as a function of its intrinsic fundamental parameter, the non-linear Duffing coefficient γ. Furthermore, the graphs in Fig. IV.25 and Fig. IV.26 demonstrate that all those scalings predicted in the analytical theory hold far beyond its validity. Hence the range where the universal scaling laws apply is much larger than the one restricted by the analytical approximations, as numerically predicted for force sweeps [Kogan 2008].

IV.5   Conclusion

The work presented here demonstrates the robustness of the universal power laws in the saddle-node bifurcation phenomenon. After an overview of the 1D analytical theory of the bifurcation process, we investigated the universal scalings of the activation energy E_a and the attempt frequency Γ as a function of the detuning from the bifurcation point and we described their non-linear dependencies. Furthermore, we delimited the region of applicability of this analytical theory, which decreases as the non-linearity increases to the extent that experimental measurements might be well outside this region. We presented an introduction of the simulations done by our collaborators to numerically understand the behaviour of the system beyond the analytical limit.

We finally present the experiment and the first results on the measurement of the average escape time t_{esc}, which cannot be described with the analytic theoretical background of the bifurcation process. By analysing in details the experimental evolution of the bifurcation frequency $\omega_{bif\downarrow}$, we observe a small "fast" fluctuation which affects the detuning $\delta\omega$ for each relaxation measurement. After a thorough study of this Gaussian $1/f$ noise affecting f_0 we managed to take it into account in the analysing procedure and to consistently describe the differences observed in the measurements between small and large detunings with respect to the bifurcation point. This extensive characterisation of the frequency noise is unique to our knowledge, while recent works focus on this issue [Fong *et al.* 2012].

Plotting the results as a function of both detuning and non-linearity, we could extract power laws in very good agreement with the 1D theory in the whole experimental range while most of those data where beyond the analytical limit. The numerical simulations corroborate our results within a rescaling of 15 % on the noise calibration and we have about a factor of 4 discrepancy on the attempt frequency (i.e. 20 % on the logarithm of Γ) [Defoort *et al.* 2014b]. This is remarkable, given the dificulty in calibrating the injected noise and the logarithmic sensitivity on Γ. The present study is the most quantitative one that we are aware of in the literature (see e.g. Refs. [Chan & Stambaugh 2007, Aldridge & Cleland 2005]). The scalings of the bifurcation phenomenon are thus still valid about two orders of magnitude beyond the analytical results, which is a remarkable and unexpected fact. Indeed, in the case of parametrically induced bifurcation (the so-called *pitchfork*), the scalings have been experimentally demonstrated to change as they get away from the bifurcation point. At the moment we write these lines, we do not know if this result if a property of the Duffing oscillator, or if it has a deeper origin within all saddle-node bifurcation phenomena.

IV.6 Perspectives

While the range of parameters studied in the present chapter explores the bifurcation process beyond the analytical 1D limit, an investigation of this phenomenon at even larger detunings might bring new physics. Indeed the power law dependencies for both E_a and Γ eventually change far enough from the bifurcation point [Ryvkine *et al.* 2004, Kogan 2008].

There are also three preliminary sets of data that we used for the frequency fluctuation characterization from which we could still get some information, and which would require further measurements:

- We measured for $V_g = 7$ V three different maximum displacement amplitudes, namely 100 nm, 71 nm and 50 nm. We described theoretically in Eq. (IV.32b) how the bifurcation process should be affected by the displacement amplitude, this kind of data would enable to test this dependency.

- The reverse bifurcation process (at $\omega_{bif\uparrow}$ instead of $\omega_{bif\downarrow}$) has been investigating at $V_g = 6.25$ V for three different detunings. Our collaborators started to work on it and found that the behaviour seems indeed to scale differently than the presented study. A more complete analysis of the other bifurcation point might thus reveal new interesting features.

- We performed the relaxation process over two cryo-cycles, between which the NEMS parameters slightly drifted. Using Eq. (IV.41), we found a good qualitative agreement with the activation energy and the attempt frequency power law dependencies of the presented cryo-cycle, but the same analysing method (i.e. with the Kolmogorov-Smirnov technique) should be done on those other data too. This would give an idea of the reproducibility of the phenomenon even though the NEMS parameters changed. Furthermore, we performed the same experiment on a standard doubly-clamped beam (on which the non-linearity cannot be tuned) to verify qualitatively that our findings are indeed robust. Again, a full analysis would be required. More experiments could be performed on different types of nano-devices as well to reinforce the statistics.

This experiment shows how the bifurcation process is sensitive to its environment. It is also clear that theoretical results are robust, even more than the analytical model in the 1D limit seemed to claim in the first place. On the other hand, two level systems in constitutive materials are of big interest for many physical systems. Both the "fast" frequency noise and the rare large frequency jumps were probed with a good precision in this experiment, while this investigation was not the aim of the study and the set-up not designed for it. If this noise has been an issue for the comprehension and the analysis of the relaxation process, using now a bifurcation set-up *as a tool* to better understand the physics describing these TLS might be a very promising method.

IV.7   Résumé

Le phénomène de bifurcation suscite un intérêt général en Science, de part son large domaine d'applications et des questions fondamentales qu'il pose. Le concept de bifurcation émerge des systèmes bistables comportant une hystéresis, présent dans de nombreuses disciplines (Fig. IV.1) et qui a été introduit dans le cadre des NEMS au travers du Chap. II. La non-linéarité de notre système est au cœur de cette bistabilité, ce qui en fait un paramètre essentiel dans l'étude de la bifurcation.

D'un point de vue théorique, le phénomène de bifurcation peut se ramener à un double puits de potentiel asymétrique avec un point métastable séparé par une barrière de potentiel E_a du point stable (Fig. IV.2). Lorsque cette barrière disparait, l'état métastable devient instable et seul l'état de plus basse énergie devient stable, cette limite s'appelle le point de bifurcation. Dans le cas où la barrière de potentiel est présente, l'étude de la relaxation du système de l'état métastable vers l'état stable est régit par une loi de type Arrhénius, avec un taux d'échappement Γ_{esc}. L'énergie d'activation nécessaire E_a pour cette relaxation, introduite par Kramers, ainsi que sa fréquence d'essai Γ, ont été particulièrement étudié dans les travaux théorique de Mark Dykman. Ces deux paramètres, décrivant l'ensemble du phénomène de bifurcation, dépendraient de la distance au point de bifurcation en loi de puissance [Eq. (IV.3)] quelque soit le phénomène de bifurcation étudié: il s'agirait d'une description universelle.

Expérimentalement, les NEMS ont souvent été un outil de choix pour l'étude de ce phénomène. La bistabilité est définie par l'amplitude de vibration du NEMS dans le régime non-linéaire: dans le régime de Duffing, à une fréquence donnée, le NEMS peut osciller avec une forte ou une faible amplitude pour une même fréquence d'excitation (Fig. II.33). Initialisé à une distance $\delta\omega$ du point de bifurcation ω_{bif} et en présence de bruit I_N, le système a alors une probabilité non-nulle de bifurquer d'un état à l'autre. Ce phénomène, de nature probabiliste, est régit par la loi de Poisson et la distribution des temps de relaxation est alors exponentielle. En réitérant le processus de relaxation et à travers l'histogramme des temps de relaxation, on obtient alors le temps moyen de relaxation pour une configuration donnée, directement lié au taux d'échappement Γ_{esc}. Dans le cas de nombreux travaux, seule la loi de puissance dans l'énergie d'activation E_a a fait l'objet d'une étude qualitative, démontrant la justesse des prédictions théoriques. Cependant, plusieurs aspects n'ont jamais été testé, comme la fréquence d'essai Γ, une comparaison quantitative entre la théorie et l'expérience, la dépendance à la non-linéarité du phénomène de bifurcation ou encore la zone de validité des formules universelles proposée par Mark Dykman. Ce sont principalement ces quatre aspects qui on été étudiés en détails dans ce chapitre, avec une approche théorique (résultats analytiques), numérique (résolution de l'équation de Fokker-Planck) et expérimentale (à l'aide de notre NEMS en portique introduit Chap. II). Les résultats théoriques et numériques ont été obtenus avec la collaboration de Vadim Puller et Fabio Pistolesi, et ce sont principalement les résultats expérimentaux qui sont décris dans ce chapitre.

Un aspect essentiel de ce travail expérimental est de pouvoir contrôler un maximum de paramètres indépendamment les uns des autres. Entre autre, il est possible de contrôler l'amplitude de notre système x, le bruit injecté I_N, et la distance au point de bifurcation $\delta\omega$ à laquelle on souhaite faire relaxer notre résonateur. L'originalité de ce travail (et les résultats qui en découlent) sont principalement dûs à la possibilité de manipuler le paramètre non-linéaire β de notre système sans affecter l'amplitude de résonance de notre NEMS, mais en utilisant l'électrode de grille qui lui fait face. On peut alors, à une amplitude fixe, ajuster la taille de l'hystérésis et étudier l'évolution de la bifurcation pour différentes non-linéarités. Dans le cadre de ce travail et afin de satisfaire tous nos objectifs, nous avons exploré une large gamme de non-linéarités afin d'observer le comportement de la bifurcation, du régime où la théorie universelle s'applique jusqu'au régime où aucune prédiction analytique n'a été suggérée à ce jour (Fig. IV.10). L'objet de cette étude étant de nature probabiliste, une procédure systématique doit alors être mise en place pour mesurer les taux d'échappements moyens pour une configuration voulue (Fig. IV.9). De même, l'analyse systématique des données doit être en mesure de pouvoir faire le tri entre les résultats physiques et les erreurs dues aux aléas expérimentaux (Fig. IV.11). Cependant les premiers résultats d'expériences présentent des histogrammes inhabituellement courbés (non-exponentiels, voir Fig. IV.13), empêchant l'extraction du taux d'échappement Γ_{esc}.

Une étude approfondie sur la fréquence de bifurcation ω_{bif} révèle que la distance expérimentale au point de bifurcation $\delta\omega$ elle-même présente des fluctuations (Fig. IV.14). Loin d'être un simple problème de dispositif expérimental, cette incertitude témoigne de la richesse du système étudié: ce bruit en fréquence provient de systèmes à deux niveaux (TLS) présents au sein du matériaux de nos NEMS. Grâce à la précision du processus de bifurcation, il est alors possible avec ce dispositif expérimental d'étudier ces TLS (Fig. IV.15 et Fig. IV.19), domaine de recherche important entre autre dans la communauté des NEMS/MEMS, mais dont la nature reste un sujet à débat.

En étudiant cette fluctuation en fréquence, l'aspect "courbé" des histogrammes a pu être pris en compte et les taux d'échappements Γ_{esc} pour chaque configuration ont pu être extraits. En traçant la fréquence d'essai Γ et l'énergie d'activation E_a en fonction de la distance au point de bifurcation $\delta\omega$ et du paramètre de non-linéarité β du système, nous avons comparé nos résultats expérimentaux avec les résultats numériques (Fig. IV.25 et Fig. IV.26). Nous avons pu vérifié l'exactitude des lois de puissance prévu dans les développements analytiques du phénomène de bifurcation avec un accord entre théorie, résultats numériques et expérience de 15 % sur E_a et de 20 % sur le logarithme de Γ. Grâce à la large gamme de paramètres étudiés, nous avons aussi pu conclure que ces lois de puissance universelles sont valables dans une gamme bien plus importante que celle restreinte par les hypothèses analytiques [Defoort *et al.* 2014b].

NEMS as probes in condensed matter physics

Contents

V.1   Introduction

In the previous chapters we explored how NEMS can be used as model systems to investigate fundamental issues of (non-linear) physics. But just like MEMS, they also have a broad field of applications for both industries and research laboratories. They can be viewed as sensors, taking benefits from their small sizes for the next generation of nanotechnology tools impacting applied science or exploring new areas in fundamental physics. In this chapter, we focus on this aspect which is unavoidable when one is dealing with nano-resonators. While these two facets are rather distinct, the use of NEMS as model systems or probes are intimately related.

In a first section we demonstrate how the high-frequency dynamics of a NEMS can be used to detect a low frequency modulation. We develop an audio-mixing technique that imprints a low frequency signal into the high frequency resonance line, thanks to its non-linear coupling with a gate. After introducing the experimental set-up in which the mixing has been done, we present the theory explaining how satellite peaks emerge from the described coupling. We then expose our experimental results together with the calculations from the theory, reproducing without free parameters our findings. Finally, we describe the limit of applicability of the phenomenon for very low frequency signals both analytically and experimentally.

Using a different set-up configuration, we then present how NEMS can be used to study two-level systems (TLS) in disordered materials. In particular, we demonstrate that the state of the conductive electrons in the overlayer of the structure (normal or superconducting) impacts crucially the measured mechanical damping. We then discuss on the origin of this effect within the framework of the latest theories derived from the standard tunneling model of TLS.

To finish with, we implement a high aspect ratio doubly-clamped beam in a low pressure - yet not completely under vacuum - experiment. Measuring the broadening of the linewidth of two different NEMS, we investigate the properties of the boundary, the so-called Knudsen layer. After a brief state-of-the-art introduction, we expose our experimental set-up and how we performed our measurements. We describe analytically the different regimes the NEMS is sensing as the pressure in its cell is reduced, and demonstrate a good agreement with our data. We show that in the molecular limit, for a sufficiently large mean-free-path, a large deviation is seen between the standard bulk theory and experiment. We propose a phenomenological formula to describe our results and demonstrate that those measurements are qualitatively in agreement with the latest theory on the boundary layer.

V.2 The audio-mixing scheme

V.2.1 Experimental and theoretical basics

Signal mixing is a very useful technique in both applied and fundamental physics. In everyday life, radio sets are the perfect examples of the application of such a tool: they detect high frequency signals (typically 100 MHz) in which smaller frequency ones (typically 1 kHz) were previously imprint. After processing, only the audio-signal is sent to the speakers which then transduce it into air vibration, that is sound. In nanotechnologies, this scheme has already been implemented in a so-called "nano-radio" [Jensen *et al.* 2007, Vincent *et al.* 2011]. As a detection technique in more fundamental research, signal mixing also enables to measure very high resonance frequencies of nanotube devices [Witkamp *et al.* 2006].

In this section, we present experimentally and analytically how to mix a low frequency signal (of about 1 kHz) into a high frequency one (about 10 MHz) [Defoort *et al.* 2011], which is basically what is then detected by a radio set. Unlike most mixing techniques using NEMS, the set-up configuration used here enables to keep the resonance line of the structure in the linear non-Duffing regime, by using the coupling with the gate electrode presented in Chap. II. Driving the goalpost structure with small forces, around its resonance frequency ($\omega \approx \omega_{0,g}$ with $\omega_{0,g}$ the resonance frequency of the nano-resonator shifted by the gate, see Sec. II.4.3), and exciting the gate at a very low frequency $\omega_g \ll \omega_{0,g}$, the only relevant terms of the Taylor expansion in Sec. II.3.4 is the second derivative, such that we are left with the equation of motion:

$$\ddot{x} + \Delta\omega\,\dot{x} + \frac{k + \delta k\,(1 + \cos(2\,\omega_g\,t))}{m}\,x = \frac{F_L}{m}\,\cos(\omega\,t), \tag{V.1}$$

with $\delta k = \frac{1}{4}\,V_g^2\,\frac{\partial^2 C_g}{\partial x^2}$, V_g the A.C. gate voltage amplitude and we recall $\omega_{0,g} = \sqrt{\frac{k + \delta k}{m}}$. Eq. (V.1) is a modified version of a Mathieu equation, with an added dissipation and applied force. To find its stationary solution, we introduce an *ansatz* for the solution $x(t)$:

$$x(t) = \sum_{n=-\infty}^{+\infty} |X_n|\,\cos\left[\omega\,t + 2\,n\,\omega_g\,t + arg(X_n)\right], \tag{V.2}$$

where X_n are complex coefficients, n referring to the sum indentation (*not the mode number, we will only use the fundamental mode in this section*). Implementing Eq. (V.1) into Eq. (V.2), we obtain the following recurrence equation:

$$a_n X_n + X_{n+1} + X_{n-1} = 2\,\delta_{n,0}\,\frac{F_L}{\delta k}, \tag{V.3}$$

with:

$$a_n = 2\,\frac{\omega_{0,g}^2 - (\omega + 2\,n\,\omega_g)^2 - i\,(\omega + 2\,n\,\omega_g)\,\Delta\omega}{\omega_{0,g}^2}\,\frac{k + \delta k}{\delta k}, \tag{V.4}$$

and $\delta_{i,j}$ is the Kronecker's symbol.

It is clear from Eq. (V.3) that the structure of the NEMS frequency response is composed of many sub-harmonics. However, we will only consider the X_0 one in the following, which just corresponds to locking on the initial reference harmonic one would measure without mixing. The explicit expression of X_0 is given by the continued fraction:

$$X_0 = \cfrac{2\,F_L/\delta k}{a_0 - \cfrac{1}{a_1 - \cfrac{1}{a_2 - \cfrac{1}{a_3 - ...}}} - \cfrac{1}{a_{-1} - \cfrac{1}{a_{-2} - \cfrac{1}{a_{-3} - ...}}}}. \qquad (V.5)$$

Let us note that without mixing ($\delta k \to 0$), Eq. (V.5) reduces to the simple Lorentzian form.

V.2.2   Results

It is clear from Eq. (V.5) that both in-phase V_X and out-of-phase V_Y components of the signal are affected by the mixing process. We present in Fig. V.1 the measured resonance line of the goalpost mixed with a relatively low frequency signal on the gate.
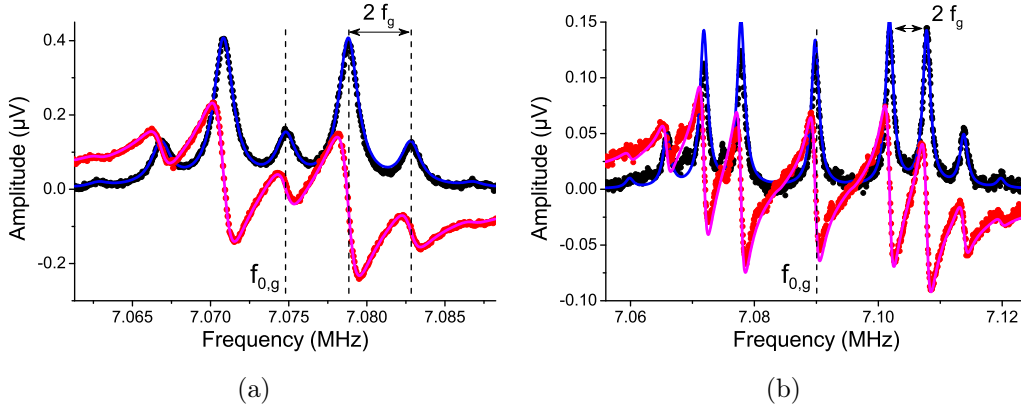
Figure V.1: The goalpost structure resonance line mixed with an A.C. gate signal. The force applied on the NEMS is $F_L = 3.9$ pN, the gate voltage is $V_g = 1.4$ V at the frequency $f_g = 2$ kHz (a) and $V_g = 2.5$ V at $f_g = 3$ kHz (b). We observe satellite peaks around the initial resonance frequency $f_{0,g}$, with their mirror image on the other side. Note that in the peculiar configuration of (a), the amplitude of the first satellite peaks are larger than the central one, but still smaller than the initial resonance line without mixing, such that the energy is preserved. The peaks are equally separated by $2\,f_g$. The full lines are calculations from Eq. (V.5) with no free parameters.

We clearly observe multiple additional peaks on both sides of the initial resonance line position, while still being in the linear regime. As predicted by Eq. (V.5), each
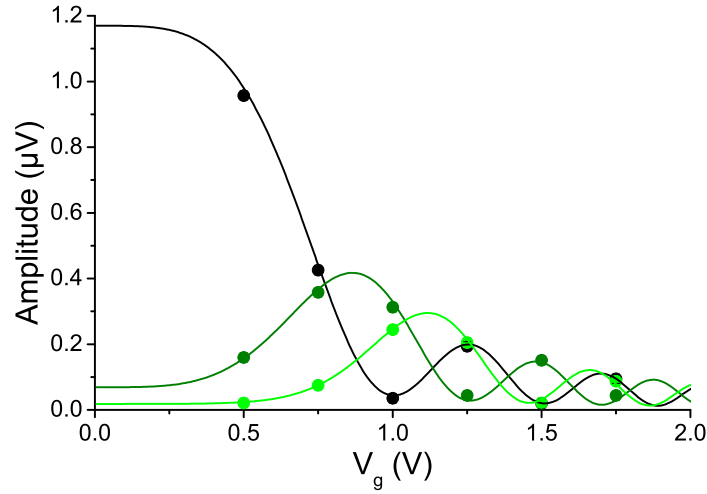
Figure V.2: In-phase amplitude of the three closest peaks from the initial resonance frequency $f_{0,g}$ with respect to the gate voltage V_g for $f_g = 1.5$ kHz. The error bars are within the points size. We show in black the peak at $f_{0,g}$, in dark green the first satellite one and in light green the second, where the lines are the calculations from Eq. (V.5) for each peak respectively. As V_g increases, the number of measurable satellite peaks also increases, but the average amplitude of each peak decreases, until vanishing to zero.
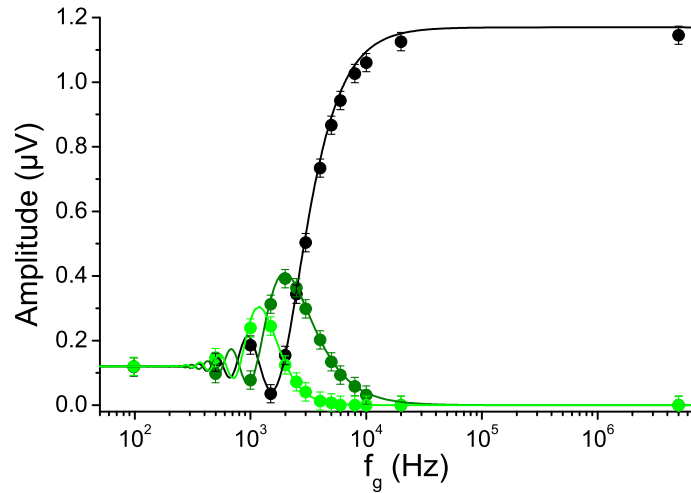
Figure V.3: In-phase amplitude of the three closest peaks from the initial resonance frequency $f_{0,g}$ with respect to the gate excitation frequency f_g for $V_g = 1.4$ V. The overall graphic style follows the one in Fig. V.2. As f_g decreases, the average peak amplitude decreases, but never falls down to zero.

peaks are separated by the excitation frequency of the gate experienced by the NEMS, which is $2\,\omega_g$. We also show in Fig. V.1 the numerical calculation from Eq. (V.5) with no free parameters, where we took into account 50 nested fractions

in the recursion for both configurations presented, although 5 would already be in very good agreement with Fig. V.1a (each fraction adds one peak in the shape of the resonance). Note that the slight asymmetry appearing on Fig. V.1b is due to the small D.C. offset on the gate voltage that is not taken into account here. Depending on the voltage applied on the gate and its excitation frequency, the amplitude of each peak changes in a non-trivial way, and we present in Fig. V.2 and Fig. V.3 the evolution of the central peak and the two first additional satellite ones with respect to both V_g and f_g. We see that as the voltage increases or the mixing frequency decreases, the additional peaks number increases but the amplitude of each peak decreases to satisfy the energy balance. The technique is thus not usable for too high modulation frequencies. In addition, as we get closer to the D.C. regime on the gate excitation one would assume that, following continuously from the actual D.C. regime (that is without mixing), all peaks would merge together leading to the initial Lorentzian line. However, a new regime occurs when $\omega_g < 2\,\Delta\omega$, as presented in Fig. V.4.
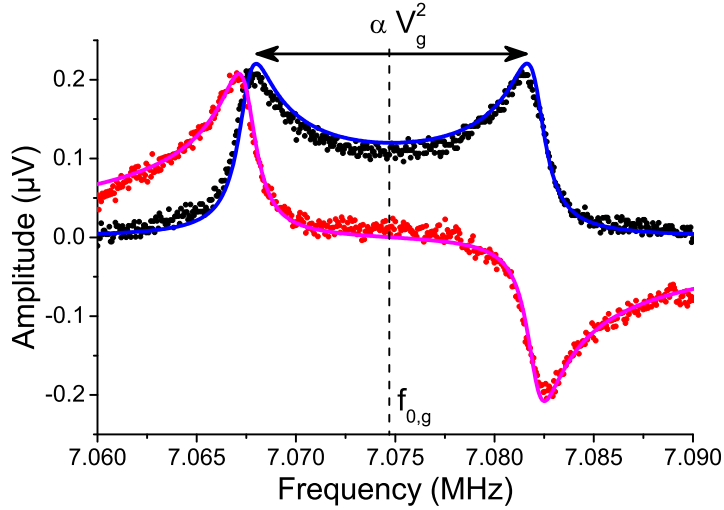
Figure V.4: Resonance line of the NEMS for a mixing frequency $f_g = 5$ Hz, at $V_g = 1.4$ V. We observe that the resonance shape is not a Lorentzian, even though f_g is close to the D.C. limit. The lines are calculations from Eq. (V.5), implementing 50 nested fractions in the recursion, with no free parameters.

As expected, all peaks merge together, but they form a hat shape characteristic structure. This is explained by the fact that the gate is modulating the resonance line so slowly that the oscillator reaches the stationary oscillation state before the gate voltage changes by an appreciable quantity. As long as our measurement technique averages over a time longer than $\frac{1}{\omega_g}$, we only measure the averaged position of the Lorentzian line. In this limit, we can calculate the exact lineshape by averaging the

quasi-stationary value of X_0 over the period $\dfrac{2\pi}{2\,\omega_g}$, giving:

$$X_0 = \frac{F_L}{m\,\omega_{0,g}^2}\;\frac{sign\left(\mathbb{R}\left[\frac{a_0}{2}\right]\right)}{\sqrt{\left(\frac{a_0}{2}\right)^2 - 1}}. \tag{V.6}$$

This expression coincides with Eq. (V.5) for very low modulation frequencies. Note that the distance between two peaks is here related to the modulation amplitude (and not to ω_g). In this configuration, we loose the information on the value of the mixing frequency. Thus, in order to perform this mixing scheme, one should be careful to work with frequencies such that $\omega_g > 2\,\Delta\omega$. Again, in Fig. V.4 the calculation matches the experiment without free parameters.

V.3   Damping mechanisms down to the millikelvin regime

V.3.1   Introduction to the Standard Tunneling Model

The low temperature dissipation in nanomechanics is a fundamental topic of research with a broad impact field, although its microscopic origin is still an open question. Indeed, there is at the moment no consensus on the nature and dependencies of the damping in nanoresonators, see Sec. II.5.1. As far as temperature is concerned, while the results in the literature quantitatively differ, the qualitative interpretation of the characteristics of dissipation in NEMS is mostly based on a theory of the early 70's: the Standard Tunneling Model (STM) [Anderson *et al.* 1972, Phillips 1972]. It is assumed that the low energy properties of the constitutive solids are dominated by entities tunneling between two essentially equivalent equilibrium states, which are commonly known as tunneling two level systems (TLS, see Fig V.5). Those states correspond to different configurations, which modify the properties of the material. While dedicated to amorphous solids, this theory phenomenologically also applies to crystalline materials based NEMS since they always suffer from defects thermally activated which relax their energy to the outside world. Those phenomena occur by absorbing or emitting phonons, which results in a variation of the dissipation and a shift in the resonance frequency of the resonator, enabling to probe the TLS behaviour.
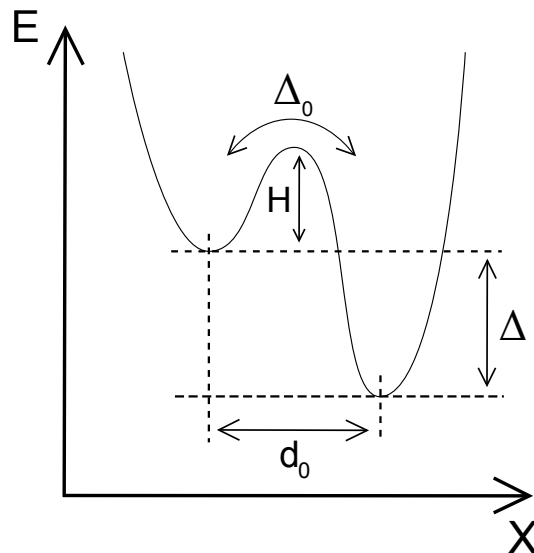
Figure V.5: Schematic of the double well potential energy experienced by two-level systems in some configuration space X, with d_0 the distance between the two wells and in the most general case a well have an asymmetry Δ. In the low temperature regime, the system does not have enough thermal energy to overcome the barrier height H and TLS only switch through tunneling, with characteristic amplitude Δ_0 (defined from the other parameters).

The STM predicts that the resonance frequency should decrease logarithmically as the resonator's temperature is decreased below a threshold $T^\star$, while the dissipation is supposed to decrease as a power law of temperature. Above $T^\star$ the dissipation saturates to an almost constant value (see Sec. II.5.2) while the frequency again shifts down logarithmically. The threshold temperature $T^\star$ is supposed to increase weakly with the resonance frequency. Many experiments validated qualitatively this theory, but depending on the materials and the sizes, the power laws found for the evolution of the dissipation as a function of the temperature are not consistent [Lulla 2011, Zolfagharkhani *et al.* 2005, Venkatesan *et al.* 2010, Hoehne *et al.* 2010]. This lack of "universality" in the experimental findings is in contradiction with the bulk situation for which almost all materials remarkably display similar properties [Southworth *et al.* 2009]. Beyond the fundamental issues at hand, understanding this phenomenon is a major issue for the implementation of high quality factor NEMS at low temperatures. In particular, this Chapter focuses on an aspect of the dissipation process which has been set aside, questioning on the importance of the electronic state of the metallic layer of the nanoresonators used in almost all the literature studying damping at low temperatures.

V.3.2   The electronic state contribution

To study such a phenomenon, we cooled the goalpost structure presented in Chap. II down to 35 mK using a pulse-tube dilution cryostat with the help of our post-doctoral fellow Kunal Lulla. At such small temperatures, the aluminium layer might be in the superconducting state **S**, while all previous measurements in this thesis were done at high enough temperatures to remain in the normal state **N** whatever the driving current or the magnetic field. Characterising and calibrating our device in its new environment, we found a superconducting critical temperature $T_c = 1.6$ K, a critical current of about 40 μA, an upper critical field $H_{c,\mathbf{N}} = 0.5$ T and a lower critical field $H_{c,\mathbf{S}} = 0.4$ T in between which the electronic state is not clearly defined, see Fig. V.6. It is important to note that the Al is a Type I superconducting material, with an abrupt transition from normal to superconducting states in the bulk. However, since the Al layer of the goalpost device is in the thin film limit, the mechanisms describing the superconducting transition is much more sophisticated: the T_c is relatively high (in the bulk it is about 1.2 K) and an intermediate state **I** appears [Cohen & Abeles 1968].

Depending on the state of the aluminum, the line termination is either superconducting (0 Ω) or normal (about 100 Ω here) which changes drastically the transmission. In the normal state, we could perform the same calibration of the injection and detection lines as described in Sec. II.4 in order to measure all parameters in real units. However, in the superconducting state the metallic layer is by definition non-resistive, thus no Joule effect is present: the calibration of the lines seem compromised. However, using a reasonably large D.C. voltage on the gate electrode coupled to the NEMS, it is possible to enter in the Duffing regime, as described in Sec. II.5.3. Having characterized this effect in the normal state, this coupling can
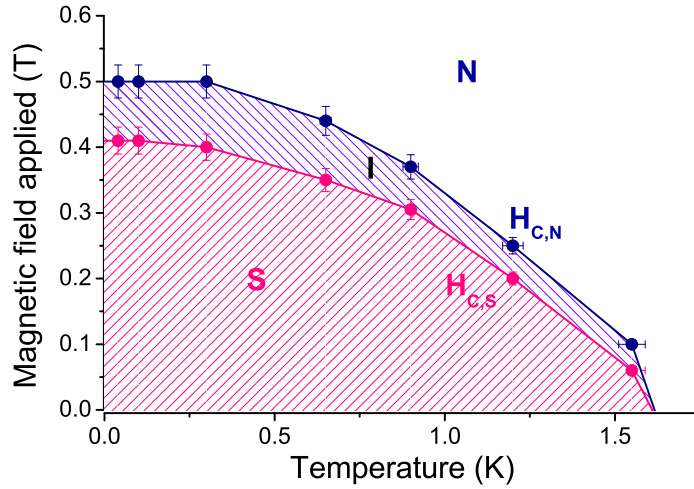
Figure V.6: Superconducting phase diagram of the aluminium layer in the resonator. Due to the reduced dimension of the system, an intermediate regime appears between fully normal or superconducting states. Below the critical temperature $T_c = 1.6$ K, the aluminium is in the superconducting state **S** between 0 T and 0.4 T (dashed pink region), in an intermediate state **I** between 0.4 T and 0.5 T (dashed purple region) and in the normal state **N** above 0.5 T (dashed dark blue region). All the data points have been taken well below the critical current of 40 μA.

be used as a calibration tool on its own: knowing the frequency shift per meters squared induced by the motion in the non-linear range (the β parameter), we can infer the displacement amplitude in the superconducting state from the position of the resonance line.

Beyond the tunable non-linear properties, both intrinsic Duffing non-linearity and measured damping may depend on the excitation (current drive and magnetic field), with different characteristics depending on the state of the metal. Thus a careful definition of the intrinsic measured damping does require a thorough study with respect to both field and current. Note that in the following results, the magnetomotive loading (see Sec. II.4.1) has already been subtracted. While it is measurable in the normal state (about 70 Hz/T^2) this field-dependent broadening is negligible in the superconducting state.

In the normal state, the intrinsic Duffing behaviour is very small but we observe in the superconducting state that the Duffing coefficient β increases as we reduce the current or the field (Fig. V.7), such that for low drive configurations in **S** state the resonance line is always in the Duffing regime. However, as explained in Sec. II.5.3, this effect does not affect the value of the maximal displacement amplitude x_{max}, from which it is still possible to extract the damping. Alternatively, a full fit can also be used (full lines in Fig. V.7). This drive-dependent non-linearity is puzzling and unexpected. One could argue that it is generated by complex non-linear dynamics of vortices within the superconducting layer [König *et al.* 1993]. Furthermore, the linewidth parameter $\Delta\omega$ needs a careful extraction since the dissipation *itself* ap-

(a)

(b)

(c)

(d)
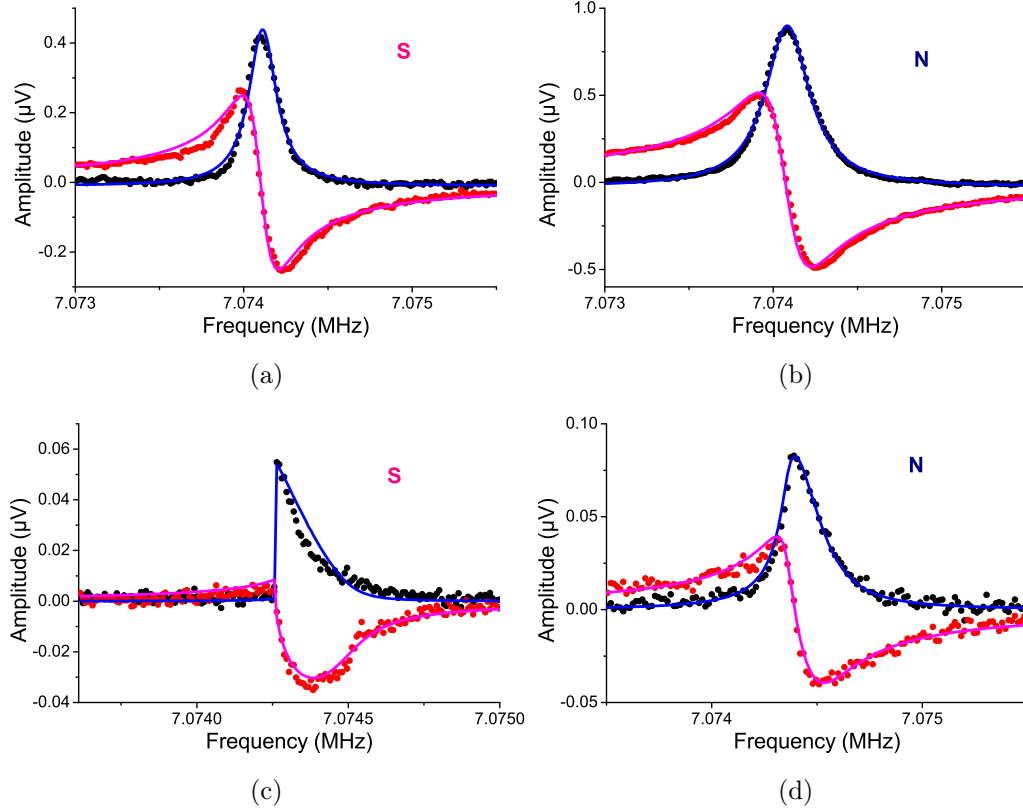
Figure V.7: Resonance lines of the NEMS for different current/magnetic field amplitudes at 95 mK (*a*: (**S**) 850 nA with 100 mT, *b*: (**N**) 330 nA with 600 mT, *c*: (**S**) 50 nA with 100 mT, *d*: (**N**) 20 nA with 600 mT). As we reduce either of the two driving parameters, we observe an increase of the non-linearity for the **S** state. However, by fitting the lines to the non-linear equation in Sec. II.5.3 (full lines) or by extracting the linewidth parameter from the maximum amplitude (Sec. II.5.4), one can recover the dissipation coefficient (presented lines measured by sweeping downwards).

pears to be non-linear with respect to the driving parameters. In Sec. II.5.4, for the **N** state we introduced that the intrinsic dissipation of the nano-structure increases linearly with x above a displacement threshold x_{th}. This effect has been attributed to anelastic properties of the coating materials (here, the Al layer). In the **S** state we observe a similar feature as a function of the applied current, but the linewidth seems to increase as a square root of the current, as presented in Fig. V.8. Hence, to extract the intrinsic dissipation of the NEMS we need to perform our measurement below this threshold, where the damping is roughly independent of injected current.

But as the magnetic field is varied, the dissipation is also affected, even *below* the apparent threshold (Fig. V.9). It is thus clear that these features cannot be related to the same anelastic properties as in the **N** state, and some other mechanisms intrinsic to the **S** state has to be invoked. Again we need to extrapolate at zero field to obtain the actual intrinsic dissipation of the NEMS. The interaction of vortices
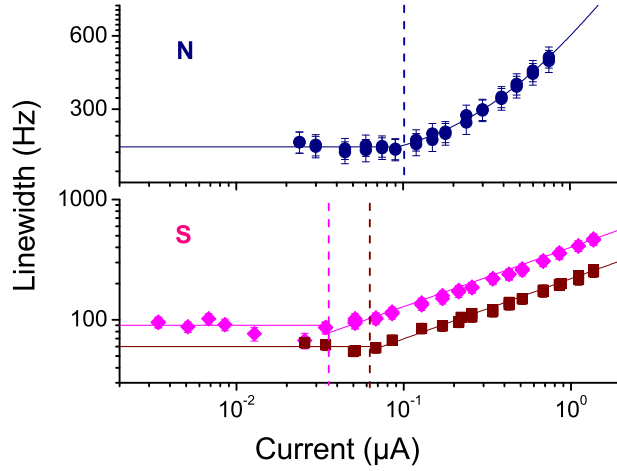
Figure V.8: Dissipation as a function of the driving current in log-log scale at 95 mK, in both **N** (upper panel, blue at 650 mT) and **S** (lower panel, magenta at 300 mT and dark red at 100 mT) states. In the **N** state the dissipation increases linearly with the current after crossing a threshold x_{th} (dashed vertical line), while in the **S** state the increase seems to follow a square root. Note that the threshold positions are not the same since the magnetic fields (thus the displacement) are not the same.
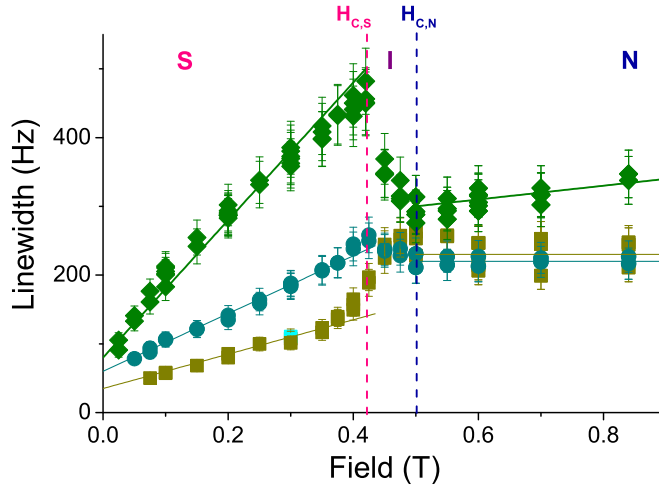
Figure V.9: Evolution of the linewidth as we increase the magnetic field at 95 mK, crossing the **S**, **I** and **N** states for three different applied currents (from bottom to top 50, 210 and 850 nA in the **S** and 20, 80 and 330 nA in the **N** state). We observe a clear difference between the three regions which demonstrates that one needs to extrapolate at zero field in order to know the intrinsic dissipation in the **S** state. In the **S** and **I** states, the lines are guides for the eye.

present in the Al layer might be the reason of such a variation. Note that this magnetic field dependence looks almost linear while a trivial loading effect would be quadratic.
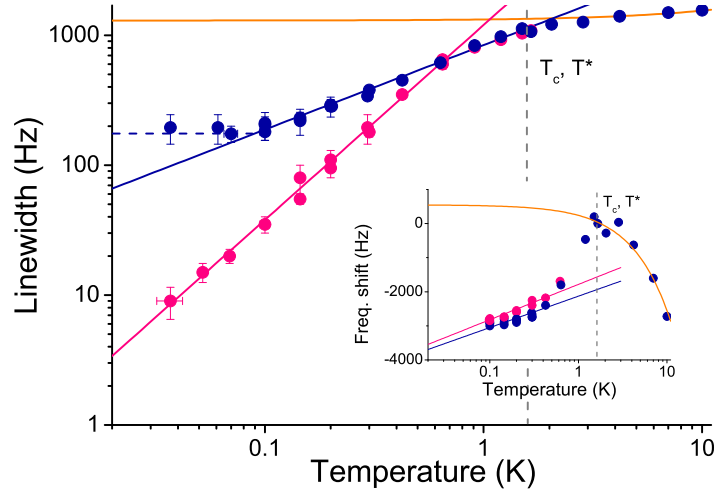
Figure V.10: *Main*: Evolution of the extrapolated linewidth (down to zero field and zero current) with respect to the temperature. We show in pink and dark blue the **S** and **N** states, with a vertical dashed line at the critical temperature T_c (which happens to be roughly equal to $T^\star$ as well). The lines on the data are guides for the eyes, showing a standard linear dependency for $T > T_c$ (orange line) and power law scalings at the lowest temperatures, of $T^{0.65}$ for the **N** state (dark blue line) and $T^{1.5}$ for the **S** state (pink line). The dashed horizontal line in the **N** state seems characteristic of a thermal decoupling (see text). *Inset*: Evolution of the resonance frequency of the NEMS as a function of the temperature. The graphic style is similar to the main graph. The parallel straight lines on the data at low temperature are logarithmic fits, as predicted by the STM model.

After taking care of those non-linear effects impacting the dissipation measurement at each temperature, we recover both frequency and linewidth variation from 30 K (**N** state, see Sec. II.5.2) down to 35 mK (**N** and **S** states), as presented in Fig. V.10. As predicted by the STM model, the resonance frequency shifts logarithmically at low temperatures, and the dissipation scales as a power law. However, we see a clear difference between the **N** and **S** states: the power law of the former with respect to the temperature is $T^{0.65}$ while the one of the latter is $T^{1.5}$, reaching a quality factor of about 1 million around 30 mK. While other experiments highlighted different power laws for the normal state, this result is a clear demonstration that the electronic state in the metallic layer of nano-electro-mechanical resonators plays a crucial role in the dissipation processes. Let us note that the separation between the two states occurs around $T_c/2$, which is the temperature from which the density of normal electrons starts to be reasonably low. Also, the normal state seems to saturate at the lowest temperature, which is attributed to the radio-frequency overheating present in the cell, maintaining the goalpost structure at an effective temperature of about 80 mK while the environment is colder. To make sure the set-up configuration has nothing to do with those results, we perform this experiment over two thermal cycles on two devices of the same chip, driving the NEMS

with the gate electrode as well instead of the magnetomotive $I \times B$. The exact same linewidth behaviours in both **N** and **S** states are obtained.

On one hand, this promising result can be seen as an oportunity to use the measurement of the linewidth as a thermometer at low temperatures, since in the **S** state it varies quite abruptly (with a $T^{1.5}$ law) without showing any sign of saturation down to 35 mK (due to clamping losses for example). In this case, the thermometer is measuring the temperature of *phonons*, and not electrons as in most devices. On the other hand, it leads to fundamental questions on the nature of the dissipation in nanomechanical devices at very low temperature. In the STM, the TLS present in the device absorb energy from the mode, which is then released to the outside world through their coupling to phonons and/or electrons. Depending on the dispersion relation of phonons confined in the mechanical mode, the variation with the temperature of the resulting dissipation is different: in the string regime, it was found to go as T^1 [Hoehne *et al.* 2010] while in the flexure regime it is supposed to go as $T^{0.5}$ [Seoánez *et al.* 2008]. However those works involve solely a coupling to phonons, whereas the electronic origin here is clear. Some papers are dealing with a discrepancy in the damping of normal and superconducting states in micromechanical devices [Haust *et al.* 2004, Weiss *et al.* 1981], but it does not reproduce our finding of the power scaling law $T^{1.5}$. Those new results are clearly calling for further experiments and new theoretical developments, taking into account the electronic degree of freedom, the reduced dimensionality and finally the order of the phononic dispersion law within the device (string or beam).

V.4 Slippage features in a rarefied gas

V.4.1 Probing gas properties with a NEMS

In the past few years, micro/nano-fluidics became of intense interest with the emergence of Lab-on-a-chip technologies and their applications in chemistry, biology and medicine [Terry *et al.* 1979, Manz *et al.* 1992]. Both MEMS and NEMS can contribute to a better understanding of the features at the heart of these fields [Karniadakis *et al.* 2005, Burg *et al.* 2007]. Indeed, their small but various sizes enable to investigate different fluid regimes while being genuinely local probes, and their high quality factors make them intrinsically very sensitive [Bullard *et al.* 2014].

Recently, a specific regime demonstrated a high potential for applications but which comprehension is very challenging: the flow within the boundary layer of a fluid, where the interaction between its constitutive particles and immersed surfaces are the strongest. In this regime, gigantic slippage has been observed leading to extremely efficient flows through extremely small apertures, which could lead to a technological revolution in nanoscale filtration [Holt *et al.* 2006, Siria *et al.* 2013]. In the high pressure limit the tangential velocity of a gas is assumed to vanish close enough to a surface: the fluid is supposed to be clamped on the irregularities of this wall, what is (conventionally) called the no-slip condition [Landau & Lifshitz 1987, Atta 1965]. However in a rarefied gas this boundary condition does not hold any more: the parallel velocity of the gas is non-zero even at the surfaces it is interacting with [Patterson 1956, Siria *et al.* 2009]. This boundary - so-called Knudsen - layer can be efficiently studied in a gas. Despite intensive numerical simulations [Bird 1994] the behaviour of this phenomenon is still not clear. As far as numerics are concerned, solving the full Boltzmann equation of a gas interacting with a wall is too demanding for nowadays computers [Reese *et al.* 2003], and the assumptions to simplify the calculations lead to different findings [Lilley & Sader 2007, Lockerby *et al.* 2005]. On the other hand investigating experimentally the Knudsen layer requires a sensor specifically designed for this purpose, presenting the properties of nanomechanical probes mentioned above: high Q and small sizes.

In this section, we present the theoretical background and the experimental signature of the Knudsen layer measured in ^{4}He gas at 4.2 K with two different NEMS already characterised in Chap. II: a 100 μm and a 300 μm high-stress SiN beams, which aspect ratios between length and cross-section are of the order of a thousand [Defoort *et al.* 2014a]. Furthermore, ^{4}He gas is an almost-ideal inert, mono-atomic gas which properties are tabulated [Arp *et al.* 1989], which makes it the best fluid available for our purpose. The 100 μm device has a gap g with the bottom of the chip of order 4 μm while the gap of the 300 μm one is of about 50 μm. While the different sizes of the beams just involve renormalisation in the formulae, the order of magnitude difference between the two gaps will demonstrate the robustness of our results, as it will be explained in the following. However, those large lengths lead to a high loading correction with the magnetic field, changing the measured

vacuum linewidth of our NEMS up to a factor 230 from 0 to 1 T for the 300 μm sample (Fig. II.14b). The dissipation, which is the essential information for this experiment, would have been even more affected with a 50 Ω loaded environment, and we see here how crucial the high impedance set-up can be (see Sec. II.4.1). The data presented here are free from loading, taken at the lowest magnetic field reachable for a decent measurement, but the extrapolation to the zero-field value is not trivial and the error bars of the extrapolated linewidth can reach 100 % of the bare value for the smallest dampings resolved. The experimental cell is the same one as presented in Chap. II and we fill it with regulated gas volumes to create a fluidic environment at different pressures. Our ^{4}He gas source is supposed to be pure (purity > 99%) and the remaining impurities should be adsorbed on cell walls for our temperature of 4.2 K, making the gas even cleaner. Only a few ppm concentration of ^{3}He may remain in the actual gas present in the cell. To measure the pressure, we used a Baratron pressure gauge connected to the pipes at the 300 K environment for pressures < 100 Torr. We made sure that the thermomolecular pressure corrections are negligible in the whole pressure range by measuring our NEMS with both a full and nearly empty Helium bath. Estimating them from length and diameters of the tubes leads to the same conclusions [Chernyak *et al.* 1973]. For pressures exceeding 100 Torr, we used a pre-calibrated Blondelle mechanical manometer. As we increase the pressure in the cell, the gas affects both the resonance frequency and the linewidth of the NEMS (Fig. V.11). For all measurements, we made sure to remain in the linear regime by using two different drives leading to the same (when rescaled) resonance peaks. This also confirms that the injected current does not heat the structure.
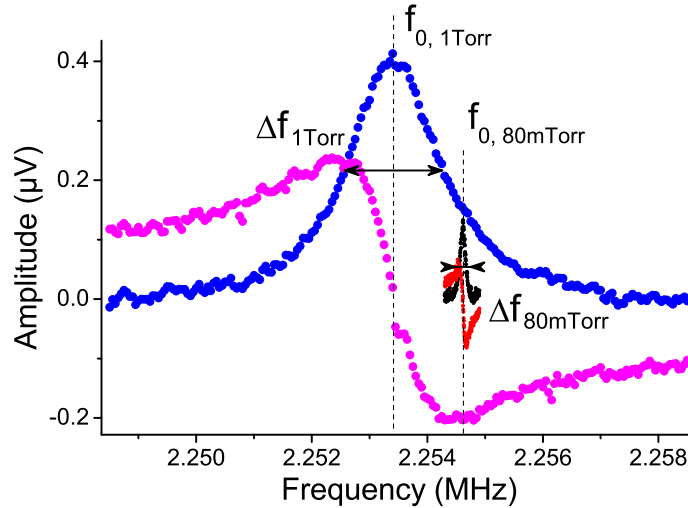

Figure V.11: Resonance lines of the first mode of the 100 μm doubly-clamped beam at two gas pressures (1 Torr in blue and magenta, 80 mTorr in black and red). As the pressure increases, the linewidth gets broadened and the resonance frequency shifts down. The measurements have been performed in the linear regime.

Two distinct effects explain the shift in frequency: at low pressures (< 2 Torr) ^{4}He atoms are being adsorbed onto the NEMS surface up to three atomic layers, increasing the effective mass and thus shifting down the initial resonance frequency, while at high pressure the shift follows the standard Navier-Stokes equation, and gas is dragged around the beam which increases the dynamic mass (Fig. V.12). This work does not pretend to study in details the adsorbed layers, but a quite convincing fit of the data can be produced from simple arguments (orange lines Fig. V.12). A first strongly bound monolayer is essentially always present for the range of pressures investigated, and on top of it two disordered layers are growing with characteristic isoterms of the Dubinin-Raduskevich type [Dash 1975]. We find a typical adsorption potential for the first layer of order 70 K, while the helium over-layer potential is around 29 K, with a spread due to the heterogeneous NEMS surface of order 10 K. These numbers are consistent with what can be expected from the literature [Goellner *et al.* 1975].
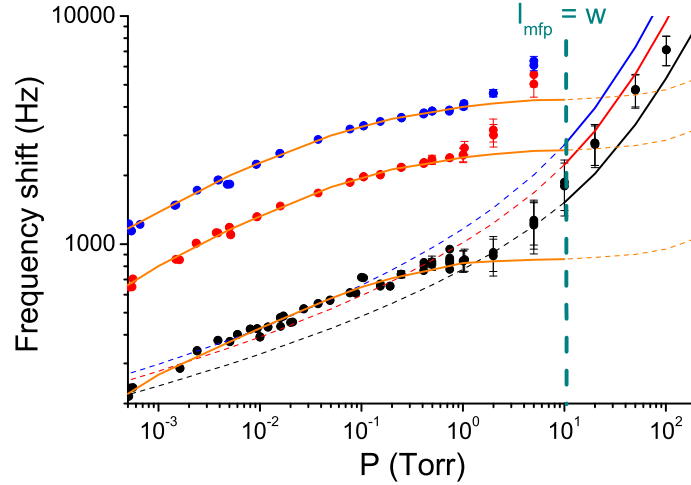
Figure V.12: Frequency shift of the resonance line of the measured mechanical modes. We present here the data of the fundamental mode (black points), the second harmonic (red points) and the fourth harmonic (blue points). In the low pressure regime, the adsorbed ^{4}He layers on the NEMS are the main cause of the frequency shift (orange lines, see text). The lines are extrapolated with the expected multi-layer condensation expression $\frac{1}{1-\frac{p}{p_0}}$ with p_0 the saturated vapour pressure (dashed lines). We present in comparison the Navier-Stokes dispersive components for each mode (with their respective colors), which contribute only at high pressures within its validity range (typically 10 Torr here, corresponding to a mean-free-path l_{mfp} comparable to the width w of the NEMS; below this limit the lines are dashed).

Essentially, the damping in a gas varies with pressure because of the variation of density. Two regimes can be distinguished, which will be described in the following: the low pressure, or molecular limit where particles have a very large mean-free-path, and the high pressure, or laminar limit where the gas is essentially a conventional viscous fluid.

V.4.2   The high pressure limit and the slippage correction

Before probing complex properties in a low pressure environment, we need to make sure we understand quantitatively our system in a more trivial regime: the high pressure (laminar) limit. When the mean-free-path of the ^{4}He molecules is small compared to any experimental dimensions, the Navier-Stokes equation enables to describe the fluid dynamics [Landau & Lifshitz 1987]. The local interaction force per unit length between the fluid and the NEMS is then [Sader 1998]:

$$\frac{\partial F_g\left(\omega, z\right)}{\partial z} = \rho_g\,\omega^2\,S_c\,\Lambda\left(\omega\right)\Psi_n\left(z\right)x_n\left(\omega\right), \tag{V.7}$$

with ρ_g the ^{4}He gas density, S_c the cross section of the structure and $\Lambda\left(\omega\right)$ the complex damping coefficient. Integrating the power $\dot{x}_n\,\Psi_n\,\frac{\partial F_g}{\partial z}$ resulting from Eq. (V.7) over the length of the probe and normalising to the mode mass ($\propto \int \Psi_n^2\left(z\right)dz$, see Eq. [II.6]) the associated dissipative and reactive parts (i.e. imaginary and real respectively) are obtained and the effective viscous forces can be injected in the dynamics equation, Eq. (II.5) [Defoort $et\,al.$ 2014a]. As a result the effective friction force is independent of the mode shape and length, but does depend on frequency. The remaining unknown is $\Lambda\left(\omega\right)$, which we define as:

$$\Lambda\left(\omega\right) = \Gamma\left(\omega\right)\Omega\left(\omega\right), \tag{V.8}$$

with $\Gamma\left(\omega\right)$ the Navier-Stokes solution for a cylinder [Stokes 1851] and $\Omega\left(\omega\right)$ a correction fraction introduced to match the rectangular cross section case (we use the expression given for the thin plaque $e \ll w$ which should be accurate enough, since it renormalises at most by 15 % the original $\Gamma\left(\omega\right)$ term) [Sader 1998]. We have:

$$\Gamma\left(\omega\right) = \frac{4}{1+i}\frac{J_1\left(\dfrac{1+i}{u}\right) + i\,Y_1\left(\dfrac{1+i}{u}\right)}{J_0\left(\dfrac{1+i}{u}\right) + i\,Y_0\left(\dfrac{1+i}{u}\right)}, \tag{V.9}$$

where $u = \frac{\sqrt{2}\,\lambda_p}{w}$, $\lambda_p = 2\sqrt{\frac{\eta}{\rho_g\,\omega}}$ being the viscous penetration depth (with η the viscosity) and w the width of the NEMS, J and Y are the Bessel functions of first and second kind.

As the ^{4}He gas pressure is reduced, the damping coefficient needs to be corrected due to slippage on the device. When the mean-free-path l_{mfp} of the gas particles becomes comparable to the NEMS width, the tangential velocity does not reduce to a zero value on the surface. At first order, this effect is taken into account through the introduction of a slip length l_{slip} which corresponds to the distance $behind$ the surface at which the velocity would have eventually reached zero if extrapolated [Lilley & Sader 2008]. This length depends on the surface aspect which is characterised by a number s ranging from 0 (completely diffusive surface) to 1 (perfectly
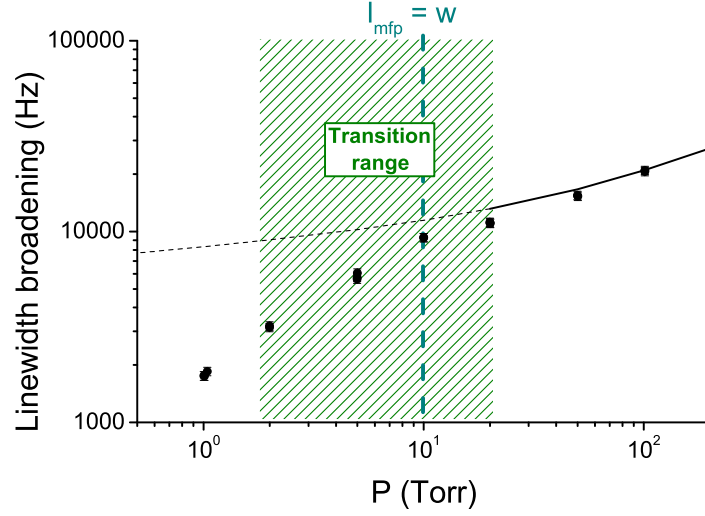
Figure V.13: Evolution of the linewidth of the 100 μm nano-resonator in the high pressure limit. In this regime we could only probe the fundamental mode (black data points), and the full line represents the Navier-Stokes calculation done with a slippage correction of $s = 0.5$ taking into account the finite mean-free-path l_{mfp} (or finite width w). When l_{mfp} becomes too large compared to w (as we reduce the pressure), the Navier-Stokes equation is not relevant any more (dashed line). In the shaded region, we represent the transition range between the two regimes.

specular surface) [Jensen *et al.* 1980], and we have:

$$l_{slip} \approx 1.15 \frac{1+s}{1-s} l_{mfp}. \tag{V.10}$$

Implementing this new feature in the damping coefficient, we renormalise it such that [Carless *et al.* 1983]:

$$\Lambda(\omega) - 1 \rightarrow \frac{1}{(\Lambda(\omega)-1)^{-1} - i \dfrac{1}{2\,u^2} \dfrac{l_{slip}}{l_{slip} + \frac{w}{2}}}. \tag{V.11}$$

From the SEM pictures of our devices Fig. II.24, we see that the surface is neither completely diffusive nor perfectly specular, and we present in Fig. V.13 the calculations above for the reasonable value of $s = 0.5$. The fit is indeed rather good up to $l_{mfp} \approx w$.

V.4.3 From the molecular regime to the Knudsen layer investigation

When the gas pressure is reduced further, l_{mfp} is so large compared to the structure cross-dimensions that the NEMS is not sensing the gas as a fluid but as a molecular flow, probing the microscopic mechanisms of each particle bouncing off the device: the Navier-Stokes equation is not valid any more. The different regimes

can be discriminated by the Knudsen number $Kn = \frac{l_{mfp}}{w}$. For $Kn < 0.1$, continuum fluid mechanics applies, for $0.1 < Kn < 10$ we observe a transition regime (shaded region in Fig. V.13 and Fig. V.14) and for $Kn > 10$, the fluid is in the molecular regime. In this low-pressure range, the interaction between the gas and the NEMS should be calculated from the transfer of momentum of each gas particle hitting the structure. The statistical velocity distribution f_v of particles from the equilibrium Maxwell-Boltzmann law writes [Patterson 1956]:

$$f_v\left(v_x, v_y, v_z\right) = \left(\frac{\beta_0}{\pi}\right)^{\frac{3}{2}} e^{-\beta\left[(v_x - v_{x,0})^2 + (v_y - v_{y,0})^2 + (v_z - v_{z,0})^2\right]}, \tag{V.12}$$

with $\beta_0 = \frac{m_{He}}{2\,k_B\,T_0}$ and v_i the ^{4}He atoms velocity in the $i = x, y, z$ direction. The index 0 refers to global flow properties, defined over a small volume in the vicinity of the probe. The intrinsic statistical average velocity is then defined by:

$$v_g = \frac{2}{\sqrt{\pi\,\beta_0}}. \tag{V.13}$$

Since $\vec{x}$ is the only relevant direction considering the symmetry of the problem, we only consider v_x terms from now on. Depending on the nature of the interaction with the surface, the equation describing the damping force is different. In the perfectly specular case and developing at first order in $v_{x,0}$, the force exerted on both front and back sides of the NEMS by the ^{4}He particles transferring momentum is:

$$\frac{\partial F_g}{\partial z} = 2\,\rho_g\,w\,v_g\,i\,\omega\,\Psi_n\left(z\right)x_n\left(\omega\right), \tag{V.14}$$

where $i\,\omega\,\Psi_n\left(z\right)x_n\left(\omega\right)$ represents the NEMS velocity at position z and frequency ω in the complex form. For the completely diffusive case, either the surface has irregularities which imply that the momentum of a particle before and after bouncing off the NEMS are not correlated, or the incoming particle sticks on the surface and another one previously stuck leaves it. Considering the high-sticking properties of ^{4}He [Sinvani et al. 1983], we describe the diffusive case using the latter mechanism. The major difference with the specular case is that the particles from the gas at temperature T will thermalise with the NEMS at temperature T_r before leaving the structure. Defining the corresponding β_r from T_r, we obtain for the diffusive case:

$$\frac{\partial F_g}{\partial z} = 2\,\rho_g\,w\,v_g\,\frac{1 + \frac{\pi}{4}\sqrt{\frac{\beta_0}{\beta_r}}}{2}\,i\,\omega\,\Psi_n\left(z\right)x_n\left(\omega\right). \tag{V.15}$$

In the more general case, combining both specular and diffusive forces, we have:

$$\frac{\partial F_g}{\partial z} = 2\,\alpha\,\rho_g\,w\,v_g\,i\,\omega\,\Psi_n\left(z\right)x_n\left(\omega\right), \tag{V.16}$$

with $\alpha = s + (1 - s)\,\dfrac{1 + \frac{\pi}{4}\sqrt{\frac{\beta_0}{\beta_r}}}{2}$. Considering that our NEMS is thermalised to the Helium bath at 4.2 K and that the heat from the current can be neglected, we have

$\beta_0 \approx \beta_r$. Since $\dfrac{1 + \frac{\pi}{4}}{2} \approx 0.89$, we see that α is almost independent of the surface aspect parameter s. However to follow on from the high pressure regime we keep $s = 0.5$ and we have $\alpha \approx 0.95$. We show in Fig. V.14 the molecular regime effect on the dissipation, both experimentally and calculated from Eq. (V.16): the expression is proportional to P with no free parameters. Note that following the same calculation procedure as in the laminar case, the resulting linewidth broadening is independent of frequency.
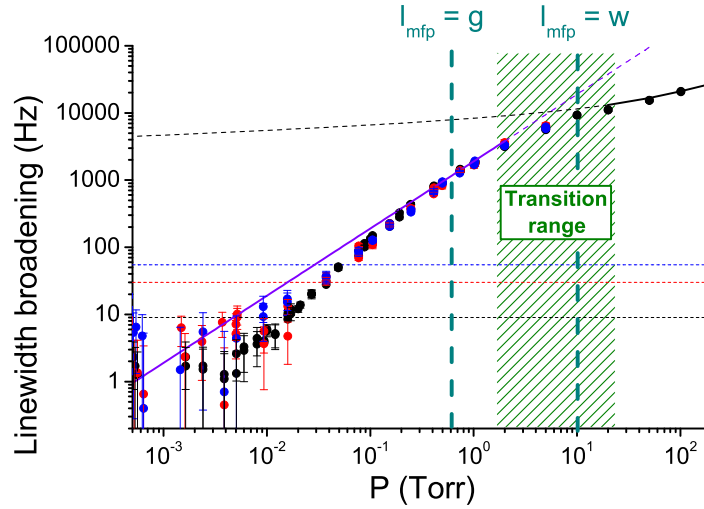
Figure V.14: Evolution of the linewidth for the 100 μm device modes as a function of the pressure in the cell. We focus here on the low pressure data, where the mean-free-path becomes larger than the width of the beam, which is then described as the molecular regime (purple line). We could measure in this range the three modes introduced in Fig. V.12 (same conventions), and observe a similar behaviour for each of them. However, when l_{mfp} is larger than the gap g between the bottom of the chip and the beam, we observe a clear deviation between the experimental data and the calculation. The dashed horizontal lines represent the linewidth of each mode in vacuum, which gives an idea of the subtractions involved to capture the broadening of the linewidths and which cannot explain the deviation.

Theory and experiments do agree slightly below the transition regime, which itself is very difficult to capture [Bullard *et al.* 2014, Yamamoto & Sera 1985]. However, as we reduce the pressure (increasing the mean-free-path) the measured damping falls *below* the molecular calculation. As a matter of fact, one could first suspect that the NEMS itself is perturbing the gas and that the device is no longer a non-invasive probe. Indeed, close to the surface of the beam (within one mean-free-path), the particles of the gas will hit the NEMS more frequently than themselves, so that we are no longer sensing the truly bulk properties. As a consequence, the velocities of the ^{4}He atoms near the device should be slightly different than the ones predicted by the Boltzmann distribution function. The simplest way of describing such deviations to study molecular dynamics is to implement a first order correc-

tion in Eq. (V.12) [Patterson 1956]. This affects the calculations of the interaction force between the gas and the solid, and using conservation relations it is possible to estimate these corrections. They are proportional to velocity gradients near the surface, or temperature gradients, and as such will depend on the NEMS excitation amplitude. However, for the 100 μm structure and the drives we use, the correction should be of only 5% maximum for a mean-free-path of 40 μm, while the measured discrepancy between theory and experiment for these settings is more than a factor of two [Defoort *et al.* 2014a]. Hence, the presence of the NEMS itself cannot explain our experimental observations. Furthermore, the discrepancy on the linewidth appears for mean-free-paths of the order of the gap between the NEMS and the bottom of the chip (for both 100 μm and 300 μm beams, with gaps g of respectively 4 μm and 50 μm): we are left with the fact that we are probing features from the Knudsen layer attached to the bottom surface underneath the NEMS.

Extensive work has been done on this boundary layer problem, mostly theoretical with both analytical and numerical calculations [Lilley & Sader 2007, Lockerby *et al.* 2005, Bird 1994]. One main issue is the computer time needed to model a realistic system while solving the Boltzmann equation. Indeed, using direct simulation Monte Carlo, just solving the two-dimensional problem for a microcantilever interacting with a rarefied flow would involve hours of supercomputers calculations [Reese *et al.* 2003]. Solving such a problem is thus not a trivial task, and due to the different approaches (the linearised Boltzmann equation, the Monte Carlo simulations, using hard sphere or variable soft sphere assumptions) the results differ. The last theories lead to the fact that the velocity of the particles decreases as a power law $d \approx 0.8$ as we enter in the Knudsen layer until reaching the non-zero velocity at the bottom of the surface (related to the associated slip length) [Lilley & Sader 2007], but the actual effect on the effective viscosity within this layer is still an open question. Two main ideas are discussed: the viscosity of the gas decreases until reaching half of the bulk value [Lockerby *et al.* 2005], or the viscosity vanishes to zero with a power law of $1 - d \approx 0.2$ [Lilley & Sader 2008].

In our system, the measured extra dissipation felt by the NEMS is directly linked to the effective viscosity of the surrounding flow. Since the viscosity decreases with $\dfrac{l_{mfp}}{g}$, we propose the following phenomenological renormalisation [Defoort *et al.* 2014a]:

$$\Delta\omega \propto \frac{1}{1 + b\left(\dfrac{l_{mfp}}{g}\right)^a},\tag{V.17}$$

with a and b the fitting parameters. We show in Fig. V.15 the damping measured normalised to $2\,\rho_g\,w\,v_g$ (prefactor of Eq. [V.16]) together with Eq. (V.17). While the formula do fit the data, the two fitting parameters need to be adjusted for each NEMS, and the exponent a does not match with the theoretical predictions: we observe a faster decrease of the effective viscosity.
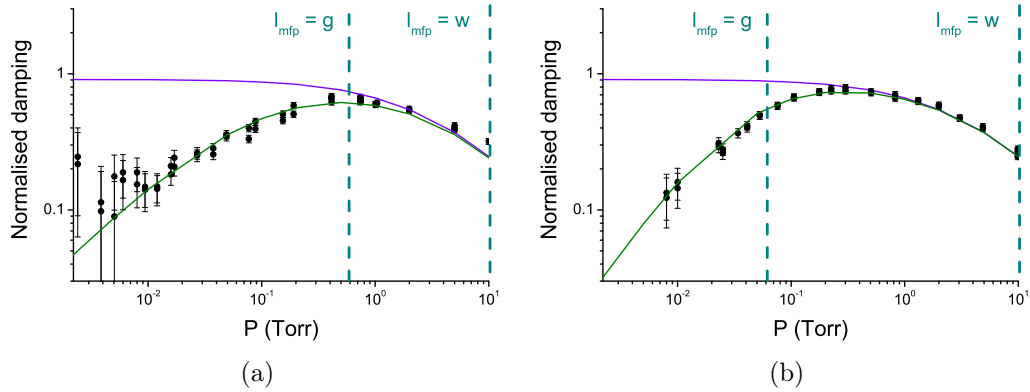
Figure V.15: Broadening of the linewidth of the first mode normalised to $2\,\rho_g\,w\,v_g$ as a function of the pressure. This normalisation highlights the deviation due to the entrance in the Knudsen layer, for $l_{mfp} > g$ ($g = 4\ \mu$m for the 100 μm beam [a] and $g = 50\ \mu$m for the 300 μm beam [b]). The purple lines are molecular calculations incorporating the cross-over description [Yamamoto & Sera 1985] and matching Eq. (V.16) at low pressures. Following Eq. (V.17), we used the fitting parameter $a = 0.8 \pm 0.1$ and $b = 0.18 \pm 0.05$ (a) and $a = 1.15 \pm 0.1$ and $b = 0.65 \pm 0.1$ (b) which reproduce (green lines) the measured data points.

While we clearly see an effect due to the Knudsen layer, we cannot explain quantitatively its behaviour with the actual experimental and theoretical results. However, our results clearly demonstrate that the viscosity does not decrease just to half of its bulk value, but seems to vanish to zero following qualitatively the latest numerical simulations: the lowest pressure data points in Fig. V.15 present a reduction of the damping of about a factor of 10, which is an unprecedented result to our knowledge.

V.5   Conclusion

In this Chapter, we focused on another use of NEMS, namely using them as probes instead of model systems. We presented different configurations involving various NEMS with distinct objectives. While more suited to applied physics issues, we nonetheless demonstrated here the potential of NEMS implemented as probes for many fields of fundamental physics.

In a first section, we took benefit of the non-linear coupling between the goalpost structure and the gate electrode to imprint in the resonance line of the resonator a low frequency signal from the electrode. We could compare our results with theory, which perfectly matches to the data without free parameter. Our measurements demonstrate that from the resonance shapes (in the multi-peaks configuration) it should be possible to deconvolute the mixing frequency and thus detect a small low-frequency signal from its impact on the high-frequency motion. While frequency-mixing has already been observed at the nano-scale using intrinsic non-linearities, we were able here to perform audio-mixing while remaining in the (non-Duffing) linear regime [Defoort *et al.* 2011].

In a completely different field, we could use the same goalpost structure to probe mechanisms at the core of the mechanical dissipation of the structure itself, namely the Two Level Systems (TLS). Recent work has been focused on determining the power law with which the dissipation in micro/nano-resonators decreases with temperature. In this second section we investigated another aspect: how the electronic state of the metal, covering almost all nano-devices used for the low-temperature study of TLS in the literature, affects the dissipation in the whole structure. Using a 20 mK based temperature pulse-tube dilution cryostat, we measured the damping of the goalpost at different temperatures in both normal **N** and superconducting **S** states of the aluminium layer. The latter one demonstrates exotic behaviour on the resonance line of the NEMS, which appears to be highly non-linear. After a thorough study of this feature, we could extrapolate to zero field and derive the resonator's dissipation. Comparing those results with the **N** state ones, we show an unprecedented difference on the power laws versus temperature between **N** and **S** states. No present model can explain those results, which are calling for new theories [Lulla *et al.* 2013].

Finally, thanks to their small intrinsic linewidths resonance, we presented how very long beams (with high aspects ratios) can be used in microfluidics. Close to a surface, the tangential velocity of a fluid is supposed to vanish, the fluid being stuck by the surface. However, when the mean-free-path of a gas becomes large enough (for small enough pressures), the gas experiences slippage, a new feature occurring within the boundary layer of order one mean-free-path next to the wall. In this last section we expose an unprecedented experimental investigation of this so-called Knudsen layer, probing the effective viscosity of the gas describing the slippage property. Comparing the results with the most recent theories, we obtain a qualitative agreement with a power law decrease of the effective viscosity towards zero as we get closer to the surface from which the boundary layer is defined [Defoort *et al.* 2014a].

V.6 Perspectives

Applications of NEMS as probes in condensed matter physics is a very broad field of research, which perspectives are continuously expanding. In this Chapter, we have been dealing in particular with the use of NEMS as probes for fundamental issues of physics.

As far as Two Level Systems (TLS) are concerned, the results we presented are just the first observation of a phenomenon of high impact in the study of TLS with NEMS: the importance of the electronic degree of freedom in dissipation mechanisms. While our measurements are reproducible over two devices of the same chip after several cooling cycles, a very interesting test would be to change the material or the shape of the structure, moving from a cantilever to a doubly clamped beam or changing the metallic layer. Since the TLS affect the dissipation in the NEMS, comparing low-stress and high-stress SiN devices could bring new information. No theoretical model encompasses all experimental results so far, and more statistics is clearly required. On the other hand, while the fast decrease of the dissipation with the temperature brings new questions on the origin of the mechanisms, it could also have a big impact in low temperature technologies. Indeed, if the properties observed can be engineered to match technical demand, superconducting mechanical structures would be low temperature phononic thermometers of high precision, down to at least 20 mK (temperature at which still no saturation has been seen in our experiment).

NEMS are also promising structures to probe micro-fluidics. In the particular case of the fundamental investigation of the Knudsen layer, the study of two different gaps between probe and boundary surface (differing by more than an order of magnitude) with two different resonator's size (differing in length by a factor of 3) demonstrated that the characterisation of this phenomenon needs very different length-scales to observe any change. Fabricating an even longer beam (for example 500 μm) would enable a very small intrinsic linewidth and thus a better precision on the viscosity variation. We also showed that the analytical description of the extra decrease of the damping needs both more theory and experiments (with for example a full statistics including larger gaps) to understand the tendency of this reduction, and thus the behaviour of the Knudsen layer. Finally, as far as low temperature physics is concerned, this results definitely validate the use of NEMS for the study of quantum fluids (^{3}He and ^{4}He) with new probes sensing the elementary excitations of the liquid down to the nanometer scale.

V.7   Résumé

Dans ce chapitre, nous nous sommes concentrés sur une autre application des NEMS, en les utilisant comme sondes plutôt que comme systèmes modèles. Nous y présentons différentes configurations impliquant différents NEMS avec des objectifs distincts. Bien que plus adapté aux questions de physique appliquée, nous démontrons ici le potentiel des NEMS comme sondes pour de nombreux domaines de la physique fondamentale.

Dans une première section, nous avons mis à profit le couplage non linéaire entre notre NEMS en fome de portique et l'électrode de grille qui lui fait face afin d'imprimer dans la raie de résonance du nano-résonateur un signal à basse fréquence, lui-même contrôlé à partir de l'électrode (Fig. V.1). Nous avons observé une correspondance parfaite (sans paramètre libre) en comparant nos résultats expérimentaux et théoriques. Nos mesures montrent qu'à partir de la forme des résonances (dans la configuration multi-pics), il devrait être possible de déconvoluer les fréquences des différents signaux, et donc de détecter un petit signal à basse fréquence à partir de son impact sur le mouvement à haute fréquence. Bien que le fait de mélanger des fréquences ait déjà été observé à l'échelle nanométrique en utilisant des non-linéarités intrinsèques aux structures, nous avons pu ici le réaliser tout en restant dans le régime linéaire (non-Duffing) [Defoort *et al.* 2011].

Dans un tout autre domaine, nous avons pu utiliser le même résonateur pour sonder les mécanismes à la base de la dissipation mécanique de la structure elle-même, à savoir les systèmes à deux niveaux (TLS). Des travaux récents, utilisant les micro/nano-résonateurs, ont permis d'étudier la loi de puissance avec laquelle la dissipation diminue avec la température. Dans cette deuxième partie, nous avons étudié un aspect différent de ce domaine : la façon dont l'état électronique du métal, couvrant presque tous les nano-dispositifs utilisés dans la littérature pour l'étude des TLS à basse température, affecte la dissipation dans l'ensemble de la structure. Utilisant un cryostat à dilution pulse-tube ayant une température de base de 20 mK, nous avons mesuré l'amortissement de la résonance de notre NEMS à différentes températures dans l'état normal **N** et l'état supraconducteur **S** de la couche d'aluminium (Fig. V.6). Dans ce dernier cas, on observe un comportement exotique de la résonance du NEMS, qui semble être fortement non-linéaire (Fig. V.7). Après une étude approfondie de cet aspect, nous avons pu extrapoler nos résultats à champ magnétique nul et extraire la dissipation du résonateur. En comparant ces résultats avec ceux de l'état **N**, nous avons mis en évidence une différence sans précédent sur les lois de puissance en fonction de la température entre les états **N** et **S** (Fig. V.10). Cependant, aucun modèle actuel ne peut expliquer ces résultats, qui réclament de nouvelles théories [Lulla *et al.* 2013].

Enfin, grâce à leurs fines largeurs de raie intrinsèques, nous avons présenté la façon dont de très longues poutres doublements encastrées (avec des facteurs d'aspects élevés) peuvent être utilisées en microfluidique. A proximité d'une surface, la vitesse tangentielle d'un fluide est censée être nulle, le fluide étant bloqué par la surface. Toutefois, lorsque le libre-parcours-moyen d'un gaz devient suffisamment

grand (pour des pressions suffisamment faibles), le gaz est sujet au glissement, un nouveau phénomène exercé au sein de la couche limite, distante d'environ un libre-parcours-moyen de la paroi. Dans cette dernière section, nous exposons une étude expérimentale sans précédent de cette couche dite de Knudsen, sondant la viscosité effective du gaz décrivant les propriétés de glissement qu'il subit (Fig. V.14). En comparant ces résultats avec les plus récentes théories, nous obtenons un accord qualitatif avec une diminution en loi de puissance de la viscosité effective vers zéro tandis que nous nous rapprochons de la surface à partir de laquelle la couche limite est définie (Fig. V.15) [Defoort *et al.* 2014a].

Overview and conclusion

Contents

VI.1   Achievements of the presented work

In this thesis we demonstrated how a Nano-Electro-Mechanical System can be used to probe fundamental phenomena arising from its non-linear behaviour. After a thorough calibration of our magnetomotive experimental set-up [Collin *et al.* 2012], we characterised the dynamics of our nano-resonators from the linear [Collin *et al.* 2014] all the way up to the highly non-linear regime, leading to an exhaustive comprehension of the Duffing oscillator [Defoort *et al.* 2013b]. This non-linear system, at the core of the present manuscript, enables to investigate different aspects of fundamental physics, some of them involving non-linear couplings between distinct degrees of freedom.

In the framework of nano-resonators, the coupling between their own vibrating modes is a study with promising benefits. Making use of the mode-coupling technique, we developed a new scheme to improve the measurement precision of the NEMS' resonance, coupling the actual mode with itself thanks to a two-tone drive set-up [Defoort *et al.* 2013a].

NEMS can also be thought of as *model systems*, and the transitions between the two states within the hysteresis emerging from the Duffing oscillator brings information on a general physical phenomenon: the bifurcation process, which is at the core of any first order transition phenomenon. Predicted to be universal within a narrow region, the power law dependencies of the hysteresis' sweeping parameter were investigated beyond the applicability limit of the analytical theory, together with the dependency to the non-linearity which is the essence of the bistable regime. We found both experimentally and numerically that the exponents hold in a range orders of magnitude larger than the one calculated from the theory [Defoort *et al.* 2014b], as previous numerical calculation suggested. While being of fundamental origin, we present how the bifurcation scheme in NEMS can be used to detect the behaviours of low-frequency two-level systems within the resonator's material.

As detectors, nano-resonators are very highly sensitive structures using numerous detection techniques. In this case, these objects are not themselves model systems but probes for condensed matter physics. We presented an audio-mixing scheme in which a low frequency signal can be imprint within the NEMS' resonance frequency [Defoort *et al.* 2011]. We could probe at very low temperatures the mechanical damping resulting from the two level systems present within the device [Lulla *et al.* 2013]. We also described the measurement of fluid friction obtained with a nano-string used as a detector in a low pressure gas in the molecular regime [Defoort *et al.* 2014a].

NEMS' implementation techniques are in constant improvement, and the nonlinear properties of those nano-resonators enable new drive and detection schemes to be used. By means of all of these various approaches, those nano-structures are key devices in both applied physics and fundamental research. The present work is a new and original step towards the use of nano-resonators as model systems and probes for condensed matter physics.

VI.2   Résumé général et conclusion

Dans cette thèse, nous avons démontré comment un Système Nano-Électro-Mécanique peut être utilisé pour sonder les phénomènes fondamentaux découlant de son comportement non-linéaire. Après une calibration approfondie de notre dispositif expérimental [Collin *et al.* 2012], nous avons caractérisé la dynamique de nos nano-résonateurs du régime linéaire [Collin *et al.* 2014] jusqu'au régime fortement non linéaire, conduisant à une compréhension exhaustive de l'oscillateur de Duffing [Defoort *et al.* 2013b]. Ce système non-linéaire, qui est le thème au cœur de ce manuscrit, permet d'étudier différents aspects de la physique fondamentale, certains impliquant des couplages non-linéaires entre différents degrés de liberté.

Dans le cadre des nano-résonateurs, l'étude du couplage entre leurs propres modes de vibration est un sujet aux avantages prometteurs. Utilisant la technique de couplage entre modes, nous avons développé une nouvelle technique pour améliorer la précision de la mesure de la résonance du NEMS, couplant ledit mode avec lui-même grâce à un dispositif d'excitation à double-ton [Defoort *et al.* 2013a].

Les NEMS peuvent également être considérés comme des *systèmes modèles*, et la transition entre les deux états de l'hystérésis émergeant de l'oscillateur de Duffing apporte des informations sur un phénomène général en physique : le processus de bifurcation, qui est au cœur de tout phénomène de transition de premier ordre. Prévues pour être universelles dans une région étroite, les dépendances en loi de puissance des paramètres caractéristiques de la bifurcation en fonction du point de fonctionnement ont été étudiées au-delà de la limite d'applicabilité de la théorie analytique, ainsi que la dépendance à la non-linéarité qui est l'essence même du régime bistable. Nous avons trouvé à la fois expérimentalement et numériquement que les exposants restent valables dans une gamme qui est des ordres de grandeur plus grande que celle proposée à partir de la théorie analytique [Defoort *et al.* 2014b], comme l'avait suggéré des calcul numériques antérieurs. Bien qu'étant d'origine fondamentale, nous présentons comment le phénomène de bifurcation peut être utilisé pour détecter les comportements basse-fréquence des systèmes à deux niveaux présents au sein du matériau du résonateur étudié.

En tant que détecteurs, les nano-résonateurs sont des structures très sensibles pouvant être utilisé dans de nombreuses techniques de détection. Dans ce cas, ces objets ne sont plus eux-mêmes des systèmes modèles, mais des sondes pour la physique de la matière condensée. Nous avons présenté un système de mixage audio dans lequel un signal de basse fréquence peut être imprimé dans la fréquence de résonance du NEMS [Defoort *et al.* 2011]. Nous avons pu sonder à très basses températures la dissipation mécanique résultant des systèmes à deux niveaux présents dans le dispositif [Lulla *et al.* 2013]. Nous avons également décrit une technique de mesure pour la viscosité des fluides obtenue avec une nano-corde utilisée en tant que détecteur dans un gaz à basse pression dans le régime moléculaire [Defoort *et al.* 2014a].

Les techniques de mise en œuvre des NEMS sont en constantes amélioration, et les propriétés non-linéaires de ces nano-résonateurs permettent la réalisation de nouvelles techniques d'excitation et de détection. De part l'ensemble de ces différentes approches, ces nano-structures sont des dispositifs clés à la fois en physique appliquée et en recherche fondamentale. Le travail présenté dans cette thèse est une étape nouvelle et originale vers l'utilisation des nano-résonateurs comme systèmes modèles et sondes pour la physique de la matière condensée.

Bibliography

[Aldridge & Cleland 2005] J. S. Aldridge and A. N. Cleland. *Noise-Enabled Precision Measurements of a Duffing Nanomechanical Resonator*. Physical Review Letters, vol. 94, no. 15, page 156403, 2005. (Cited on pages 70, 82, 88, 92 and 104.)

[Almog *et al.* 2006] R. Almog, S. Zaitsev, O. Shtempluck and E. Buks. *High intermodulation gain in a micromechanical Duffing resonator*. Applied Physics Letters, vol. 88, no. 21, page 213509, May 2006. (Cited on page 56.)

[Almog *et al.* 2007] R. Almog, S. Zaitsev, O. Shtempluck and E. Buks. *Signal amplification in a nanomechanical Duffing resonator via stochastic resonance*. Applied Physics Letters, vol. 90, no. 1, page 013508, January 2007. (Cited on page 56.)

[Almog 2007] R. Almog. *Nonlinear Dynamics in Nanomechanical Oscillators*. PhD thesis, Technion - Israel Institute of Technology, Faculty of Electrical Engineering, 2007. (Cited on page 56.)

[Anderson *et al.* 1972] P. w. Anderson, B. I. Halperin and c. M. Varma. *Anomalous low-temperature thermal properties of glasses and spin glasses*. Philosophical Magazine, vol. 25, no. 1, pages 1–9, January 1972. (Cited on page 116.)

[Arp *et al.* 1989] V. D. Arp, Robert D. McCarty and Daniel G. Friend. Thermophysical properties of helium-4 from 0.8 to 1500 k with pressures to 2000 mpa. National Institute of Standards and Technology (U.S.), 1989. (Cited on page 123.)

[Atta 1965] C.M. Van Atta. Vacuum science & engineering. 1965. (Cited on page 123.)

[Bachtold *et al.* 1999] A. Bachtold, C. Strunk, J.-P. Salvetat, J.-M. Bonard, L. Forró, T. Nussbaumer and C. Schönenberger. *Aharonov–Bohm oscillations in carbon nanotubes*. Nature, vol. 397, no. 6721, pages 673–675, 1999. (Cited on page 2.)

[Barois *et al.* 2013] T. Barois, A. Ayari, P. Vincent, S. Perisanu, P. Poncharal and S. T. Purcell. *Ultra Low Power Consumption for Self-Oscillating Nanoelectromechanical Systems Constructed by Contacting Two Nanowires*. Nano Letters, vol. 13, no. 4, pages 1451–1456, 2013. (Cited on page 2.)

[Bird 1994] G. A. Bird. *Molecular Gas Dynamics and the Direct Simulation of Gas Flows (Oxford Engineering Science Series)*, 1994. (Cited on pages 123 and 130.)

[Blanchard & Summers 1986] O. J. Blanchard and L. H. Summers. *Hysteresis and the European Unemployment Problem.* NBER Macroeconomics Annual, vol. 1, page 15, 1986. (Cited on page 67.)

[Bullard *et al.* 2014] Elizabeth C. Bullard, Jianchang Li, Charles R. Lilley, Paul Mulvaney, Michael L. Roukes and John E. Sader. *Dynamic Similarity of Oscillatory Flows Induced by Nanomechanical Resonators.* Physical Review Letters, vol. 112, no. 1, page 015501, January 2014. (Cited on pages 123 and 129.)

[Burg *et al.* 2007] Thomas P. Burg, Michel Godin, Scott M. Knudsen, Wenjiang Shen, Greg Carlson, John S. Foster, Ken Babcock and Scott R. Manalis. *Weighing of biomolecules, single cells and single nanoparticles in fluid.* Nature, vol. 446, no. 7139, pages 1066–1069, April 2007. (Cited on page 123.)

[Carless *et al.* 1983] D. C. Carless, H. E. Hall and J. R. Hook. *Vibrating wire measurements in liquid3He. I. The normal state.* Journal of Low Temperature Physics, vol. 50, no. 5-6, pages 583–603, March 1983. (Cited on page 127.)

[Carr *et al.* 1999] D. W. Carr, S. Evoy, L. Sekaric, H. G. Craighead and J. M. Parpia. *Measurement of mechanical resonance and losses in nanometer scale silicon wires.* Applied Physics Letters, vol. 75, no. 7, pages 920–922, August 1999. (Cited on page 36.)

[Chan & Stambaugh 2007] H. B. Chan and C. Stambaugh. *Activation Barrier Scaling and Crossover for Noise-Induced Switching in Micromechanical Parametric Oscillators.* Physical Review Letters, vol. 99, no. 6, page 060601, 2007. (Cited on pages 72 and 104.)

[Chan *et al.* 2001] H. B. Chan, V. A. Aksyuk, R. N. Kleiman, D. J. Bishop and Federico Capasso. *Quantum Mechanical Actuation of Microelectromechanical Systems by the Casimir Force.* Science, vol. 291, no. 5510, pages 1941–1944, March 2001. (Cited on page 2.)

[Chan *et al.* 2011] J. Chan, T. P. M. Alegre, A. H. Safavi-Naeini, J. T. Hill, A. Krause, S. Gröblacher, M. Aspelmeyer and O. Painter. *Laser cooling of a nanomechanical oscillator into its quantum ground state.* Nature, vol. 478, no. 7367, pages 89–92, October 2011. (Cited on page 52.)

[Chernyak *et al.* 1973] V. G. Chernyak, B. T. Porodnov and P. E. Suetin. *Thermomolecular pressure difference under arbitrary accommodation at a surface.* Journal of engineering physics, vol. 24, no. 2, pages 157–161, February 1973. (Cited on page 124.)

[Chiaverini *et al.* 2003] J. Chiaverini, S. J. Smullin, A. A. Geraci, D. M. Weld and A. Kapitulnik. *New Experimental Constraints on Non-Newtonian Forces below 100 µm.* Physical Review Letters, vol. 90, no. 15, page 151101, 2003. (Cited on page 2.)

[Cleland & Roukes 1996] A. N. Cleland and M. L. Roukes. *Fabrication of high frequency nanometer scale mechanical resonators from bulk Si crystals.* Applied Physics Letters, vol. 69, no. 18, pages 2653–2655, October 1996. (Cited on page 2.)

[Cleland & Roukes 1999] A. N. Cleland and M. L. Roukes. *External control of dissipation in a nanometer-scale radiofrequency mechanical resonator.* Sensors and Actuators A: Physical, vol. 72, no. 3, pages 256–261, 1999. (Cited on pages 2, 14 and 26.)

[Cohen & Abeles 1968] Roger Cohen and B. Abeles. *Superconductivity in Granular Aluminum Films.* Physical Review, vol. 168, no. 2, pages 444–450, April 1968. (Cited on page 117.)

[Collin *et al.* 2008] E. Collin, L. Filleau, T. Fournier, Y. M. Bunkov and H. Godfrin. *Silicon Vibrating Wires at Low Temperatures.* Journal of Low Temperature Physics, vol. 150, no. 5-6, pages 739–790, March 2008. (Cited on page 45.)

[Collin *et al.* 2010a] E. Collin, Yu. M. Bunkov and H. Godfrin. *Addressing geometric nonlinearities with cantilever microelectromechanical systems: Beyond the Duffing model.* Physical Review B, vol. 82, no. 23, page 235416, 2010. (Cited on pages 23 and 24.)

[Collin *et al.* 2010b] E. Collin, J. Kofler, S. Lakhloufi, S. Pairis, Yu M. Bunkov and H. Godfrin. *Metallic coatings of microelectromechanical structures at low temperatures: Stress, elasticity, and nonlinear dissipation.* Journal of Applied Physics, vol. 107, no. 11, page 114905, June 2010. (Cited on pages 39 and 45.)

[Collin *et al.* 2011a] E. Collin, T. Moutonet, J.-S. Heron, O. Bourgeois, Yu. M. Bunkov and H. Godfrin. *Nonlinear parametric amplification in a triport nanoelectromechanical device.* Physical Review B, vol. 84, no. 5, page 054108, 2011. (Cited on page 45.)

[Collin *et al.* 2011b] E. Collin, T. Moutonet, J.-S. Heron, O. Bourgeois, Yu M. Bunkov and H. Godfrin. *A Tunable Hybrid Electro-magnetomotive NEMS Device for Low Temperature Physics.* Journal of Low Temperature Physics, vol. 162, no. 5-6, pages 653–660, March 2011. (Cited on pages 10 and 22.)

[Collin *et al.* 2012] E. Collin, M. Defoort, K. Lulla, T. Moutonet, J.-S. Heron, O. Bourgeois, Yu M. Bunkov and H. Godfrin. *In-situ comprehensive calibration of a tri-port nano-electro-mechanical device.* Review of Scientific Instruments, vol. 83, no. 4, page 045005, April 2012. (Cited on pages 22, 24, 27, 28, 46, 48, 138 and 140.)

[Collin *et al.* 2014] E. Collin, M. Defoort, K. J. Lulla, J. Guidi, S. Dufresnes and H. Godfrin. *Modal Decomposition in Goalpost Micro/Nano Electro-*

Mechanical Devices. Journal of Low Temperature Physics, vol. 175, no. 1-2, pages 442–448, April 2014. (Cited on pages 20, 138 and 140.)

[Cross *et al.* 2004] M. C. Cross, A. Zumdieck, Ron Lifshitz and J. L. Rogers. *Synchronization by Nonlinear Frequency Pulling.* Physical Review Letters, vol. 93, no. 22, page 224101, November 2004. (Cited on page 52.)

[Dash 1975] J. G. Dash. Films on solid surfaces. the physics and chemistry of physical adsorption. New York, Academic Press, 1975. (Cited on page 125.)

[Defoort *et al.* 2011] M. Defoort, K. Lulla, J.-S. Heron, O. Bourgeois, E. Collin and F. Pistolesi. *Audio mixing in a tri-port nano-electro-mechanical device.* Applied Physics Letters, vol. 99, no. 23, page 233107, December 2011. (Cited on pages 111, 132, 134, 138 and 140.)

[Defoort *et al.* 2013a] M. Defoort, K. J. Lulla, C. Blanc, O. Bourgeois, E. Collin and A. D. Armour. *Modal "self-coupling" as a sensitive probe for nanomechanical detection.* Applied Physics Letters, vol. 103, no. 1, page 013104, July 2013. (Cited on pages 60, 62, 64, 138 and 140.)

[Defoort *et al.* 2013b] M. Defoort, K. J. Lulla, C. Blanc, H. Ftouni, O. Bourgeois and E. Collin. *Stressed Silicon Nitride Nanomechanical Resonators at Helium Temperatures.* Journal of Low Temperature Physics, vol. 171, no. 5-6, pages 731–736, June 2013. (Cited on pages 34, 35, 42, 49, 138 and 140.)

[Defoort *et al.* 2014a] M. Defoort, K. J. Lulla, T. Crozes, O. Maillet, O. Bourgeois and E. Collin. *Slippage and Boundary Layer Probed in an Almost Ideal Gas by a Nanomechanical Oscillator, and Supplemental Material therein.* Physical Review Letters, vol. 113, no. 13, page 136101, September 2014. (Cited on pages 123, 126, 130, 132, 135, 138 and 140.)

[Defoort *et al.* 2014b] M. Defoort, V. Puller, O. Bourgeois, F. Pistolesi and E. Collin. *Scaling laws for the bifurcation-escape rate in a nanomechanical resonator.* arXiv:1409.6971 [cond-mat], September 2014. arXiv: 1409.6971. (Cited on pages 104, 107, 138 and 140.)

[Dunn *et al.* 2010] T. Dunn, J.-S. Wenzler and P. Mohanty. *Anharmonic modal coupling in a bulk micromechanical resonator.* Applied Physics Letters, vol. 97, no. 12, page 123109, September 2010. (Cited on page 53.)

[Dykman & Krivoglaz 1979] M. I. Dykman and M. A. Krivoglaz. *Theory of fluctuational transitions between stable states of a non-linear oscillator.* Journal of Experimental and Theoretical Physics, vol. 77, no. 1, page 60, July 1979. (Cited on pages 69, 71, 74 and 92.)

[Dykman & Krivoglaz 1980] M. I. Dykman and M. A. Krivoglaz. *Fluctuations in nonlinear systems near bifurcations corresponding to the appearance of new*

stable states. Physica A: Statistical Mechanics and its Applications, vol. 104, no. 3, pages 480–494, 1980. (Cited on pages 69, 74 and 77.)

[Dykman *et al.* 1998] M. I. Dykman, C. M. Maloney, V. N. Smelyanskiy and M. Silverstein. *Fluctuational phase-flip transitions in parametrically driven oscillators.* Physical Review E, vol. 57, no. 5, pages 5202–5212, 1998. (Cited on page 72.)

[Eadie *et al.* 1971] W.T Eadie, D. Drijard, F.E. James, M.G. Roos and B. Sadoulet. *Statistical Methods in Experimental Physics*, 1971. (Cited on page 98.)

[Espinosa *et al.* 2003] H. D. Espinosa, B. C. Prorok, B. Peng, K. H. Kim, N. Moldovan, O. Auciello, J. A. Carlisle, D. M. Gruen and D. C. Mancini. *Mechanical properties of ultrananocrystalline diamond thin films relevant to MEMS/NEMS devices.* Experimental Mechanics, vol. 43, no. 3, pages 256–268, September 2003. (Cited on page 2.)

[Faust *et al.* 2013] T. Faust, J. Rieger, M. J. Seitner, J. P. Kotthaus and E. M. Weig. *Coherent control of a classical nanomechanical two-level system.* Nature Physics, vol. 9, no. 8, pages 485–488, 2013. (Cited on page 3.)

[Feynman 1993] R. Feynman. *Infinitesimal machinery.* Journal of Microelectromechanical Systems, vol. 2, no. 1, pages 4–14, March 1993. (Cited on page 2.)

[Fong *et al.* 2012] K. Y. Fong, W. H. P. Pernice and H. X. Tang. *Frequency and phase noise of ultrahigh Q silicon nitride nanomechanical resonators.* Physical Review B, vol. 85, no. 16, page 161410, 2012. (Cited on pages 92 and 104.)

[Gavan *et al.* 2009] K. Babaei Gavan, E. W. J. M. van der Drift, W. J. Venstra, M. R. Zuiddam and H. S. J. van der Zant. *Effect of undercut on the resonant behaviour of silicon nitride cantilevers.* Journal of Micromechanics and Microengineering, vol. 19, no. 3, page 035003, March 2009. (Cited on page 35.)

[Goellner *et al.* 1975] G. J. Goellner, J. G. Daunt and E. Lerner. *Helium adsorption on exfoliated graphite.* Journal of Low Temperature Physics, vol. 21, no. 3-4, pages 347–358, November 1975. (Cited on page 125.)

[Hanay *et al.* 2012] M. S. Hanay, S. Kelber, A. K. Naik, D. Chi, S. Hentz, E. C. Bullard, E. Colinet, L. Duraffourg and M. L. Roukes. *Single-protein nanomechanical mass spectrometry in real time.* Nature Nanotechnology, vol. 7, no. 9, pages 602–608, September 2012. (Cited on page 2.)

[Haust *et al.* 2004] J. Haust, M. Burst, R. Haueisen and G. Weiss. *Low Temperature Acoustic Properties of Poly-Crystalline Aluminium.* Journal of Low Temperature Physics, vol. 137, no. 3-4, pages 523–533, November 2004. (Cited on page 122.)

[Hoehne *et al.* 2010] F. Hoehne, Yu. A. Pashkin, O. Astafiev, L. Faoro, L. B. Ioffe, Y. Nakamura and J. S. Tsai. *Damping in high-frequency metallic nanomechanical resonators*. Physical Review B, vol. 81, no. 18, page 184112, 2010. (Cited on pages 117 and 122.)

[Holt *et al.* 2006] Jason K. Holt, Hyung Gyu Park, Yinmin Wang, Michael Stadermann, Alexander B. Artyukhin, Costas P. Grigoropoulos, Aleksandr Noy and Olgica Bakajin. *Fast Mass Transport Through Sub-2-Nanometer Carbon Nanotubes*. Science, vol. 312, no. 5776, pages 1034–1037, May 2006. (Cited on page 123.)

[Island *et al.* 2012] J. O. Island, V. Tayari, A. C. McRae and A. R. Champagne. *Few-Hundred GHz Carbon Nanotube Nanoelectromechanical Systems (NEMS)*. Nano Letters, vol. 12, no. 9, pages 4564–4569, September 2012. (Cited on page 2.)

[Jacobs 2012] K. Jacobs. *Simulating many-body lattice systems on a single nanomechanical resonator*. arXiv:1209.2499 [quant-ph], September 2012. arXiv: 1209.2499. (Cited on page 2.)

[Jensen *et al.* 1980] H. Højgaard Jensen, H. Smith, P. Wölfle, K. Nagai and T. Maack Bisgaard. *Boundary effects in fluid flow. Application to quantum liquids*. Journal of Low Temperature Physics, vol. 41, no. 5-6, pages 473–519, December 1980. (Cited on page 127.)

[Jensen *et al.* 2007] K. Jensen, J. Weldon, H. Garcia and A. Zettl. *Nanotube Radio*. Nano Letters, vol. 7, no. 11, pages 3508–3511, November 2007. (Cited on page 111.)

[Judge *et al.* 2007] John A. Judge, Douglas M. Photiadis, Joseph F. Vignola, Brian H. Houston and Jacek Jarzynski. *Attachment loss of micromechanical and nanomechanical resonators in the limits of thick and thin support structures*. Journal of Applied Physics, vol. 101, no. 1, page 013521, January 2007. (Cited on page 36.)

[Karniadakis *et al.* 2005] G. Karniadakis, A. Beskok and N. Aluru. Microflows and nanoflows - fundamentals and simulation. 2005. (Cited on page 123.)

[Kogan 2008] O. Kogan. *Scaling crossovers in activated escape of nonequilibrium systems: a resonantly driven oscillator*. arXiv:0805.0972 [cond-mat], May 2008. arXiv: 0805.0972. (Cited on pages 79, 84, 92, 103 and 105.)

[König *et al.* 1993] R. König, P. Esquinazi and F. Pobell. *Nonlinear acoustic properties of vibrating wires at very low temperatures*. Journal of Low Temperature Physics, vol. 90, no. 1-2, pages 55–76, January 1993. (Cited on page 118.)

[Kozinsky *et al.* 2006] I. Kozinsky, H. W. Ch Postma, I. Bargatin and M. L. Roukes. *Tuning nonlinearity, dynamic range, and frequency of nanomechanical resonators.* Applied Physics Letters, vol. 88, no. 25, page 253101, June 2006. (Cited on pages 22 and 42.)

[Kozinsky *et al.* 2007] I. Kozinsky, H. W. Ch. Postma, O. Kogan, A. Husain and M. L. Roukes. *Basins of Attraction of a Nonlinear Nanomechanical Resonator.* Physical Review Letters, vol. 99, no. 20, page 207201, November 2007. (Cited on pages 72 and 73.)

[Kramers 1940] H. A. Kramers. *Brownian motion in a field of force and the diffusion model of chemical reactions.* Physica, vol. 7, no. 4, pages 284–304, 1940. (Cited on page 68.)

[Kraus *et al.* 2000] A. Kraus, A. Erbe and R. H. Blick. *Nanomechanical vibrating wire resonator for phonon spectroscopy in liquid helium.* Nanotechnology, vol. 11, no. 3, page 165, September 2000. (Cited on page 3.)

[Kurkijärvi 1972] J. Kurkijärvi. *Intrinsic Fluctuations in a Superconducting Ring Closed with a Josephson Junction.* Physical Review B, vol. 6, no. 3, pages 832–835, 1972. (Cited on page 66.)

[Landau & Lifshitz 1987] L. D. Landau and E. M. Lifshitz. Fluid mechanics, second edition: Volume 6. Butterworth-Heinemann, Oxford, 2 edition édition, January 1987. (Cited on pages 123 and 126.)

[Lifshitz & Cross 2008] R. Lifshitz and M. C. Cross. *Nonlinear Dynamics of Nanomechanical and Micromechanical Resonators.* In Heinz Georg Schuster, editeur, Reviews of Nonlinear Dynamics and Complexity, pages 1–52. Wiley-VCH Verlag GmbH & Co. KGaA, 2008. (Cited on page 40.)

[Lifshitz & Roukes 2000] R. Lifshitz and M. L. Roukes. *Thermoelastic damping in micro- and nanomechanical systems.* Physical Review B, vol. 61, no. 8, pages 5600–5609, 2000. (Cited on page 36.)

[Lilley & Sader 2007] Charles R. Lilley and John E. Sader. *Velocity gradient singularity and structure of the velocity profile in the Knudsen layer according to the Boltzmann equation.* Physical Review E, vol. 76, no. 2, page 026315, August 2007. (Cited on pages 123 and 130.)

[Lilley & Sader 2008] Charles R. Lilley and John E. Sader. *Velocity profile in the Knudsen layer according to the Boltzmann equation.* Proceedings of the Royal Society of London A: Mathematical, Physical and Engineering Sciences, vol. 464, no. 2096, pages 2015–2035, August 2008. (Cited on pages 126 and 130.)

[Lockerby *et al.* 2005] Duncan A. Lockerby, Jason M. Reese and Michael A. Gallis. *Capturing the Knudsen layer in continuum-fluid models of non-equilibrium*

gas flows. AIAA Journal, vol. 43, no. 6, pages 1391–1393, June 2005. (Cited on pages 123 and 130.)

[Lulla *et al.* 2012] K. J. Lulla, R. B. Cousins, A. Venkatesan, M. J. Patton, A. D. Armour, C. J. Mellor and J. R. Owers-Bradley. *Nonlinear modal coupling in a high-stress doubly-clamped nanomechanical resonator.* New Journal of Physics, vol. 14, no. 11, page 113040, November 2012. (Cited on page 53.)

[Lulla *et al.* 2013] K. J. Lulla, M. Defoort, C. Blanc, O. Bourgeois and E. Collin. *Evidence for the Role of Normal-State Electrons in Nanoelectromechanical Damping Mechanisms at Very Low Temperatures, and Supplemental Material therein.* Physical Review Letters, vol. 110, no. 17, page 177206, 2013. (Cited on pages 132, 134, 138 and 140.)

[Lulla 2011] Kunal Lulla. *Dissipation and nonlinear effects in nanomechanical resonators at low temperatures.* Thesis, University of Nottingham, 2011. (Cited on page 117.)

[Mahboob *et al.* 2012] I. Mahboob, K. Nishiguchi, H. Okamoto and H. Yamaguchi. *Phonon-cavity electromechanics.* Nature Physics, vol. 8, no. 5, pages 387–392, 2012. (Cited on page 52.)

[Manz *et al.* 1992] Andreas Manz, D. Jed Harrison, Elisabeth M. J. Verpoorte, James. C. Fettinger, Aran Paulus, Hans Lüdi and H. Michael Widmer. *Planar chips technology for miniaturization and integration of separation techniques into monitoring systems: Capillary electrophoresis on a chip.* Journal of Chromatography A, vol. 593, no. 1–2, pages 253–258, February 1992. (Cited on page 123.)

[Matheny *et al.* 2013] M. H. Matheny, L. G. Villanueva, R. B. Karabalin, J. E. Sader and M. L. Roukes. *Nonlinear Mode-Coupling in Nanomechanical Systems.* Nano Letters, vol. 13, no. 4, pages 1622–1626, 2013. (Cited on pages 42 and 54.)

[Matheny *et al.* 2014] M. H. Matheny, M. Grau, L. G. Villanueva, R. B. Karabalin, M. C. Cross and M. L. Roukes. *Phase Synchronization of Two Anharmonic Nanomechanical Oscillators.* Physical Review Letters, vol. 112, no. 1, page 014101, January 2014. (Cited on page 52.)

[Mohanty *et al.* 2002] P. Mohanty, D. A. Harrington, K. L. Ekinci, Y. T. Yang, M. J. Murphy and M. L. Roukes. *Intrinsic dissipation in high-frequency micromechanical resonators.* Physical Review B, vol. 66, no. 8, page 085416, 2002. (Cited on page 36.)

[Nayfeh & Mook 1995] A. H. Nayfeh and D. T. Mook. *Nonlinear Oscillations*, 1995. (Cited on pages 24 and 40.)

[Nguyen 2007] C.T.-C. Nguyen. *MEMS technology for timing and frequency control.* IEEE Transactions on Ultrasonics, Ferroelectrics, and Frequency Control, vol. 54, no. 2, pages 251–270, February 2007. (Cited on page 2.)

[Novak *et al.* 1995] M. A Novak, R Sessoli, A Caneschi and D Gatteschi. *Magnetic properties of a Mn cluster organic compound.* Journal of Magnetism and Magnetic Materials, vol. 146, no. 1–2, pages 211–213, 1995. (Cited on page 66.)

[O'Connell *et al.* 2010] A. D. O'Connell, M. Hofheinz, M. Ansmann, Radoslaw C. Bialczak, M. Lenander, Erik Lucero, M. Neeley, D. Sank, H. Wang, M. Weides, J. Wenner, John M. Martinis and A. N. Cleland. *Quantum ground state and single-phonon control of a mechanical resonator.* Nature, vol. 464, no. 7289, pages 697–703, 2010. (Cited on pages 3 and 52.)

[Ozbudak *et al.* 2004] E. M. Ozbudak, M. Thattai, H. N. Lim, B. I. Shraiman and A. van Oudenaarden. *Multistability in the lactose utilization network of Escherichia coli.* Nature, vol. 427, no. 6976, pages 737–740, 2004. (Cited on page 66.)

[Palomaki *et al.* 2013] T. A. Palomaki, J. W. Harlow, J. D. Teufel, R. W. Simmonds and K. W. Lehnert. *Coherent state transfer between itinerant microwave fields and a mechanical oscillator.* Nature, vol. 495, no. 7440, pages 210–214, March 2013. (Cited on page 52.)

[Patterson 1956] Gordon N. Patterson. Molecular flow of gases. Wiley, 1956. (Cited on pages 123, 128 and 130.)

[Phillips 1972] W. A. Phillips. *Tunneling states in amorphous solids.* Journal of Low Temperature Physics, vol. 7, no. 3-4, pages 351–360, May 1972. (Cited on page 116.)

[Photiadis & Judge 2004] D. M. Photiadis and J. A. Judge. *Attachment losses of high Q oscillators.* Applied Physics Letters, vol. 85, no. 3, pages 482–484, July 2004. (Cited on page 36.)

[Pistolesi *et al.* 2008] F. Pistolesi, Y. M. Blanter and I. Martin. *Self-consistent theory of molecular switching.* Physical Review B, vol. 78, no. 8, page 085127, 2008. (Cited on page 79.)

[Rebeiz & Muldavin 2001] G.M. Rebeiz and J. B. Muldavin. *RF MEMS switches and switch circuits.* IEEE Microwave Magazine, vol. 2, no. 4, pages 59–71, 2001. (Cited on page 2.)

[Reese *et al.* 2003] Jason M. Reese, Michael A. Gallis and Duncan A. Lockerby. *New directions in fluid dynamics: non-equilibrium aerodynamic and microsystem*

flows. Philosophical Transactions of the Royal Society of London A: Mathematical, Physical and Engineering Sciences, vol. 361, no. 1813, pages 2967–2988, December 2003. (Cited on pages 123 and 130.)

[Regal *et al.* 2008] C. A. Regal, J. D. Teufel and K. W. Lehnert. *Measuring nanomechanical motion with a microwave cavity interferometer.* Nature Physics, vol. 4, no. 7, pages 555–560, 2008. (Cited on pages 3 and 52.)

[Ryvkine *et al.* 2004] D. Ryvkine, M. I. Dykman and B. Golding. *Scaling and crossovers in activated escape near a bifurcation point.* Physical Review E, vol. 69, no. 6, page 061102, 2004. (Cited on pages 84 and 105.)

[Sader 1998] John Elie Sader. *Frequency response of cantilever beams immersed in viscous fluids with applications to the atomic force microscope.* Journal of Applied Physics, vol. 84, no. 1, pages 64–76, July 1998. (Cited on page 126.)

[Schmid *et al.* 2011] S. Schmid, K. D. Jensen, K. H. Nielsen and A. Boisen. *Damping mechanisms in high-Q micro and nanomechanical string resonators.* Physical Review B, vol. 84, no. 16, page 165307, October 2011. (Cited on page 36.)

[Seoánez *et al.* 2008] C. Seoánez, F. Guinea and A. H. Castro Neto. *Surface dissipation in nanoelectromechanical systems: Unified description with the standard tunneling model and effects of metallic electrodes.* Physical Review B, vol. 77, no. 12, page 125107, March 2008. (Cited on page 122.)

[Sinvani *et al.* 1983] M. Sinvani, M. W. Cole and D. L. Goodstein. *Sticking Probability of He4 on Solid Surfaces at Low Temperature.* Physical Review Letters, vol. 51, no. 3, pages 188–191, July 1983. (Cited on page 128.)

[Siria *et al.* 2009] A. Siria, A. Drezet, F. Marchi, F. Comin, S. Huant and J. Chevrier. *Viscous Cavity Damping of a Microlever in a Simple Fluid.* Physical Review Letters, vol. 102, no. 25, page 254503, June 2009. (Cited on page 123.)

[Siria *et al.* 2013] Alessandro Siria, Philippe Poncharal, Anne-Laure Biance, Rémy Fulcrand, Xavier Blase, Stephen T. Purcell and Lydéric Bocquet. *Giant osmotic energy conversion measured in a single transmembrane boron nitride nanotube.* Nature, vol. 494, no. 7438, pages 455–458, February 2013. (Cited on page 123.)

[Southworth *et al.* 2009] D. R. Southworth, R. A. Barton, S. S. Verbridge, B. Ilic, A. D. Fefferman, H. G. Craighead and J. M. Parpia. *Stress and Silicon Nitride: A Crack in the Universal Dissipation of Glasses.* Physical Review Letters, vol. 102, no. 22, page 225503, 2009. (Cited on pages 3 and 117.)

[Stambaugh & Chan 2006] C. Stambaugh and H. B. Chan. *Noise-activated switching in a driven nonlinear micromechanical oscillator.* Physical Review B, vol. 73, no. 17, page 172302, 2006. (Cited on pages 72, 73 and 98.)

[Stokes 1851] G. G. Stokes. *On the Composition and Resolution of Streams of Polarized Light from different Sources.* Transactions of the Cambridge Philosophical Society, vol. 9, page 399, 1851. (Cited on page 126.)

[Suhel *et al.* 2012] A. Suhel, B. D. Hauer, T. S. Biswas, K. S. D. Beach and J. P. Davis. *Dissipation mechanisms in thermomechanically driven silicon nitride nanostrings.* Applied Physics Letters, vol. 100, no. 17, page 173111, April 2012. (Cited on pages 36 and 37.)

[Terry *et al.* 1979] S.C. Terry, J.H. Jerman and J.B. Angell. *A gas chromatographic air analyzer fabricated on a silicon wafer.* IEEE Transactions on Electron Devices, vol. 26, no. 12, pages 1880–1886, December 1979. (Cited on page 123.)

[Triqueneaux *et al.* 2000] S. Triqueneaux, E. Collin, D. J Cousins, T. Fournier, C. Bäuerle, Yu. M. Bunkov and H. Godfrin. *Microfabrication of silicon vibrating wires.* Physica B: Condensed Matter, vol. 284–288, Part 2, pages 2141–2142, 2000. (Cited on page 2.)

[Turlot *et al.* 1989] E. Turlot, D. Esteve, C. Urbina, J. M. Martinis, M. H. Devoret, S. Linkwitz and H. Grabert. *Escape oscillations of a Josephson junction switching out of the zero-voltage state.* Physical Review Letters, vol. 62, no. 15, pages 1788–1791, 1989. (Cited on page 66.)

[Unterreithmeier *et al.* 2010] Q. P. Unterreithmeier, T. Faust and J. P. Kotthaus. *Damping of Nanomechanical Resonators.* Physical Review Letters, vol. 105, no. 2, page 027205, 2010. (Cited on page 36.)

[Venkatesan *et al.* 2010] A. Venkatesan, K. J. Lulla, M. J. Patton, A. D. Armour, C. J. Mellor and J. R. Owers-Bradley. *Dissipation due to tunneling two-level systems in gold nanomechanical resonators.* Physical Review B, vol. 81, no. 7, page 073410, 2010. (Cited on page 117.)

[Venstra *et al.* 2012] Warner J. Venstra, Ronald van Leeuwen and Herre S. J. van der Zant. *Strongly coupled modes in a weakly driven micromechanical resonator.* Applied Physics Letters, vol. 101, no. 24, page 243111, December 2012. (Cited on page 55.)

[Venstra *et al.* 2013] W. J. Venstra, H. J. R. Westra and H. S. J. van der Zant. *Stochastic switching of cantilever motion.* Nature Communications, vol. 4, October 2013. (Cited on page 66.)

[Verbridge *et al.* 2008] S. S. Verbridge, H. G. Craighead and J. M. Parpia. *A megahertz nanomechanical resonator with room temperature quality factor over a million.* Applied Physics Letters, vol. 92, no. 1, page 013112, January 2008. (Cited on page 36.)

[Verpoorte & de Rooij 2003] E. Verpoorte and N.F. de Rooij. *Microfluidics meets MEMS*. Proceedings of the IEEE, vol. 91, no. 6, pages 930–953, June 2003. (Cited on page 2.)

[Villanueva *et al.* 2013] L. G. Villanueva, R. B. Karabalin, M. H. Matheny, D. Chi, J. E. Sader and M. L. Roukes. *Nonlinearity in nanomechanical cantilevers*. Physical Review B, vol. 87, no. 2, page 024304, January 2013. (Cited on page 24.)

[Vincent *et al.* 2011] P. Vincent, P. Poncharal, T. Barois, S. Perisanu, V. Gouttenoire, H. Frachon, A. Lazarus, E. de Langre, E. Minoux, M. Charles, A. Ziaei, D. Guillot, M. Choueib, A. Ayari and S. Purcell. *Performance of field-emitting resonating carbon nanotubes as radio-frequency demodulators*. Physical Review B, vol. 83, no. 15, page 155446, April 2011. (Cited on page 111.)

[Weiss *et al.* 1981] G. Weiss, S. Hunklinger and H. von Löhneysen. *Influence of superconductivity on the sound propagation in disordered metals*. Physics Letters A, vol. 85, no. 2, pages 84–86, September 1981. (Cited on page 122.)

[Westra *et al.* 2010] H. J. R. Westra, M. Poot, H. S. J. van der Zant and W. J. Venstra. *Nonlinear Modal Interactions in Clamped-Clamped Mechanical Resonators*. Physical Review Letters, vol. 105, no. 11, page 117205, September 2010. (Cited on pages 52 and 53.)

[Witkamp *et al.* 2006] Benoit Witkamp, Menno Poot and Herre S. J. van der Zant. *Bending-Mode Vibration of a Suspended Nanotube Resonator*. Nano Letters, vol. 6, no. 12, pages 2904–2908, December 2006. (Cited on page 111.)

[Yamamoto & Sera 1985] Kyoji Yamamoto and Kazuyuki Sera. *Flow of a rarefied gas past a circular cylinder*. Physics of Fluids (1958-1988), vol. 28, no. 5, pages 1286–1293, May 1985. (Cited on pages 129 and 131.)

[Zolfagharkhani *et al.* 2005] Guiti Zolfagharkhani, Alexei Gaidarzhy, Seung-Bo Shim, Robert L. Badzey and Pritiraj Mohanty. *Quantum friction in nanomechanical oscillators at millikelvin temperatures*. Physical Review B, vol. 72, no. 22, page 224101, 2005. (Cited on page 117.)

Abstract

The investigation of non-linear dynamics intrinsically opens access to a broad field of researches, and Nano-Electro-Mechanical Systems (NEMS) are valuable tools for this purpose. In the present manuscript, we emphasize the fundamental applications of non-linear nano-resonators for condensed matter. After a careful calibration of our peculiar experimental set-up, we characterise the relevant parameters associated to the resonance of our devices, notably the Duffing non-linearity which is the essence of coupling mechanisms between distinct modes of the system. We present a new scheme emerging from the mode-coupling technique, using a two-tone drive but actuating a single flexural mode: a high detection precision procedure. The Duffing regime also opens an hysteresis within the resonance line of the NEMS, and the device is then employed as a model system for the associated bifurcation process. We explored numerically and experimentally this physical phenomenon and found that both the non-linear behaviour and the universal power laws described in the general theory are still valid far beyond any analytical predictions. We finally describe different techniques using NEMS as sensors to measure fundamental features of condensed matter physics, like signatures of two level systems within the resonator's material or slippage in a rarefied gas.

Résumé

L'étude des systèmes non-linéaires ouvre un large champ d'investigation en recherche fondamentale, dans cette optique les Systèmes Nano-Electro-Mécanique (NEMS) sont des outils de premier choix. Ce manuscrit met en avant l'utilisation des propriétés non-linéaires de nano-résonateurs pour la physique fondamentale. À la suite d'une calibration rigoureuse de notre dispositif expérimental, nous avons caractérisé les principaux paramètres associés à la résonance de nos structures avec, en particulier, la non-linéarité de Duffing qui est à la source des mécanismes de couplage entre les différents modes de notre système. Un nouveaux procédé expérimental utilisant une excitation à deux tons est présenté, émergeant du couplage entre modes mais en stimulant un seul mode résonant : un système de détection à haute précision. Le régime de Duffing engendre également l'ouverture d'une hystérésis au sein de la courbe de résonance du NEMS, configuration qui est alors utilisée comme système modèle pour le phénomène de bifurcation. Nous démontrons, numériquement et expérimentalement, que le comportement non-linéaire et les lois de puissances universelles décrites par la théorie sont valides au-delà des prédictions attendues. Différentes techniques expérimentales sont finalement présentées, utilisant les NEMS afin de détecter des caractéristiques fondamentales de la matière condensée, comme les signatures des systèmes à deux niveaux présents au sein des nano-résonateurs ou les propriétés de glissement dans un gaz raréfié.